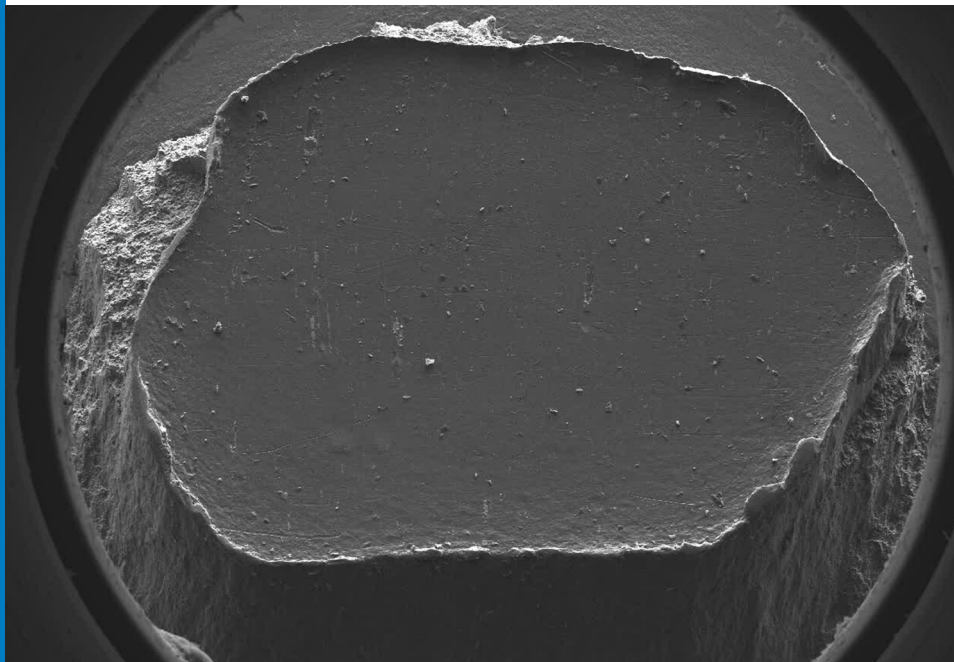
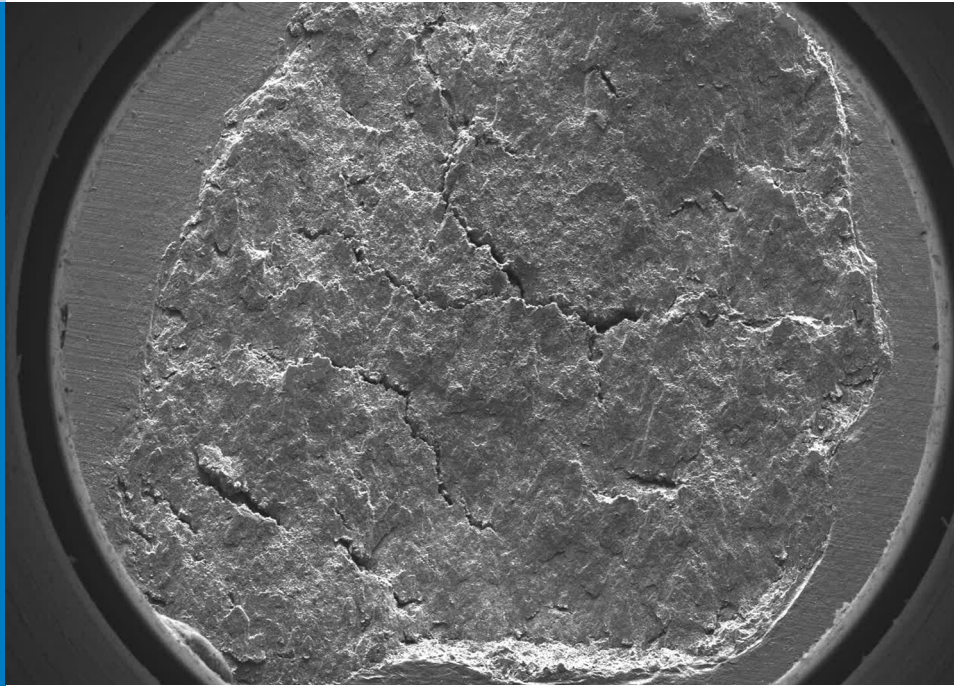




Strojniški vestnik

Journal of Mechanical Engineering



no. **11**
year **2016**
volume **62**

Strojniški vestnik – Journal of Mechanical Engineering (SV-JME)

Aim and Scope

The international journal publishes original and (mini)review articles covering the concepts of materials science, mechanics, kinematics, thermodynamics, energy and environment, mechatronics and robotics, fluid mechanics, tribology, cybernetics, industrial engineering and structural analysis.

The journal follows new trends and progress proven practice in the mechanical engineering and also in the closely related sciences as are electrical, civil and process engineering, medicine, microbiology, ecology, agriculture, transport systems, aviation, and others, thus creating a unique forum for interdisciplinary or multidisciplinary dialogue.

The international conferences selected papers are welcome for publishing as a special issue of SV-JME with invited co-editor(s).

Editor in Chief

Vincenc Butala

University of Ljubljana, Faculty of Mechanical Engineering, Slovenia

Technical Editor

Pika Škraba

University of Ljubljana, Faculty of Mechanical Engineering, Slovenia

Founding Editor

Bojan Kraut

University of Ljubljana, Faculty of Mechanical Engineering, Slovenia

Editorial Office

University of Ljubljana, Faculty of Mechanical Engineering

SV-JME, Aškerčeva 6, SI-1000 Ljubljana, Slovenia

Phone: 386 (0)1 4771 137

Fax: 386 (0)1 2518 567

info@sv-jme.eu, <http://www.sv-jme.eu>

Print: Grafex, d.o.o., printed in 310 copies

Founders and Publishers

University of Ljubljana, Faculty of Mechanical Engineering, Slovenia

University of Maribor, Faculty of Mechanical Engineering, Slovenia

Association of Mechanical Engineers of Slovenia

Chamber of Commerce and Industry of Slovenia,

Metal Processing Industry Association

President of Publishing Council

Branko Širok

University of Ljubljana, Faculty of Mechanical Engineering, Slovenia

Vice-President of Publishing Council

Jože Balič

University of Maribor, Faculty of Mechanical Engineering, Slovenia

International Editorial Board

Kamil Arslan, Karabuk University, Turkey

Hafiz Muhammad Ali, University of Engineering and Technology, Pakistan

Josep M. Bergada, Politechnical University of Catalonia, Spain

Anton Bergant, Litostroj Power, Slovenia

Miha Boltežar, UL, Faculty of Mechanical Engineering, Slovenia

Franci Čuš, UM, Faculty of Mechanical Engineering, Slovenia

Anselmo Eduardo Diniz, State University of Campinas, Brazil

Igor Emri, UL, Faculty of Mechanical Engineering, Slovenia

Imre Felde, Obuda University, Faculty of Informatics, Hungary

Janez Grum, UL, Faculty of Mechanical Engineering, Slovenia

Imre Horvath, Delft University of Technology, The Netherlands

Aleš Hribernik, UM, Faculty of Mechanical Engineering, Slovenia

Soichi Ibaraki, Kyoto University, Department of Micro Eng., Japan

Julius Kaplunov, Brunel University, West London, UK

Iyas Khader, Fraunhofer Institute for Mechanics of Materials, Germany

Jernej Klemenc, UL, Faculty of Mechanical Engineering, Slovenia

Milan Kljajin, J.J. Strossmayer University of Osijek, Croatia

Peter Krajnik, Chalmers University of Technology, Sweden

Janez Kušar, UL, Faculty of Mechanical Engineering, Slovenia

Gorazd Lojen, UM, Faculty of Mechanical Engineering, Slovenia

Thomas Lübben, University of Bremen, Germany

Janez Možina, UL, Faculty of Mechanical Engineering, Slovenia

George K. Nikas, KADMOS Engineering, UK

José L. Ocaña, Technical University of Madrid, Spain

Miroslav Plančak, University of Novi Sad, Serbia

Vladimir Popović, University of Belgrade, Faculty of Mech. Eng., Serbia

Franci Pušavec, UL, Faculty of Mechanical Engineering, Slovenia

Bernd Sauer, University of Kaiserslautern, Germany

Rudolph J. Scavuzzo, University of Akron, USA

Arkady Voloshin, Lehigh University, Bethlehem, USA

General information

Strojniški vestnik – Journal of Mechanical Engineering is published in 11 issues per year (July and August is a double issue).

Institutional prices include print & online access: institutional subscription price and foreign subscription €100,00 (the price of a single issue is €10,00); general public subscription and student subscription €50,00 (the price of a single issue is €5,00). Prices are exclusive of tax. Delivery is included in the price. The recipient is responsible for paying any import duties or taxes. Legal title passes to the customer on dispatch by our distributor.

Single issues from current and recent volumes are available at the current single-issue price. To order the journal, please complete the form on our website. For submissions, subscriptions and all other information please visit: <http://en.sv-jme.eu/>.

You can advertise on the inner and outer side of the back cover of the journal. The authors of the published papers are invited to send photos or pictures with short explanation for cover content.

We would like to thank the reviewers who have taken part in the peer-review process.

The journal is subsidized by Slovenian Research Agency.

Strojniški vestnik - Journal of Mechanical Engineering is available on <http://www.sv-jme.eu>, where you access also to papers' supplements, such as simulations, etc.



Cover:
SEM image of failure types on spot welding samples after tensile-shear test for different welding distance of adjacent spots to investigate shunting effect on AA2219 sheet

Image Courtesy:
Mehdi Jafari Vardaniani, Iran

ISSN 0039-2480

© 2016 Strojniški vestnik - Journal of Mechanical Engineering. All rights reserved. SV-JME is indexed / abstracted in: SCI-Expanded, Compendex, Inspec, ProQuest-CSA, SCOPUS, TEMA. The list of the remaining bases, in which SV-JME is indexed, is available on the website.

Contents

Strojniški vestnik - Journal of Mechanical Engineering
volume 62, (2016), number 11
Ljubljana, November 2016
ISSN 0039-2480

Published monthly

Papers

Mehdi Jafari Vardanjani, Alireza Araee, Jacek Senkara, Majid Sohrabian, Roozbeh Zarandooz: Influence of Shunting Current on the Metallurgical and Mechanical Behaviour of Resistance Spot-welded Joints in AA2219 Joints	625
Tahsin Tecelli Öpöz, Xun Chen: Chip Formation Mechanism Using Finite Element Simulation	636
Liqiang Zhang, Kai Zhang, Yecui Yan: Local Corner Smoothing Transition Algorithm Based on Double Cubic NURBS for Five-axis Linear Tool Path	647
Piotr Zgórnjak, Wojciech Stachurski, Dariusz Ostrowski: Application of Thermographic Measurements for the Determination of the Impact of Selected Cutting Parameters on the Temperature in the Workpiece During Milling Process	657
Yongsheng Zhao, Cheng Yang, Ligang Cai, Weimin Shi, Yi Hong: Stiffness and Damping Model of Bolted Joints with Uneven Surface Contact Pressure Distribution	665
Xiangyang Xu, Youchuan Tao, Changrong Liao, Shaojiang Dong, Renxiang Chen: Dynamic Simulation of Wind Turbine Planetary Gear Systems with Gearbox Body Flexibility	678
Liljana Ferbar Tratar: Comprehensive Energy Resource Management for Essential Reduction of the Total Cost	685

Influence of Shunting Current on the Metallurgical and Mechanical Behaviour of Resistance Spot-welded Joints in AA2219 Joints

Mehdi Jafari Vardanjani^{1,*} – Alireza Araee¹ – Jacek Senkara² – Majid Sohrabian³ – Roozbeh Zarandooz⁴

¹ University of Tehran, Department of Mechanical Engineering, Iran

² Warsaw University of Technology, Department of Welding Engineering, Poland

³ University of Science & Technology, Department of Mechanical Engineering, Iran

⁴ Arak University of Technology, Department of Mechanical Engineering, Iran

The effects of shunting current on metallurgical and mechanical behavior of resistance spot-welded (RSW) joints in AA2219 sheets are analysed experimentally via the investigation of mechanical and metallurgical properties, while numerical results predicted by the finite element method (FEM) are used to check the thermal aspects of the phenomenon and its effect on experimental results. Welding distance is chosen as the main variable for two consecutive nuggets. Predicted temperature distribution and cooling rates of FEM are verified by checking the nuggets and heat-affected zone (HAZ) dimensions, the SEM investigation of cracks, and performing a tensile-shear test. Experimental results have been in agreement with the predicted results, since HAZ development, the presence of cracks, interfacial failure, and poor mechanical strength of shunted nugget with shorter welding distance are all predicted in the form of temperature distribution and cooling rates of shunted nugget in finite element analysis (FEA). The temperature dependence of material properties and coupling between all aspects of the solution are respected in the FEA model while experimental tests are performed according to a three-factor design of experiment (DOE) to set the levels of factors based on their significance.

Keywords: shunting effect; heat affected zone; tensile-shear strength; failure type; finite element method

Highlights

- Shunting effect of RSW is considered for the brittleness of joints, and FEM results are used to check thermal effects of the phenomenon on metallurgical and mechanical behaviour.
- Distance effect of the shunting current was clearly observable on tensile-shear strength.
- Experimental and numerical results proved a shunting effect on crack generation.
- HAZ asymmetry due to shunting effect was observed experimentally and numerically.
- Influence of welding distance was discovered for the failure type in tensile-shear strength.

0 INTRODUCTION

Shunting current appears in resistance spot-welds (RSW) when there is a secondary circuit next to main welding current. This circuit is usually provided by previous spot(s), therefore a fraction of the applied welding current passes via previous welding spot(s). This phenomenon alternates metallurgical and mechanical qualities of the current spot due to changes in electrical and temperature distributions. Parameters affecting this phenomenon include welding distance, number, and size of previous nuggets, surface roughness, and electrode force. This phenomenon occurs in many industries requiring intermittent joints made by RSW. One of the significant industries including this type of joints is aerospace industry in which AA2219 is a common alloy used to produce many parts of products, such as fuselages and so on. The reliable mechanical and metallurgical quality of these joints are necessary for the final performance of products. Therefore, assuring the final quality

of intermittent RSW joints is inevitable in such industries. This proves the necessity of experimental and analytical consideration of the shunting effect on welding nuggets to optimize parameters and avoid undesirable consequences, particularly regarding the mechanical and metallurgical quality of the final product. In addition, regardless of the shunting effect, the comparison of failure load values obtained using the RSW process and other joining methods such as riveting of steel sheets by Zeyveli et al. [1] in which the maximum strength of 2.747 kN was obtained (which is less than the values usually obtained for RSW of aluminum alloys), demonstrates the importance of considering RSW and its associated issues to solve, rather other similar joining processes.

One of the oldest experimental studies of the shunting effect was performed by Hard [2] who provided a method for detecting shunting paths. Sheet size, weld spacing, electrode geometry, and electrode force were considered in the following studies to find minimum required distance of shunting effect [3].

*Corr. Author's Address: University of Tehran, North Kargar St., Tehran, Iran, mehdi.jafari@ut.ac.ir

The effect of shunting current on crack generation in RSW of AA5754 (Senkara and Zhang [4] and Zhang et al. [5]) was observed as the side effects of multiple spot welding, while the necessity and requirement of deeper investigation on the influence of shunting current on mechanical aspects of shunted spots was proved as a result. The effect of surface quality was checked by Howe [6] and Wang et al. [7] to observe the effect of surface conditions on shunting intensity.

Modeling and theoretical approaches to consider shunting effects have been numerable due to difficulty in the asymmetric configuration of the shunted nugget model, and assigning appropriate properties to the previous (shunting) spot, if two adjacent nuggets were to be analyzed; however, the electrical, thermal, and mechanical principles are similar, regardless of the configuration of the problem.

Among the most important numerical studies are a 3D finite element analysis (FEA) by Chang and Cho [3], in which electrical and thermal parameters were predicted in a shunted nugget or a theoretical model developed by Li et al. [8], to obtain the minimum required welding distance. The latter case was designed based on many geometrical simplifying assumptions. Simulation of temperature and electrical potential distribution (Tsai et al. [9]), prediction of contact radius (Shen et al. [10]), nugget formation and deformations (Nied [11]), and coupled analysis of RSW process (Zhang [12] and Kim et al. [13]) are examples of general FEA on asymmetric configuration of a single spot.

In this paper, the influence of shunting current on metallurgical and mechanical behaviour of resistance spot welded joints in AA2219 joints is analyzed experimentally by investigation of mechanical and metallurgical behaviour while numerical results predicted by the finite element method (FEM) are used to check thermal aspects of the phenomenon and its effects on experimental results. Welding distance is chosen as the main variable for two consecutive

nuggets. Predicted temperature distribution and cooling rates of FEM indicate the heat-affected zone (HAZ) distribution toward previous spot and brittle structure with poor tensile-shear strength respectively, for shorter welding distances. Both of these predictions are verified by checking the nugget and HAZ dimensions, tensile-shear test, and SEM consideration of samples, revealing the presence of cracks, poorer mechanical strength, and interfacial failure of shunted nuggets with shortened welding distances.

1 METHODS

FEA and experiments performed are described here separately.

1.1 Finite Element Analysis

Mathematical equations, the configuration of the model, and the material properties used in FEM are described in this section.

1.1.1 Mathematical Equations

Electrical and thermal equations plus boundary conditions are explained in a distinguished manner here.

1.1.1.1 Electrical Equations

Quasi-Laplace equation of electrical potential ϕ , can be written in 3D coordinates as [2]:

$$\frac{\partial}{\partial x} \left[\frac{1}{\rho} \cdot \frac{\partial \phi}{\partial x} \right] + \frac{\partial}{\partial y} \left[\frac{1}{\rho} \cdot \frac{\partial \phi}{\partial y} \right] + \frac{\partial}{\partial z} \left[\frac{1}{\rho} \cdot \frac{\partial \phi}{\partial z} \right] = 0, \quad (1)$$

where ρ is the bulk electrical resistivity. Boundary conditions are provided in Table A1 according to Fig.

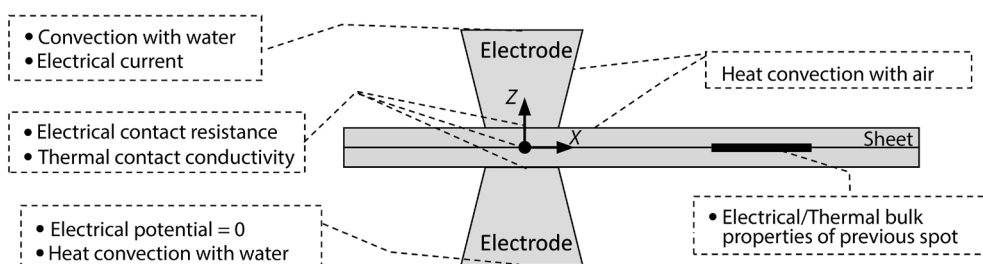


Fig. 1. Schematics for boundary conditions and important domains

1. For the application of the alternative current, it can be assumed that [14]:

$$I_e = \frac{I_p}{\sqrt{2}}, \quad (2)$$

where I_e is the applied electrical current on electrode and I_p is the maximum electrical current supplied in the welding machine. Eq. (3) is used to calculate electrical contact resistivity [14].

$$\rho_c(T) = R_C(20^\circ\text{C}) \cdot \frac{A_C}{L_C} \sqrt{\frac{\sigma_{e,ave}(T)}{\sigma_{e,ave}(20^\circ\text{C})}}, \quad (3)$$

where $R_C(20^\circ\text{C})$ is the measured electrical contact resistance (ECR) of the electrode-sheet interface at 20°C under constant mechanical pressure, L_C is the characteristic thickness of contact surfaces (assumed equal to 1×10^{-4} for some aluminium alloys as reported by Sun and Dong [15]), A_C is the nominal contact area, $\sigma_{e,ave}(T)$ and $\sigma_{e,ave}(20^\circ\text{C})$ are the average yield stress of contacting materials at T and 20°C respectively.

1.1.1.2 Thermal Equations

The thermal equation is presented in Eq. (4) [2] and [16].

$$D \cdot c \cdot \frac{\partial T}{\partial t} = \frac{\partial}{\partial x} \left[k \cdot \frac{\partial T}{\partial x} \right] + \frac{\partial}{\partial y} \left[k \cdot \frac{\partial T}{\partial y} \right] + \frac{\partial}{\partial z} \left[k \cdot \frac{\partial T}{\partial z} \right] + \frac{1}{\rho} \nabla \phi \cdot \nabla \phi, \quad (4)$$

where D is mass density, c is specific heat capacity, k is thermal conductivity coefficient, and T is temperature. Specific heat capacity after melting temperature (phase change) (c_w) follows Eq. (5) [3].

$$c_w = \frac{H_m}{T_l - T_s}, \quad (5)$$

where H_m is fusion latent heat, and T_s and T_l are solidus and liquidus temperatures, respectively. Thermal boundary conditions are provided in Table A2.

Thermal contact conductivity (TCC) coefficients are calculated using Eq. (6) as reported by Zhang and Senkara [17].

$$k_c = \frac{1}{3} \left(\frac{\sigma}{\sigma_e} \right) \left(\frac{k_1 + k_2}{2} \right), \quad (6)$$

where k_c is the TCC coefficient, σ is normal stress, σ_e is yield stress, and k_1 and k_2 are the TCC coefficient of contacting parts.

1.1.2 Configuration of the Model

To simplify the calculation process, the previous nugget is defined as a cylindrical connection between the two sheets (Fig. 2) and the diameter is specified according to the dimensions of an experimental nugget, obtained using average welding parameters in single spot welding.

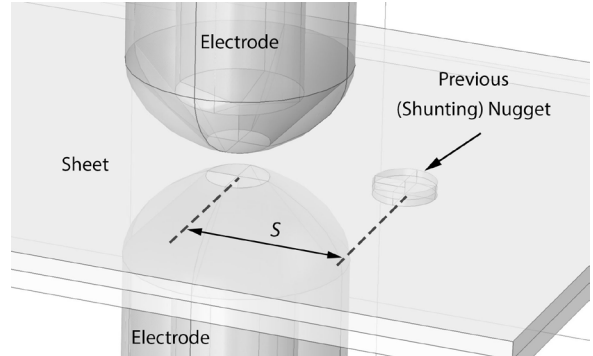


Fig. 2. Welding configuration, showing shunting (previous) nugget and other parts in FEM model

1.1.3 Material Properties

The elastic-plastic material is specified as the type of material for AA2219 in the model. The composition of the alloy is identified by a scanning electron microscope (SEM) at different points on the sample, as shown in Table B1. Tables B2 and B3 provide important properties of AA2219. Table B4 provides important properties of C18150 as the material used for electrodes. Table B5 indicates important electrical and mechanical properties of the shunting nugget. Since the temperature of the nugget does not change drastically during the process, ambient temperature properties are assigned. Therefore, the thermal properties of the shunting nugget are also defined as the same as the sheet alloy. Table B6 shows electrical contact resistance (ECR) values measured at room temperature. Electrical resistances are measured experimentally using the method reported by Vogler and Sheppard [18] while mechanical properties were determined by performing micro-hardness and extraction of elasticity modulus and yield strength, reported by nano-indentor. All of these material properties are used in the FEA process as temperature dependent or independent properties according to the parameter's formula.

The melting process is modelled using phase change capability in multi-physics simulation software (COMSOL). Both solid and liquid phases were defined

in the software to achieve a reliable simulation, while material properties changed according to temperature and phase state (Table B2). Therefore, the behaviour of the molten alloy was different from the solid state as some of the properties changed after the phase change. For instance, the strength of material reaches the minimum value according to material properties in high temperature (liquid state), or specific heat capacity changes according to Eq. (5); however, the liquid properties, such as viscosity or fluidity, were ignored since the liquid state appears for a very short time and does not considerably influence the progress of the simulation. Therefore, it is reasonable to ignore such properties as other studies such as [15] and [19] included similar assumptions for finite element analysis of the melting process.

1.2 Experiments

Weldability tests, the design of experiment (DOE), metallographic considerations, and tensile-shear tests are the main phases of the experiments. Principles of coupon preparation, inspection of results, as well as the preheating and welding parameters, were excerpted from military and welding handbooks [20] and [21]. 12 kA and 4 cycles was chosen for preheating, while the off time was 2 cycles. The squeeze and holding forces were 2 kN and 3.2 kN respectively. The initial range of welding current, time, and force for DOE were 22 kA to 26 kA, 2 cycles to 10 cycles, and 2.5 kN to 3.2 kN respectively. Electrode was chosen as dome type according to previous studies [21] (Fig. 3).

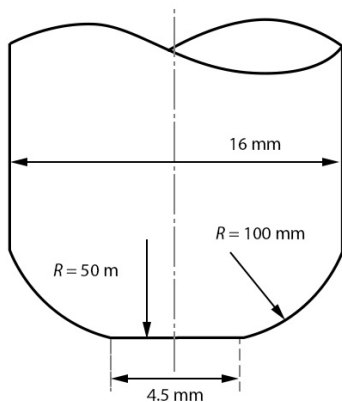


Fig. 3. Geometry of electrodes

1.2.1 Weldability Tests

The weldability window was obtained (Fig. 4) after finding the allowable electrode force to provide an

expulsion-free nugget diameter between $3.5\sqrt{t_s}$ and $3.5\sqrt{t_s}$ [20] and [23] where t_s is sheet thickness [21].

1.2.2 Design of Experiments (DOE)

Three-factor DOE was performed in a rectangular area inside the welding lobe for both nugget diameter and failure load, while the welding distance range was set according to a previous study by Howe [6] (Table 1). Figs. 5 and 6 show schematic and real samples after welding, respectively. Spot S_1 (shunting spot) on all samples was welded using the average parameters provided in Table 2. The electrode force was set to 2900 kN for all tests according to previous study [24]. After welding the procedure, the specimens were cut through the spots for geometrical and metallurgical considerations.

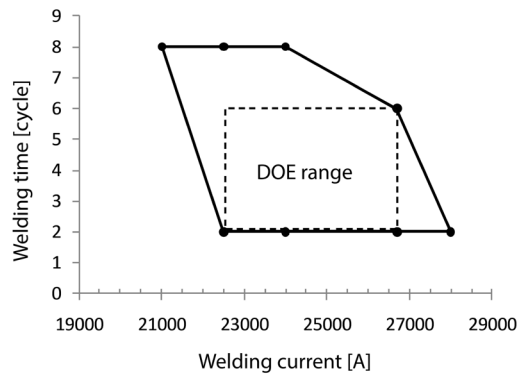


Fig. 4. Weldability region obtained via numerical and experimental results

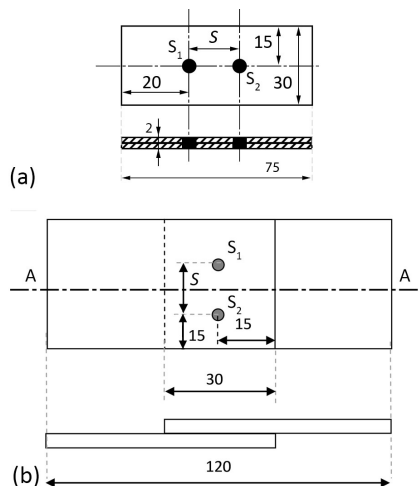


Fig. 5. Arrangement of spots for DOE; a) samples for nugget dimension checking, b) Samples for tensile-shear test; samples are cut along A-A line to check spot strength; S is distance (dimensions in mm)

1.2.3 Tensile-Shear Tests

Tensile-shear tests were performed inside the weldability range, after designing experiments for welding current, time, and distance. The specimens shown in Fig. 5 were first cut along the A-A line then they were implemented in the tensile testing machine to check the failure strength of the shunted nugget which was then converted to failure load using the nugget area.

Table 1. Chosen range of welding current and time for DOE

Parameter	Min	Max
Welding Current [kA]	22.5	26.7
Welding time [cycle]	2	6
Weld spacing [mm]	5	20

Table 2. Average welding parameters for spot

Current [kA]	Welding time [cycle]	Force [kN]
24	4	2.9

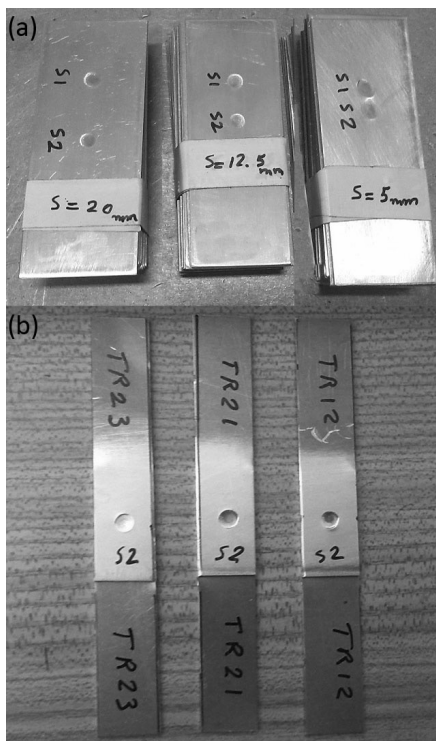


Fig. 6. Welded specimens for a) dimension checking, b) tensile-shear test (after cutting along A-A line)

1.2.4 Equipment

The welding procedure was performed using an RSW machine PFP 231 connected to a special device (TE1600) for checking electrical parameters, while

tensile-shear tests were done using a Zwick-Roell Z250 machine. Cut specimens were then mounted for geometrical and metallurgical considerations under a light microscope (Olympus SZX9) while other samples were investigated with SEM (JEOL JSM-7600F).

2 RESULTS AND DISCUSSION

Results are provided according to the following order:

- Considering predicted temperature distribution on the shunted nuggets and comparing them with micrographs,
- Considering predicted cooling rates on shunted nuggets and comparing them with mechanical quality in terms of presence of cracks, tensile-shear strength, and failure types, using SEM images and tensile-shear test results.

2.1 HAZ Development

HAZ growth around the shunted nugget and between spots is considered numerically by checking temperature distribution, while it is discovered experimentally by investigation of shunted nugget micrographs.

2.1.1 Predicted Temperature Distribution

The temperature distribution for HAZ development between spots along *x*-axis on the faying surface is indicated in Fig. 7 during the cooling phase, about 1 cycle after the welding current is switched off. The asymmetry of temperature distribution is observed for both distances while it is severe for a shorter distance. Higher levels of temperatures appeared between the spots. This is an important cause of HAZ generation between spots with a bigger volume for 5 mm welding distance. Although asymmetry of temperature distribution is also observed for 20 mm welding distance, the level of temperatures does not cause the generation of HAZ, in comparison to the values calculated for the 5 mm welding distance between weld spots.

2.1.2 HAZ Growth in Micrographs

As shown in Fig. 8, the development of HAZ toward the previous nugget is indicated for nugget with a shorter welding distance (Fig. 8a). Shunted nugget size is also reduced due to shunting effect while the

volume of HAZ is increased in the vertical direction versus nugget size compared to longer welding distance (Fig. 8b). This is a reasonable proof for the predicted temperature distribution obtained in Fig. 7 as temperature values between and over the spot during a cooling phase are adequate to generate HAZ in these domains.

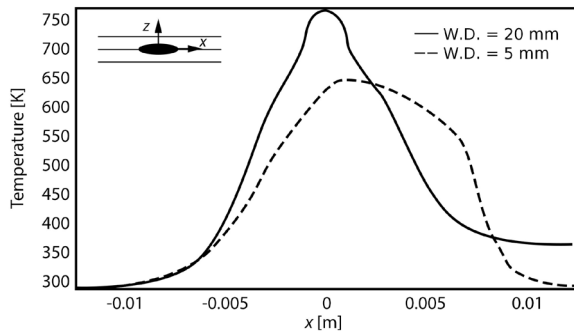


Fig. 7. Predicted temperature distribution during cooling phase for a) 5 mm, and b) 20 mm weld spacing along x-axis on faying surface, with 25.3 kA and 4 cycles welding current and time respectively; W.D. means welding distance

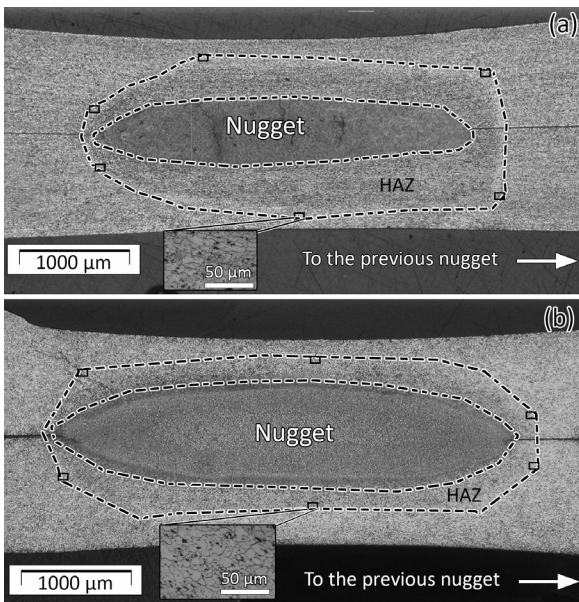


Fig. 8. Section of welding nugget for a) 5 mm, b) 20 mm weld spacing, for 25.3 kA and 4 cycles welding current and time respectively; Rectangles indicate important places at which HAZ boundary is checked

The HAZ domain shown in Fig. 8 was measured using light microscope images around nugget with 500 \times magnification. Six important points at which the transition of HAZ to the base metal occurs are indicated in Fig. 8, while one of them is magnified.

2.2 Brittleness and Strength Reduction

Influence of welding distance on brittleness and reduction in tensile-shear strength of the shunted nugget is predicted by checking cooling rates of the nugget and the HAZ around it. This phenomenon is comprehensively considered by three different experimental investigations. Cracks are observed on SEM images, tensile-shear test results are investigated, and the failure types of nuggets are compared.

2.2.1 Predicted Cooling Rates

Cooling rates for shunted nuggets are calculated numerically at the centre of the nugget, for both welding distances (Fig. 9). The higher cooling rate is obtained for 20 mm welding distance, according to the FEM results for the centre point. The reason for indicating solidus temperature in Fig. 9 is the importance of this temperature which will be discussed more in the next section.

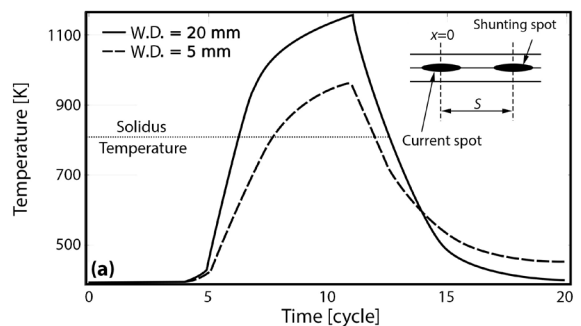


Fig. 9. Predicted cooling and heating rates for $x=0$ of current welding spot, for with 25.3 kA and 4 cycles welding current and time respectively

Although the purpose of this study is to verify the prediction of temperature variation on the metallurgical and mechanical behaviour of AA2219 shunted RSW joints, the validity of temperature prediction has also been indirectly checked by considering power (heat) input. For checking the accuracy of temperature prediction, the linear relationship between the power input and maximum temperature obtained in the process (Yeung and Thornton [25]) was used. For this purpose, the power input of the welding process was checked for single and shunted spots, and the maximum temperature could have been estimated. Since this linear relationship is obtained for aluminium alloys, it is also currently reliable to be used for other aluminium alloys.

2.2.2 Experimental Effect of Predicted Cooling Rates

As explained in the previous section, the experimental consideration of predicted cooling rates is performed by three different experiments, in terms of crack generation, tensile-shear strength, and failure type investigation.

2.2.2.1 Crack Generation

The temperature time transformation (TTT) diagram shown in Fig. 10 is indicating the phase transformations of Al 94- Cu 5.2 (wt%) alloy. Although AA2219 includes up to 0.5 % Fe and 0.2 Mn, it is reasonable to use this TTT diagram to consider major phase changes during the time for AA2219 with a composition obtained in Table B1. By using this diagram (Fig. 10), one can estimate the percentage of meta-stable θ' phase and Guinier-Preston (GP) zones during the cooling process. Although all of these meta-stable phases will finally transform to stable α and θ phases after a certain sufficient time, the persistence of θ' during cooling process might increase the brittleness of the nugget microstructure due to semi-coherent nature and lower strength, while the strength of GP zone is in higher levels [26]. Therefore, the possibility of crack generation could be associated with the percentages of meta-stable phases during cooling period.

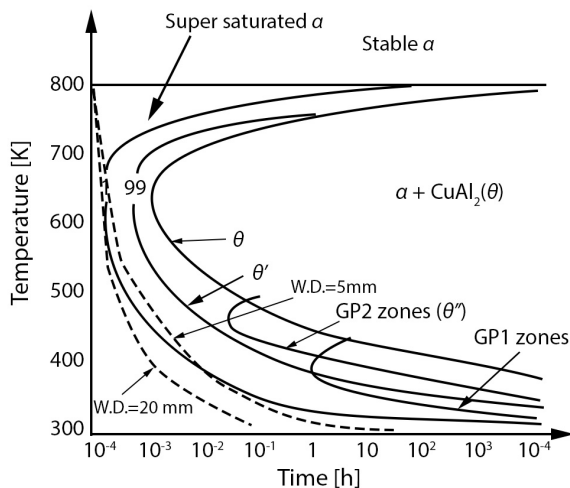


Fig. 10. TTT diagram of Al 94 - Cu 5.2% (wt%) [27], including cooling procedures predicted in Fig. 9.

Comparing the TTT diagram with predicted cooling rates (Fig. 9), shows more percentages of θ' phase inside the nugget with 5 mm welding distance, while very less or zero percentage of meta-stable

phases can be estimated in the nugget zone with 20 mm welding distance according to the TTT diagram in Fig. 10. Therefore, the brittleness and cracking possibility of nugget with a shorter welding distance could be more than nugget with a longer welding distance. This issue is checked experimentally by investigating cracks on SEM images (Fig. 11) in nuggets produced by different welding distances. As seen in Fig. 11a, cracks and even voids have appeared for shorter welding distances inside the nugget while few cracks are observed for longer distances (Fig. 11b).

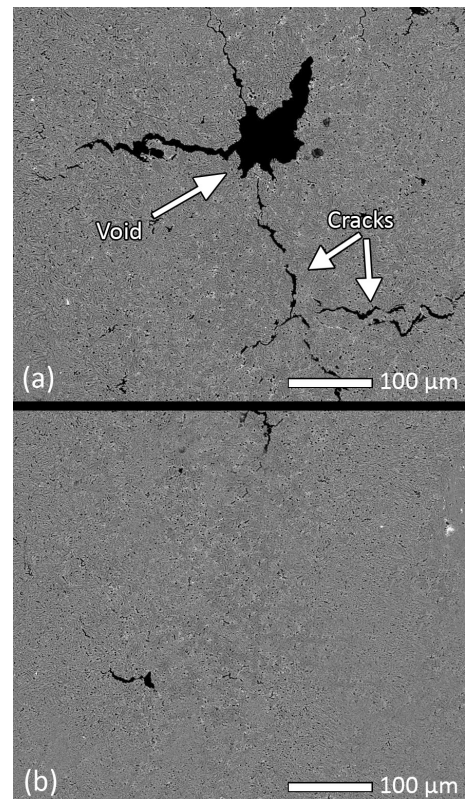


Fig. 11. SEM image of nugget for a) 5 mm and b) 20 mm weld spacing for 25.3 kA and 4 cycles welding current and time respectively, with 150 \times magnification

Although this comparison is not about the effect of different percentages of Cu content in the alloy on brittleness, the difference between Cu content in the phases can effect this phenomenon, as shown in the study by Barlas and Colak [28]. This study could prove the increase in brittleness by increasing rich-copper particles in the content. It shows the concentration of more copper in microstructure increases the possibility of crack appearance. This is a logical conclusion as uneven distribution of copper over Al-Cu alloy changes the mechanical and metallurgical

behaviour of an alloy, as changing the percentages of different phases in the current alloy (α , θ , and θ') does the same. This is again proven in the study by Elatharasan and Kumar [29], about the corrosion analysis of AA 7075 for FSW products, as corrosion usually appeared near Cu inter-metallic particles, or the study by Matesa et al. [30] about the effect of heat treatment on impact energy as precipitation of inter-metallic contents amplified the brittleness.

2.2.2.2 Tensile-Shear Results

Tensile-shear results also show the reduction of the tensile-shear strength of shunted nuggets. Fig. 12 indicates the failure load of the welding nugget under tensile-shear test versus the welding distance for certain welding current. A reduction in failure load is observed by reducing weld spacing. The reduction in welding distance has changed the thermal behaviour of the welding process in the way the shunted nugget and HAZ have become more brittle and easier to fracture. Therefore, it is reasonable to observe such tensile-shear behaviour from shunted nuggets. The behaviour observed in failure types of shunted nuggets after tensile-shear test in the next section is also in agreement with the latter result obtained for the tensile-shear test.

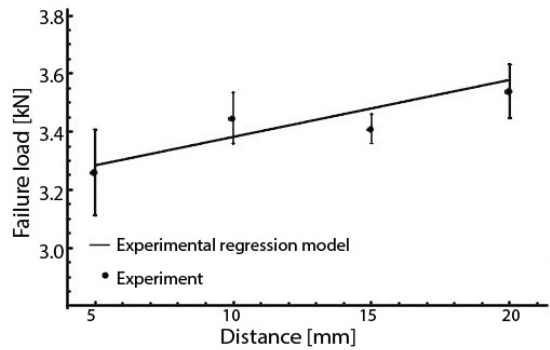


Fig. 12. Comparison of experimental and experimental regression model results of failure load versus weld spacing with 25.3 kA and 4 cycles welding current and time respectively

2.2.2.3 Failure Types of Shunted Nugget

The SEM image of fractured shunted nugget after tensile-shear test with 5 mm welding distance (Fig. 13a) shows the interfacial and brittle failure of the shunted nugget while the presence of cracks inside the nugget is simply observable. This is different for the 20 mm welding distance as shown in Fig.13b. Although the sides of the fractured nugget seem to have a brittle type of crack due to a subtle shunting effect, a pull-out failure is observed. In addition, the

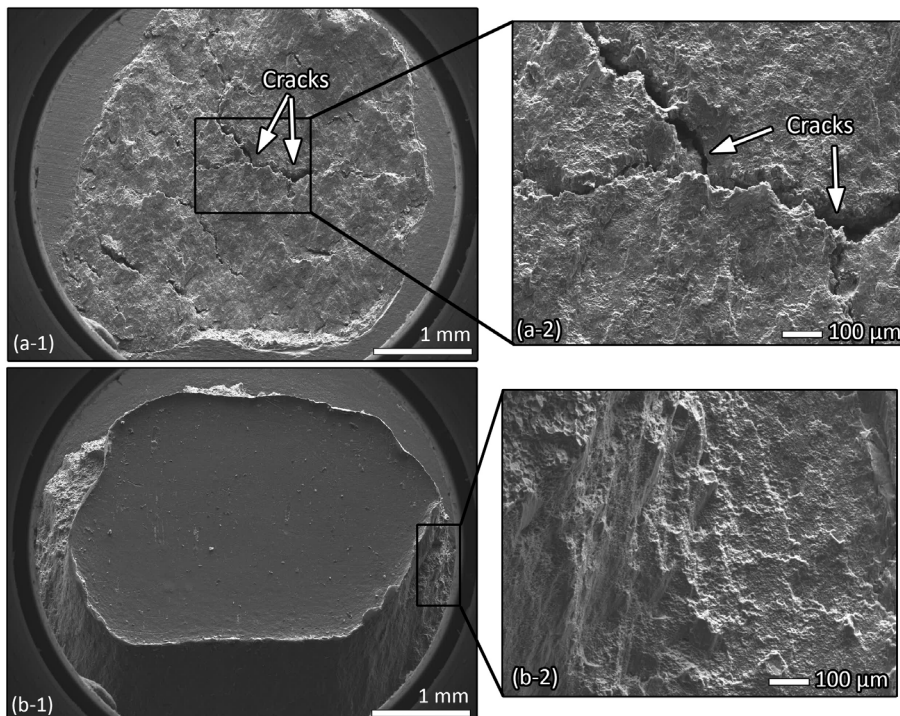


Fig. 13. SEM images showing the failure type of nuggets after tensile-shear test for a) 5 mm, and b) 20 mm welding distance, with 25.3 kA and 4 cycles welding current and time respectively with (1) 25 \times , and (2) 100 \times magnification

presence of initial cracks is rarely observed around the shunted nugget with 20 mm weld spacing.

The main reason for the difference in failure types is associated with the poorer metallurgical and mechanical quality of shunted nuggets. The initial cracks inside the nugget have initiated the interfacial failure inside the nugget for the 5 mm welding distance while the possibility of such phenomenon for the 20 mm welding distance is not considerable due to better mechanical and metallurgical conditions as discussed in previous sections.

3 CONCLUSION

The influence of shunting current on metallurgical and mechanical behaviour of resistance spot welded joints in AA2219 joints was analysed numerically and experimentally. The welding distance was chosen as the main variable of the problem to analyse the shunting effect. Temperature distribution and cooling rates after the application of welding current were checked numerically while verified with comparisons to the experimental results of metallographic micrographs, tensile-shear test results, and SEM images. Numerical and experimental results were in reasonable agreement while the following points are concluded:

- The growth of HAZ volume together with development toward the previous nugget was revealed while this issue was more intense for shorter welding distances.
- According to predicted cooling rates, brittleness of the structure of the shunted nugget and HAZ was discovered and could be associated with the presence of meta-stable incoherent phase during the cooling process for shorter welding distance while SEM images showed more cracks, with weaker tensile-shear strength.
- The checking failure type of shunted nuggets with different welding distances proved the presence of several cracks inside the nugget as a result of brittleness causing interfacial fractures for a shorter distance, while it was a pull-out failure for longer distance (20 mm) without critical cracks around the nugget. This indicates that 20 mm weld spacing could be an appropriate choice to obtain desirable quality for current material and welding conditions while designing limitations of intermittent RSW in terms of spot layout and efficient use of space can be respected.

4 REFERENCES

- [1] Zeyveli, M., Özkan, M., Ulaş, H.B. (2012). An Investigation into the mechanical behavior of the St 37 sheet materials joined with clinching rivet. *International Iron & Steel Symposium*, Karabuk. (in Turkish)
- [2] Hard, A. R. (1948). Preliminary test of spot weld shunting in 24St Alclad. *Welding Journal*, vol. 27, no. 6, p. 491-495.
- [3] Chang, H.S., Cho, H.S. (1990). A study on the shunt effect in resistance spot welding. *Welding Journal*, vol. 69, p. 308-316.
- [4] Senkara, J., Zhang, H. (2000). Cracking in spot welding aluminum alloy AA5754. *Welding Journal*, vol. 79, p. 194s-201s.
- [5] Zhang, H., Senkara, J., Wu, X. (2002). Suppressing cracking in resistance welding AA5754 by mechanical means. *Journal of Manufacturing Science and Engineering*, vol. 124, no. 1, p. 79-85, DOI:10.1115/1.1418693.
- [6] Howe, P. (1994). Spot weld spacing effect on weld button size. *Sheet Metal Welding 6th Conference Proceedings*, paper C03.
- [7] Wang, B.L., Lou, M., Shen, Q., Li, Y. B., Zhang, H. (2013). Shunting effect in resistance spot welding steels – part 1: Experimental study. *Welding Journal*, vol. 92, no. 6, p. 182s-189s.
- [8] Li, Y.B., Wang, B., Shen, Q., Lou, M., Zhang, H. (2013). Shunting effect in resistance spot welding steels – part 2: Theoretical analysis. *Welding Journal*, vol. 92, p. 231s-238s.
- [9] Tsai, C.L., Jammal, O.A., Papritan, J.C., Dickinson, D.W. (1992). Analysis and development of a real time control methodology in resistance spot welding. *Welding Journal*, vol. 70, no. 12, p. 339s-351s.
- [10] Shen, J., Zhang, Y., Lai, X., Wang, P.C. (2011). Modeling of resistance spot welding of multiple stacks of steel sheets. *Materials & Design*, vol. 32, no. 2, p. 550-560, DOI:10.1016/j.matdes.2010.08.023.
- [11] Nied, H.A. (1984). The finite element modeling of resistance spot welding process. *Welding Journal*, vol. 63, no. 4, p. 123s-132s.
- [12] Zhang, W. (2003). Design and implementation of software for resistance welding process simulations. *Journal of Material and Manufacture*, vol. 112, no. 5, p. 556-564, DOI:10.4271/2003-01-0978.
- [13] Kim, J.H., Cho, Y., Jang, Y.H. (2013). Estimation of the weldability of single-sided resistance spot welding. *Journal of Manufacturing Systems*, vol. 32, no. 3, p. 505-512, DOI:10.1016/j.jmsy.2013.04.007.
- [14] Hamed, M., Eisazadeh, H., Esmailzadeh, M. (2010). Numerical simulation of tensile strength of upset welded joints with experimental verification. *Material & Design*, vol. 31, no. 5, p. 2296-2304, DOI:10.1016/j.matdes.2009.12.011.
- [15] Sun, X., Dong, P. (2000). Analysis of Aluminum resistance spot welding processes using coupled finite element procedures. *Welding Journal*, 215s-221s.
- [16] Ghosh, A., Barman, N., Chattopadhyay, H., Hloch, S. (2013). A study of thermal behaviour during submerged arc welding. *Strojniški vestnik - Journal of Mechanical Engineering*, vol. 59, no. 5, p. 333-338, DOI:10.5545/sv-jme.2012.775.

- [17] Zhang, H., Senkara, J. (2011). *Resistance Welding: Fundamentals and Applications*, 2nd ed., CRC Press, Boca Raton.
- [18] Vogler, M., Sheppard, S. (1993). Electrical contact resistance under high loads and elevated temperature. *Welding Journal*, vol. 72, no. 6, p. 231s-238s.
- [19] Kim, S., Lee, W., Kim, D. (2015). One-step distortion simulation of pulsed laser welding with multi-physics information. *International Journal of Simulation Modelling*, vol. 14, no. 1, p. 85-97, DOI:10.2507/IJSIMM14(1)8.291.
- [20] MIL-W-6858D (1978). *Military Specification-Welding-Resistance: Spot and Seam*. Department of the Air Force, Washington.
- [21] Kearns, W.H. (ed.) (1997). *Metals and Their Weldability*, 7th ed., vol. 4, American Welding Society, Miami.
- [22] Saleem, J., Majid, A., Bertilsson, K., Carlberg, T., Ul Islam, N. (2012). Nugget formation during resistance spot welding using finite element model. *World Academy of Science - Engineering and Technology*, vol. 67, p. 588-593.
- [23] Jafari Vardanjani, M., Araee, A., Senkara, J., Jakubowski, J., Godek, J. (2016). Experimental and numerical analysis of shunting effect in resistance spot welding of Al2219 sheets. *Bulletin of the Polish Academy of Sciences: Technical Sciences*, vol. 64, no. 2, p. 425-434, DOI:10.1515/bpasts-2016-0048.
- [24] Yeung, K.S., Thornton, P.H., (1999). Transient thermal analysis of spot welding electrodes. *Welding Journal*, vol. 81, no. 1, p. 1s-6s.
- [25] Ashraf, S. M., Ahmed, S., Riaz, U. (2008). *A Laboratory Manual of Metals and Alloys*, p. 80-81, IK International, New Delhi.
- [26] Porter, D.A., Easterling, K.E., Sherif, M. (2009). *Phase Transformations in Metals and Alloys*, 3rd ed., CRC Press, Boca Raton.
- [27] Barles, Z., Çolak, M. (2014). Evaluation of the influence of upset stage on joint properties of friction welded dissimilar Aluminum-Copper cast alloys. *Strojniški vestnik - Journal of Mechanical Engineering*, vol. 60, no. 12, p. 832-837, DOI:10.5545/sv-jme.2014.1857.
- [28] Elatharasan, G., Senthil Kumar, V.S. (2014). Corrosion analysis of friction stir-welded AA 7075 Aluminium alloy. *Strojniški vestnik - Journal of Mechanical Engineering*, vol. 60, no. 1, p. 29-34, DOI:10.5545/sv-jme.2012.711.
- [29] Mateša, B., Samardžić, I., Dunđer, M. (2014). Heat treatment influence on clad dissimilar joints weakness. *Tehnički vjesnik - Technical Gazette*, vol. 21, no. 5, p. 1035-1040.
- [30] Hou, Z., Kim, I.S., Wang, Y., Li, C., Chen, C. (2007). Finite element analysis for the mechanical features of resistance spot welding process. *Journal of Materials Processing Technology*, vol. 185, no. 1-3, p. 160-165, DOI:10.1016/j.jmatprotec.2006.03.143.
- [31] Sessler, J., Weiss, V. (1966). Aluminum alloy 2219, Muraca, R. F., *Materials Data Handbook*, 2nd ed., Western Applied Research & Development, San Carlos.
- [32] Rooy, E.L., Cayless, R.B.C., Bray, J.W. (1990). Nonferrous alloys and special-purpose materials. *ASM International Handbook Committee, ASM Handbook - Properties & selection*, 10th Ed., vol. 2, ASM, OH.

5 APPENDICES

Appendices include boundary conditions (Appendix A) and different material properties (Appendix B) used in finite element analysis.

A Boundary Conditions

All boundary conditions are provided in this appendix separately.

A1 Electrical Boundary Conditions

Table A1 includes electrical boundary conditions used in FEA section. In Table A1, ϕ_e is the electrical potential applied on the electrode and ρ_{ES} is the electrical contact resistivity between the electrode and sheet, $\Delta\phi_{SS}$ is the voltage drop between the sheets, ρ_{SS} is the electrical contact resistivity between the welds, and $\Delta\phi_{Sh}$ is the voltage drop in the shunting nugget.

Table A1. Electrical boundary conditions

Boundary	Equation
Electrode-sheet Interface [2]	$\frac{1}{\rho} \left(\frac{\partial \phi_{x,y,z}}{\partial z} \right) = \frac{1}{\rho_{ES}} (\phi_e - \phi_{x,y,z}), \quad (A1)$
Faying surface [2]	$\frac{1}{\rho} \left(\frac{\partial \phi_{x,y,z}}{\partial z} \right) = \frac{1}{\rho_{SS}} (\Delta\phi_{SS}), \quad (A2)$
Surfaces exposed to air	$\frac{1}{\rho} \left(\frac{\partial \phi_{x,y,z}}{\partial z} \right) = 0, \quad (A3)$
Perimeter of shunting nugget	$\frac{1}{\rho} \left(\frac{\partial \phi_{x,y,z}}{\partial z} \right) = \frac{1}{\rho_{Sh}} (\Delta\phi_{Sh}). \quad (A4)$

A2 Thermal Boundary Conditions

Table A2 includes thermal boundary conditions used in FEA. In Table A2 k_{ES} and k_{SS} are TCC coefficient of electrode-sheet interface and sheets, respectively; T_W and T_A are water and ambient temperature, respectively; h_W and h_A are thermal convection coefficient of water and air respectively, and n is the surface normal vector.

Table A2. Thermal boundary conditions

Boundary	Equation
Contact surface of electrode and sheet [2]	$-k_{ES} \frac{\partial T_{x,y,z}}{\partial z} = \frac{1}{\rho_{ES}} (\phi_{x,y,z} - \phi_e)^2, \quad (A5)$

Faying surface [2]	$-k_{ss} \frac{\partial T_{x,y,z}}{\partial z} = \frac{1}{\rho_{ss}} (\Delta\phi)^2, \quad (A6)$
Inside electrode exposed to water	$-k_c \frac{\partial}{\partial z} T_{x,y,z} = h_w (T_{x,y,z} - T_w), \quad (A7)$
Sheet, exposed to ambient	$-k \frac{\partial}{\partial z} T_{x,y,z} = h_A (T_{x,y,z} - T_A), \quad (A8)$
Unspecified surfaces	$\frac{\partial T}{\partial n} = 0. \quad (A9)$

B Material Composition Properties

This appendix provides all of the material composition and properties used in FEA and discussion.

B1 AA2219

The material composition of AA2219 identified by SEM is provided in Table B1. The functions or values of material properties used for aluminium alloy 2219 are provided in Tables B2 and B3.

Table B1. AA2219 element composition

Spectrum	Cu	Al	Mg	Mn	Fe
Spectrum 1	5.02	93.53	1.17	0.53	0.25
Spectrum 2	5.25	92.67	1.25	0.56	0.27
Spectrum 3	5.21	92.80	1.29	0.50	0.20

Table B2. Different material properties for AA2219-T6, as a function of temperature

Property	Equation
Density [kg/m ³] [31]	$D(T) \cong 0.0002T^2 - 0.17T + 2858.3, \quad (B1)$
Electrical resistivity [Ω·m] [32]	$\rho(T) = 5.7 \times 10^{-8} \times (1 + 0.0017 \times (T - 293)), \quad (B2)$
Linear thermal expansion [1/K] [31]	$\alpha(T) \cong (0.0063T + 19.708) \times 10^{-6}, \quad (B3)$
Specific heat capacity [J/(kg·K)] [33]	$c(T) \cong -0.0016T^2 + 1.3521T + 567.72, \quad (B4)$
Thermal conduction coefficient [W/(m·K)] [33]	$k(T) \cong 0.1836T + 71.847, \quad (B5)$
Elasticity Modulus [GPa] [33]	$E(T) \cong 2 \times 10^{-7} T^3 - 0.0005T^2 + 0.2253T + 43.386, \quad (B6)$
Yield Strength [MPa] [31]	$\sigma_e(T) \cong 7 \times 10^{-6} T^3 - 0.0102T^2 + 4.0876T + 126.96, \quad (B7)$

Note: T is temperature in K.

Table B3. Important temperature independent properties of AA2219-T6

Parameter	Value
Solidus temperature [°C] [31]	543
Liquidus temperature [°C] [31]	643
Fusion heat [kJ/kg] [32]	389

B2 C18150

The functions or values of C18150 properties are provided in Table B4.

Table B4. Different material properties for C18150, as a function of temperature

Property	Equation
Linear thermal expansion [1/K] [8]	$\alpha_E(T) \cong (3 \times 10^{-6} T^2 + 0.0013T + 15.934) \times 10^{-6}, \quad (B8)$
Electrical resistivity [Ω·m] [8]	$\rho_E(T) \cong (10^{-5} T^2 + 0.0009T + 1.3754) \times 10^{-8}, \quad (B9)$
Specific heat capacity [J/(kg·K)] [8]	$c_E(T) \cong 8 \times 10^{-5} T^2 + 0.0726T + 369.7, \quad (B10)$
Thermal conduction coefficient [W/(m·K)] [8]	$k_E(T) \cong -2 \times 10^{-5} T^2 - 0.1147T + 424.89, \quad (B11)$
Elasticity modulus [GPa] [8]	$E_E(T) \cong 10^{-7} T^3 - 0.0002T^2 - 0.0516T + 150.81, \quad (B12)$
Yield strength [MPa] [8]	83 (B13)

Note: T is temperature in K.

B3 Shunting Nugget

Important properties of shunting nugget are provided in Table B5.

Table B5. Important electrical and mechanical properties of shunting nugget

Parameter	Value
Electrical resistivity [Ω·m]	7.11×10^{-8}
Elasticity modulus [GPa]	75
Yield Strength [MPa]	342

B4 Contact Properties

ECR values are shown in Table B6.

Table B6. ECR values, at room temperature

Parameter	Value
ECR of sheets [Ω]	6.8×10^{-5}
ECR of electrode-sheet [Ω]	8.1×10^{-7}

Chip Formation Mechanism Using Finite Element Simulation

Tahsin Tecelli Öpöz* – Xun Chen

Liverpool John Moores University, General Engineering Research Institute, UK

Prediction of chip form produced during machining process is an important work when considering workpiece surface creation and possible damage caused by chips generated during machining. The paper presents a set of new results of cutting chip formation from the latest finite element method (FEM) model development. Generally, three types of chips (continuous, serrated, and discontinuous chips) are generated during metal machining. The formation of these three types of chips is investigated in relation to various influential factors, such as rake angles and depth of cuts. Progressive damage model with a damage evolution criterion is employed into the FEM model to reduce mesh dependency. It has been demonstrated that finite element simulation is a good tool for the evaluation of chip formation in relation to operational parameters, tool settings as well as material properties.

Keywords: chip formation, finite element method, simulation, fracture energy, metal cutting

Highlights

- A FEM model was developed to predict the chip shape during metal cutting at different machining conditions.
- Fracture energy as a damage evolution criterion was used, and the influence of fracture energy on-chip generation is explored. In addition, the usage of fracture energy as a damage criterion is emphasized.
- Formation of three types of chips (continuous, serrated, and discontinuous chips) was investigated using FEM model.
- Prediction of chip shapes and morphologies have been very promising with increasing machining volume of industrial components in the manufacturing industry. Therefore, it is indispensable to predict machined part quality using simulation techniques to reduce costly experimental tests and also to evaluate mechanical parameters such as stresses, strains, and temperatures, which are difficult to measure using experimental tests.

0 INTRODUCTION

Chip formation during machining processes is a material removal process in which the materials are removed from the workpiece in the form of numerous tiny chips. To understand chip formation regarding the chip types, shapes as well as the stress/strain distribution would help the prediction of cutting force and thermal behaviour to avoid unexpected vibration and thermal damage. To do this, the finite element models of machining processes are very popular for simulating chip formation [1] to [15]. The reason is to minimize labour cost and save time by reducing expensive experimental tests. In contrast, the estimation of some physical phenomena such as the distribution of stress and strain under machining conditions is quite difficult to accomplish with experimental tests. Finite element method (FEM) provides a convenient method to visualise material performance under different machining conditions. Therefore, the prediction of chip types and chip shapes under different operating conditions is one of the significant benefits provided by FEM simulations.

In metal cutting processes, often three types of chip formation occur (continuous chips, serrated chips, and discontinuous chips), which are produced as a result of the cutting deformation mechanism, operating parameters, and workpiece mechanical

and thermal properties. The continuous chip is often considered to be an ideal chip that generates stable cutting forces; however, it is not desired for automated machining because the continuous chips may obstruct the machining process, which may lead to unpredictable damage on the machined surface, cutting tool or machine tool. To minimize these problems, serrated chips that are easier to break and remove are preferred during machining [1] and [2], so, predicting the cutting conditions which lead to a serrated chip has become increasingly important.

In some literature, serrated chips are called saw-tooth shape or continuous segmented chips. Increased segmentation on continuous chips eventually leads to serrated chips. It is common knowledge that segmentation during chip formation is triggered by two phenomena: the formation of the adiabatic shear band and the crack initiation mechanism in a primary shear zone. Adiabatic shear banding is known as the localization of the plastic deformation into the narrow bands which occur during the high-rate plastic deformation and often lead to shear fracture [3]. Serrated chips are formed as a result of adiabatic shear bands [4]. In addition to adiabatic shear band deduced segmentation, the serrated chip is formed when a chip fractures at the primary deformation zone due to overstrain and the interfaces of the chip segments are welded immediately after the fracture by compression

and high chemical activity, and a crack is generated according to material failure criterion. After the crack initiation, it is propagated in the direction of the shear zone into the chip, which enables segmentation [5]. The generation of segmentation in FEM modelling is achieved by employing either failure criterion or modified constitutive model regarding strain, strain rate, and temperature as a function of flow stress into the finite element model. Deployment of flow stress without failure criterion is highly necessary, coupled with continuous adaptive remeshing to mitigate the distortion of the element taking place due to high plastic deformation at the primary and secondary deformation zones, ultimately, adaptive remeshing also enable to complete solution without termination of the model caused by excessive element distortion during computation.

Aurich and Bil [5] developed a 3D chip formation model by introducing Rhim's flow stress equations to account for thermal softening, adaptive remeshing to deal with element distortion and fracture mechanic-based chip separation criterion. They found a significant effect of the applied method on predicted chip shape; adaptive remeshing alone leads to continuous chip, thermal softening generates brief segmentation, and fracture leads to severe segmentation. Calamaz et al. [6] studied the influence of the strain softening phenomenon and friction law on the shear location generating serrated chips. Bäker et al. [7] developed a two-dimensional orthogonal cutting process considering adiabatic shearing effects and generated segmented chips by employing a remeshing technique to the model.

Segmentation of chips is also dependent on operating parameters; segmented continuous chips are often produced at high cutting speeds [8] and the degree of segmentation increases with increasing feed or uncut chip thickness [4]. The tendency to form segmented chips is found to be smaller at the lower cutting speed [7]. This indicates the complexity of chip formation with a large number of influential factors. Regarding material property effects, the lower the elastic modulus is, the higher the degree of segmentation and segmentation time would be. A possible explanation is that a larger amount of stored elastic energy eases the shearing, or that plastic shearing is preferred as elastic deformation of the region left of the shear band is energetically unfavourable.

The earliest FEM simulation on chip formation was conducted by Strenkowski and Carroll [9], and they achieved serrated chips by using the chip separation criterion. To date, chip separation was

achieved either by previously defined separation criteria or by the fully plastic flow of material using an adaptive remeshing technique employed to the FEM model. Finite element analysis of chip formation can be modelled either by using Eulerian formulation or Lagrangian formulation. In a Eulerian-based model, no need to define chip separation criterion exists; cutting is simulated from the steady state, but it is required to define the initial chip shape, so it is not very realistic for investigating machining chip formation. Conversely, the Lagrangian formulation can allow simulating chip formation without defining initial chip shape from incipient to the steady state. It gives more realistic results as a prediction of chip geometry and other machining-deduced phenomenal parameters, such as stress, strain, and force. However, the Lagrangian formulation needs a chip separation criterion to enable chip separation from the workpiece [10]. Huang and Black [11] evaluated available chip separation criteria and divided them into two categories: (a) physical criteria such as effective plastic strain and strain energy density; and (b) geometrical criteria such as distance tolerance. They concluded that neither the geometrical nor physical criteria simulated machining process correctly and suggested a combination of geometric and physical criteria for FEM simulation of machining. Often, parting lines, or sacrificial layer, are used together with a failure criterion to allow chip separation from the workpiece when the updated Lagrangian formulation is used.

In early FEM models of chip formation, a node release technique was based on distance tolerance; effective plastic strain and strain energy density [10] and [12] were employed to the model. According to node release technique, an element in front of the tool is separated following the nodal release when the defined criterion is satisfied. Recently, three other methods have been utilized to generate chips: material failure (damage) models based on fracture mechanics, flow stress models which take thermal softening and straining hardening into account with continuous adaptive remeshing, and Arbitrary-Lagrangian-Eulerian (ALE) adaptive meshing. The first one considers the fracture mechanic concept to initiate a crack and followed by crack growth to form chips according to degradation criterion. The last two produce chips due to the plastic flow of material over the tool tip without crack formation. Moreover, the material failure model and adaptive remeshing are used together to achieve further improvement in chip formation in some models. Particularly, for the formation of serrated chips, the inclusion of a material

failure model and adaptive remeshing method into FEM model is highly crucial.

Shet and Deng [13] developed the orthogonal cutting process under plane strain conditions in Abaqus/Explicit. Explicit FEA is generally preferred in cutting simulation because explicit analyses guarantee to converge. Large deformation was prevented by an updated Lagrangian formulation. Movahhedy et al. [14] developed an orthogonal cutting model by using ALE approach with strain rate and temperature dependent constitutive equations. Özel and Zeren [15] developed a finite element model with ALE adaptive meshing without using chip separation criteria; chip was generated by the plastic flow of workpiece material. Sima and Özel [4] simulated the serrated chips without using damage or failure models by adiabatic shearing due to temperature –dependent flow softening with continuous remeshing in Deform 2D.

A progressive failure model needs a properly defined damage evolution technique. In Abaqus, damage evolution can be conducted by defining either equivalent plastic displacement or fracture energy dissipation [16] to [19]. Ambati and Yuan [17] investigated the mesh-dependence in cutting simulation by using the progressive failure model with plastic displacement as the damage evolution criterion. They analysed various chip shapes by using different plastic displacement values and found that chip transition occurs from continuous to segmentation with increasing feeds. Mabrouki et al. [2] investigated the characteristics of chip morphology and chip microstructures during cutting operation under high loading. Mabrouki et al. [18] also investigated the dry cutting of an aeronautic aluminium alloy and developed the numerical model based on the Johnson-Cook law incorporating with material damage evolution by using a fracture energy model. The feed rate and cutting velocity were used as the simulation variables. Their experimental results showed that the higher cutting speed results in increasing segmentation frequency. Chen et al. [20] employed energy density based failure criteria to investigate the flow stress and failure strain behaviour in orthogonal cutting of aluminium alloys.

In metal cutting, simulations results are often considered as dependent on mesh size so called mesh sensitivity. In cutting simulation at large deformation when using a progressive failure model in Abaqus, element characteristics, length could be increased to reduce the mesh dependency [21]. In the determination of element size, there are two main constraints that should be taken into account: (1)

mesh element size should be relatively high to obtain a reasonable computation time and (2) the results should be similar to the experimental results in terms of chip morphology and cutting force generation [21]. It must be noted that the influence of mesh size (mesh sensitivity) is not investigated in this paper; a constant element mesh size of 1 μm in length is used for the chip formation.

1 FINITE ELEMENT SIMULATION

1.1 Simulation Environment and Boundary Conditions

In this paper, all simulations are performed in Abaqus/Explicit FEM software. CPE4RT elements, 4-node bilinear displacement, and temperature, reduced integration with hourglass control, are used in the workpiece model. Element size in cutting region (top section of the workpiece) is 1 μm in length. Although the cutting tool is meshed, a rigid body constrained is applied to the cutting tool in the simulations. Cutting tool speed of 300 m/min is used for all simulations. Workpiece boundary conditions are shown in Fig. 1.

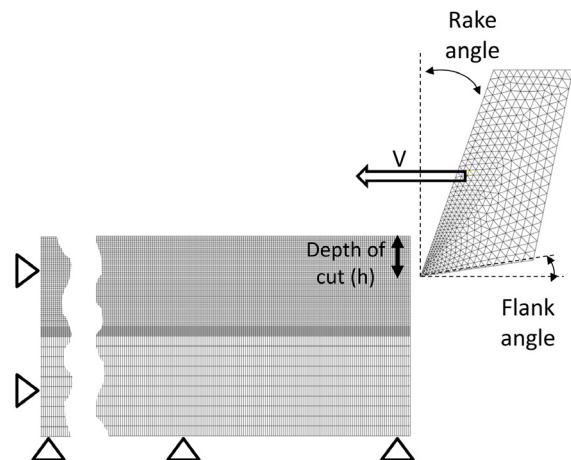


Fig. 1. An example of tool and workpiece model with positive tool rake angle

The penalty contact method with a constant friction coefficient ($\mu = 0.2$) is applied between the tool and workpiece. Johnson-Cook (JC) flow stress parameters are given in Table 1. The simulation is modelled considering the adiabatic heating effect on the analysis. Element deletion technique is used to allow element separation to form a chip. In the present study, no sacrificial layer is used to allow chip separation. The ALE adaptive meshing technique is used to maintain the mesh quality throughout the simulation and to reduce element distortion in cases of

extreme deformation. Damage criterion and element deletion is applied to entire workpiece elements, so that it might be possible to simulate crack initiation along a chip's primary shear region. However, one drawback without a sacrificial layer, the simulation might be terminated if the elements distortions increase excessively due to inconvenient damage parameters. In addition, without a sacrificial layer, some elements in the chip separation region where the tool comes into contact with workpiece extend too much as seen black lines in Fig. 5c in a later section.

Table 1. JC flow stress parameters for workpiece (A2024-T351) [18]

Parameters	values
A [MPa]	352
B [MPa]	440
n	0.42
C	0.0083
m	1
Density, ρ [kg/m ³]	2700
Elastic modulus, E [GPa]	73
Poisson's ratio	0.33
Specific heat, C_p [J/(kg·°C)]	$C_p = 0.557T + 877.6$
Expansion, α_d [$\mu\text{m}/(\text{m}\cdot^\circ\text{C})$]	$\alpha_d = 8.9 \times 10^{-3}T + 22.2$
T_{melt} [°C]	520
T_{room} [°C]	25
Heat fraction coefficient	0.9

1.2 Constitutive Model

In the present study, a rate-dependent JC model [22] was used. Rate dependent yield is required to model materials' yield behaviour accurately when the yield strength depends on the strain rate. The JC hardening method describes the flow stress of a material with the product of strain, strain rate, and temperature effect is defined in Eq. (1).

$$\bar{\sigma} = \left[A + B(\bar{\epsilon})^n \right] \left[1 + C \ln \left(\frac{\dot{\bar{\epsilon}}}{\dot{\bar{\epsilon}}_0} \right) \right] \left[1 - \left(\frac{T - T_{room}}{T_{melt} - T_{room}} \right)^m \right], \quad (1)$$

where $\bar{\sigma}$ is the equivalent stress, A is the initial yield strength [MPa] of the material at room temperature, B is the hardening modulus [MPa], $\bar{\epsilon}$ is the equivalent plastic strain, n is the work-hardening exponent, C is the coefficient dependent on the strain rate, $\dot{\bar{\epsilon}}$ is the equivalent plastic strain rate, $\dot{\bar{\epsilon}}_0$ is the reference strain rate, m is the thermal softening coefficient. T_{room} and T_{melt} represent the room temperature and melting temperature, respectively. The flow stress curves of

Johnson-Cook model for the material properties used in the simulation are shown in Fig. 2.

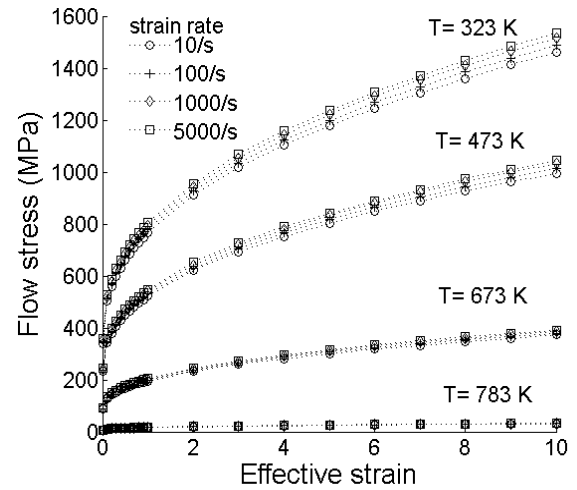


Fig. 2. Flow stress curves with temperature and strain rate data using JC model

1.3 Damage Initiation

The damage model proposed by Johnson and Cook [23] is used in conjunction with JC flow stress model. The JC damage model is suitable for high strain rate deformation, such as high-speed machining. The JC damage model was claimed to result in more realistic simulations compared to other models (e.g. Wilkins, the maximum shear stress, the modified Cockcroft-Latham, the constant fracture strain, and the Bao-Wierzbicki fracture models) [24]. According to JC damage criterion, the general expression for the fracture strain is given in Eq. (2).

$$\bar{\epsilon}^f = \left(D_1 + D_2 \exp D_3 \frac{\sigma_m}{\bar{\sigma}} \right) \left(1 + D_4 \ln \frac{\dot{\bar{\epsilon}}}{\dot{\bar{\epsilon}}_0} \right) \times \left[1 + D_5 \left(\frac{T - T_{room}}{T_{melt} - T_{room}} \right) \right], \quad (2)$$

JC damage parameters represent: D_1 initial failure strain, D_2 exponential factor, D_3 triaxiality factor, D_4 strain rate factor, and D_5 temperature factor, where $\bar{\epsilon}^f$ the equivalent strain to fracture is, σ_m is the average of the three normal stresses and $\bar{\sigma}$ is the von Mises equivalent stress.

Damage initiation begins according to the standard damage law,

$$w = \sum \frac{\Delta \bar{\epsilon}}{\bar{\epsilon}^f}, \quad (3)$$

where $\Delta \bar{\epsilon}$ is the accumulated increment of equivalent plastic strain during an integration step, w is damage parameter to initiate failure when it equals to 1. Due to the use of progressive damage, damage initiation is followed by damage evolution criterion which governs the propagation of damage until an ultimate failure happens.

The JC damage parameters used for the present study are given in Table 2. The temperature factor D_5 is null which means that the temperature has no effect on the damage initiation during the cutting of the aluminium alloy A2024-T351 [18].

Table 2. JC damage parameters for A2024-T351 [18]

D_1	D_2	D_3	D_4	D_5
0.13	0.13	-1.5	0.011	0

1.4 Damage Evolution Based on Fracture Energy Dissipation

The stress-strain relationship defined in the material properties table cannot represent the material behaviour properly after the initiation of damage. Usage of stress-strain relation through damage propagation results in significant mesh dependency due to strain localization [25]. To mitigate the mesh dependency, a damage evolution technique with linear softening based on the fracture energy model proposed by Hillerborg et al. [26] is used in this paper. Hillerborg defines fracture energy, G_f (with a unit of J/m² or N/m in Abaqus), which is required to obtain a unit area of crack as a material parameter. This governs the softening of material according to a stress-displacement response after damage initiation rather than a stress-strain response [25]. To determine the stress-displacement response, a characteristic length (L), which is the typical length of line in the first-order element associated with an integration point, is defined. Hillerborg’s fracture energy is defined in Eq. (4).

$$G_f = \int_{\bar{\epsilon}_0^{pl}}^{\bar{\epsilon}_f^{pl}} L \sigma_y d\bar{\epsilon}^{pl} = \int_0^{u_f^{pl}} \sigma_y du^{pl}, \quad (4)$$

where, \bar{u}^{pl} is the equivalent plastic displacement as the fracture work conjugate of the yield stress after the onset of damage. Linear evolution of the damage is assumed. Before damage initiation $\bar{u}^{pl} = 0$; after damage initiation $\bar{u}^{pl} = L\bar{\epsilon}^{pl}$. In the Abaqus FEM model, fracture energy is an input parameter which is required to be known before simulation. Thus, following the damage initiation, the damage variable increases according to Eq. (5).

$$D = \frac{L\bar{\epsilon}^{pl}}{\bar{u}_f^{pl}} = \frac{\bar{u}^{pl}}{\bar{u}_f^{pl}}, \quad (5)$$

where the equivalent plastic displacement at failure is computed as in Eq. (6).

$$\bar{u}_f^{pl} = \frac{2G_f}{\sigma_{y0}}, \quad (6)$$

where σ_{y0} is the value of yield stress at the time when the failure criterion is reached. Stress-strain behaviour of a material undergoing damage is illustrated in Fig. 3. The solid curve in the figure represents the damaged stress-strain response, while the dashed curve is the response in the absence of damage. In the figure, σ_{y0} and $\bar{\epsilon}_0^{pl}$ are the yield stress and equivalent plastic strain at the onset of damage, and $\bar{\epsilon}_f^{pl}$ is the equivalent plastic strain at failure; that is when the overall damage variable reaches the value $D=1$. Then the concerned element is removed from the computation when $D=1$ in every integration point, with the element deletion technique provided by Abaqus software. Overall damage variable, D , can be obtained from the simulation output as a degradation variable, $SDEG$, and can be set to a value lower than 1 considering the course of simulation [20]. The SDEG value in this study is a default 0.99 in Abaqus to ease the element deletion.

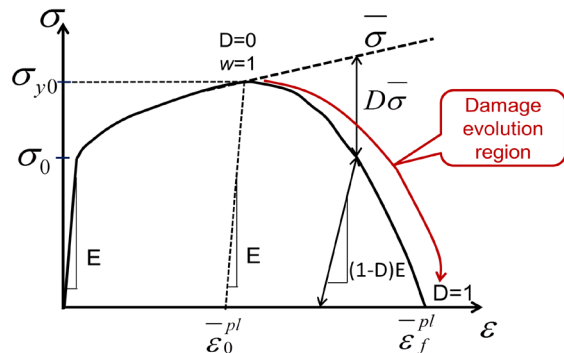


Fig. 3. Stress-strain curve illustrates damage evolution for progressive damage model [20]

The strength of the material along the curve can be calculated by Eq. (7).

$$\sigma = (1 - D)\bar{\sigma}, \quad (7)$$

where σ and $\bar{\sigma}$ are the effective and apparent stress and D is the accumulated damage. In addition, the elastic modulus decreases due to damage [26]. Elastic modulus after damage initiation \tilde{E} can be calculated by Eq. (8).

$$\tilde{E} = (1 - D)E. \quad (8)$$

The difficulty in damage evolution is due to the requirement of a previously known fracture energy value as an input parameter. The fracture energy required for the damage evolution can be determined by Eq. (9).

$$G_f = K_{IC}^2 \left(\frac{1 - \nu^2}{E} \right) \text{ (Plane strain)}. \quad (9)$$

Evaluated fracture energy is related to fracture toughness K_{IC} , Young's modulus E , and Poisson's ratio ν . As an important criterion, fracture toughness (K_{IC}) indicates the resistance to crack growth and can be used to predict fracture initiation. High plastic deformation in the machining process causes variation in fracture toughness. He and Li [27] investigated the influences of fracture toughness on strengthening and degrading aspects. With the increasing number of defects (micro-cracks and growth), some physical characteristic of materials are also changed such as elastic modulus as recalculated in Eq. (8) and toughness as well.

Measurements of K_{IC} are made using specimens containing very sharp fatigue pre-cracks. However, there are constraints on specimen dimension and crack length. These limitations make it difficult to obtain valid K_{IC} values for materials [28]. The experimental evidence shows that the fracture toughness of metals is dependent on the size of the specimen during the test. Although at the bigger size of the test specimen, fracture toughness was calculated as being more stable, whereas, it is dramatically decreasing while the test specimen size is decreasing to lower values as shown in Fig. 4. When chip formation is considered, the chip size is relatively small where the fracture initiated and propagated. So it is not realistic to use K_{IC} values measured at nominal test specimen size, which is relatively higher than required for chip formation. In addition, K_{IC} is not a constant property; it is varying depending on the fracture mode of material including the micro-crack formation, element dislocation, and subsequent crack growth along the fracture line. Mabrouki et al. [18] employed fracture energy method into the FEM model by using K_{IC} values measured at a nominal size to estimate the fracture energy required as a damage evolution criterion. G_f values defined in [18] is 16711 N/m for the opening mode of fracture and 8251 N/m for the shearing mode of fracture, which are estimated from Eq. (9). A detail explanation of opening and shearing mode is provided in [18]. In this paper, fracture energy

required for damage evolution is not determined from K_{IC} values; a range of G_f values from 250 N/m to 20000 N/m is used to emphasize the influences of G_f value on the chip type and morphology. Therefore, significant changes have been observed in the chip type and shape.

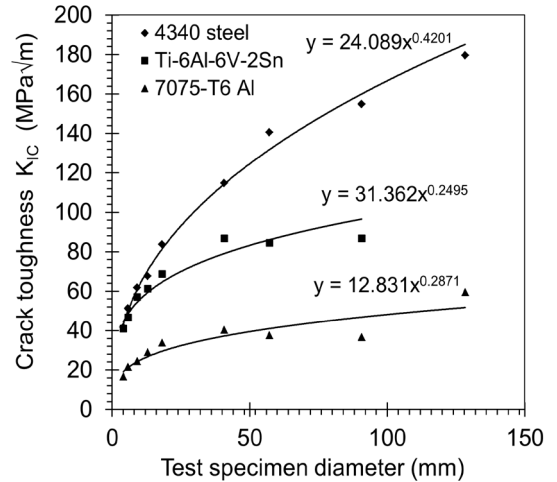


Fig. 4. Crack toughness (K_{IC}) versus section size [29]

1.5 Temperature Rise Due to Adiabatic Process

In high-speed machining, heat produced due to local energy dissipation may not have adequate time to diffuse away, and local heating will take place in the active plastic zones and sliding frictional interface. Thus, the temperature rise in the chip can be estimated with the adiabatic heating condition. The temperature increase is calculated directly at the material integration points according to the adiabatic thermal energy increases caused by inelastic deformation [13], [16] and [30]. Heat conduction has not a contribution in an adiabatic analysis. Volumetric heat flux due to plastic straining can be calculated by Eq. (10).

$$\dot{q} = \eta \dot{\sigma} \varepsilon, \quad (10)$$

where \dot{q}_p is the heat flux that is added to the thermal energy balance, η is the inelastic heat fraction (assumed constant as a default value of 0.9 in Abaqus), σ is the effective stress, and $\dot{\varepsilon}^p$ is the plastic strain rate. Also, the heat equation solved at each integration point is given in Eq. (11).

$$\rho C_p \frac{\Delta T_p}{\Delta t} = \dot{q}_p, \quad (11)$$

where ρ is the material density and C_p is the specific heat. Considering both equations shown above, the

local temperature rise due to plastic deformation can be given in Eq. (12).

$$\Delta T_p = \eta \frac{\sigma \dot{\epsilon}^p \Delta t}{\rho C_p} \quad (12)$$

Similarly, heat generated by friction forces (Eq. (13)) lead to a rise in temperature ΔT_f during a period of Δt .

$$\dot{q}_f = \eta_f J \tau \dot{\gamma} = \rho C_p \frac{\Delta T_f}{\Delta t} \quad (13)$$

Then temperature rise due to sliding friction between tool and chip interfaces is determined by Eq. (14):

$$\Delta T_f = \eta_f \frac{J \tau \dot{\gamma} \Delta t}{\rho C_p} \quad (14)$$

where, η_f is the fraction of dissipated energy caused by friction and assumed as 0.9, J the equivalent heat conversion factor, τ shear stress computed by Coulomb's law and $\dot{\gamma}$ slip strain rate.

2 FEM SIMULATION RESULTS

Chip formation simulations were performed with gradually increasing fracture energy, G_f , two different depth of cuts ($h_1 = 20 \mu\text{m}$ and $h_2 = 50 \mu\text{m}$) and four rake angles ($\gamma_1 = 22^\circ$, $\gamma_2 = 0^\circ$, $\gamma_3 = -30^\circ$, $\gamma_4 = -45^\circ$) in Abaqus/Explicit.

2.1 Fracture Energy Influence on Chip Formation

A simulation with gradually increasing fracture energy, G_f , was performed to demonstrate the influence of fracture energy which is used as damage evolution criterion. Due to difficulties in knowing the exact value of the fracture energy at the smaller thickness, chip formation have been simulated with different values of fracture energy (250 N/m, 2500 N/m, 10000 N/m, and 20000 N/m) while uncut chip thickness remains 20 μm . The results shown in Fig. 5 demonstrate that increasing fracture energy (2500 N/m, 10000 N/m and 20000 N/m) leads to the generation of the continuous chips, as shown in Figs. 5b-d while lower values of fracture energy (250 N/m) results in discontinuous chip generation as shown in Fig. 5a. Furthermore, chip shapes tend to be straighter with increasing fracture energy (Figs. 5b to d) while lower fracture energy result in more curled chips, as shown in Fig. 5b. Therefore, fracture energy is one of the key factors as a damage evolution criterion to determine the chip generation behaviour during cutting simulation.

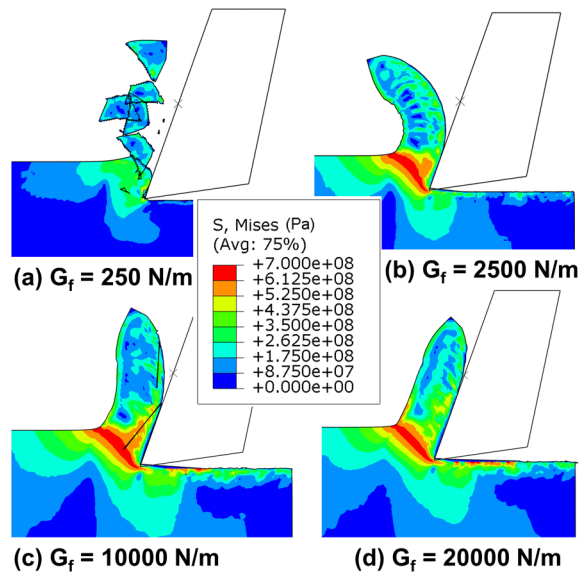


Fig. 5. Chip simulations with varying fracture energy criterion for damage evolution ($h = 20 \mu\text{m}$)

2.2 Influence of Depth of Cut on Chip Type

The depth of cut is also one of the influential parameters for the determination of chip type. To show the depth of cut influence, two different simulations with different depths of cut were made. A continuous chip without forming segmentation along the chip free edge is generated when uncut chip thickness is set to 20 μm as shown in Fig. 6a. In contrast, the serrated chip is generated when the depth of cut is about 50 μm under the same simulation conditions as shown in Fig. 6b. The reason of serrated chip formation at higher uncut chip thickness is probably shear stress developed in the primary shear zone increasing dramatically due to intensive straining in this region. With the increasing strain at the primary shear zone, material strength is weakened due to the predefined

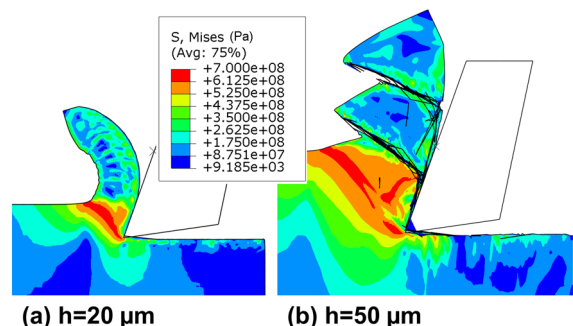


Fig. 6. Chip formation with different depth of cuts ($G_f = 2500 \text{ N/m}$)

failure criterion and crack initiation in the primary shear region. As a result, each segment formed due to plastic flow and formed sharp-edged serrated chips as shown in Fig. 6b. Experimental results obtained in [31] support the present simulations, i.e. the tendency to produce segmented chips is increasing with increased feed.

2.3 Influence of Rake Angle on Chip Formation

The formation of continuous, serrated and discontinuous chips was simulated by using the different tool rake angles. Though previous research [4] did not show a significant effect of rake angle on the degree of segmentation, it has a significant influence in low values of the depth of cut. Fig. 7 shows that the rake angle plays a crucial role in determining chip type. A continuous chip with a little segmentation is generated with a positive rake angle of 22° (Fig. 7a); a serrated or saw-tooth chip is generated with a zero rake angle tool (Fig. 7b); a discontinuous chip is generated with a negative rake angle of -30° (Fig. 7c); and a different discontinuous chip with two split parts is generated with a negative rake angle of -45° (Fig. 7d). Obviously, the tendency from continuous to discontinuous chip formation is increasing while the rake angle is moving from positive to negative values. As a result of the negatively increasing tool rake face, compression on the chip increases. This higher compression results in tearing stress increasing in the primary shear region, which in turn promotes segmentation, then eventually separation of each

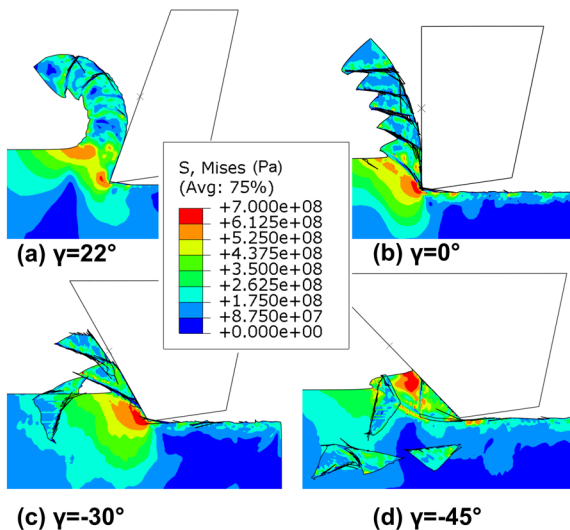


Fig. 7. Chip shape alteration with varying rake angles ($G_f = 1500 \text{ N/m}$ and $h = 20 \mu\text{m}$)

segment. Since material strength in the primary shear region decreased with increasing straining, ultimate fracture occurs when the predefined damage evolution criterion is satisfied. Experimental results in [31] confirm that the chip shape changes from continuous to segmented chip and also segmentation degree increases with the smaller rake angle. In [31], there was not any experimental result for the negative rake angle.

2.4 Chip Fracture Development due to Increasing Chip Length

Chip fracture is observed in serrated chip formation simulation with simulated chip length is increasing with increasing simulation time as shown in Fig. 8. After reaching a certain length, the chip is fractured from the weak residual shear zone since with the increasing chip length chip curvature increases than elements in the weakened residual shear zone no longer withstand carrying the frontier portion of the chip then fracture will occur as shown in Fig. 8b.

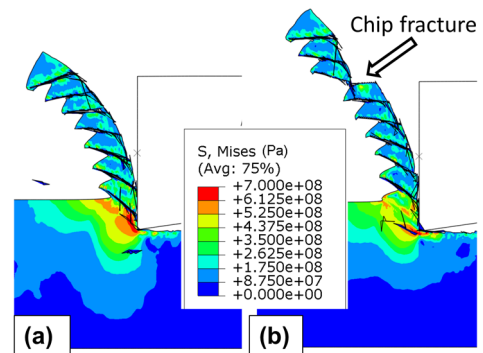


Fig. 8. Chip fracture during serrated chip formation at a) $2.85e-5 \text{ s}$ and b) $3.42e-5 \text{ s}$, ($G_f = 1500 \text{ N/m}$, $h = 20 \mu\text{m}$, $\gamma = 0^\circ$)

2.5 Temperature Changes in Chip Formation

Temperature increases across the shear band and high deformation area due to energy consumption in plastic deformation and friction. It is observed that temperature rises mainly in the chip region, with maximum values localized along the tool-chip interface and at the fracture zone. Fig. 9 demonstrates temperature variation on chips with three different tool rake angles. Temperature-affected region between the workpiece top surface layer and the sub-surface layer increases while the tool rake face angle changes from positive to negative values. The temperature rise in the workpiece is very small. Overall temperature distribution in the chip is determined by plastic work

dissipation in the chip rather than friction along the tool-chip interface [13].

2.6 Plastic strain

Equivalent plastic strain (PEEQ) lies in the range of 0.8 to 3 in most of the segmented section where intense localized deformation occurs; however, PEEQ reaches the value of 6 where elements are distorted or broken in the chip. The PEEQ results are consistent with the results obtained in [32] in which the simulations were performed for the machining of Ti6Al4V at 500 m/min.

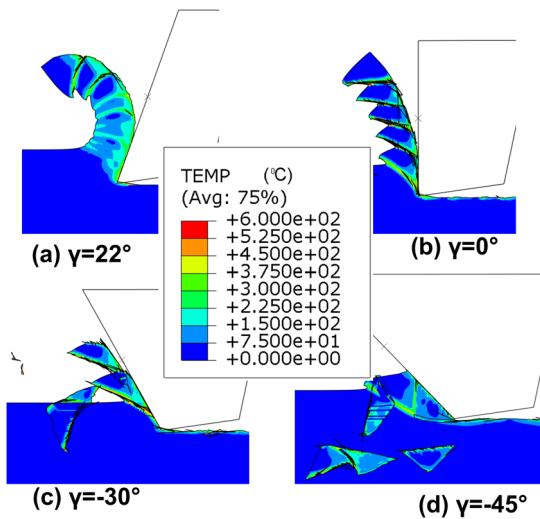


Fig. 9. Temperature changes during chip formation ($G_f = 1500 \text{ N/m}$, $h = 20 \mu\text{m}$)

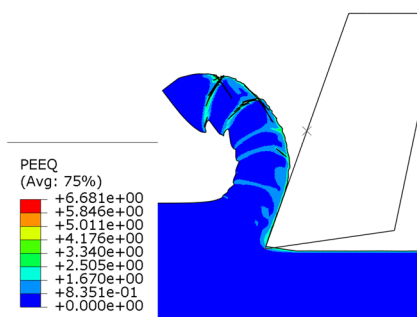


Fig. 10. Equivalent plastic strain demonstration ($\gamma = 22^\circ$, $G_f = 1500 \text{ N/m}$, $h = 20 \mu\text{m}$)

3 CONCLUSIONS

With the latest FEM models, a set of new results has been presented on the effects of influential material parameters and processing parameters on chip formation.

The morphology of cutting chips (continuous chip, discontinuous chip, and serrated chips) is simulated in Abaqus/Explicit finite element software. The Johnson-Cook constitutive material model is used in conjunction with the Johnson-Cook progressive damage model by using fracture energy as a damage evolution criterion. In addition, the fracture energy-based damage evolution criterion is integrated into the model to reduce mesh dependency. According to simulation results, the fracture energy dissipation used for damage evolution is an influential factor in chip formation. As it was explained in preceding sections, the very lower values of fracture energy lead to discontinuous chip formation whereas the increasing values of fracture energy result in continuous chips with straighter chip shapes. Another essential factor in chip formation is the depth of cut. Though previous research did not demonstrate the significant effect of rake angle on the degree of chip segmentation, it has been found that a significant influence at smaller depths of cut. According to simulation results in this paper, with the increasing depth of cut chip type tends to become more segmented and finally serrated chips are generated. However, a great difficulty was encountered in the simulation with smaller depths of cut down to less a micron level due to the mesh size and computational power. In addition, the effects of rake angle in chip formation are simulated. Generated chips tend to be serrated and eventually the discontinuous type when the tool rake angle is moving from positive values to negative values. These findings are significant when a grinding case is to be studied, in which the depth of cut is smaller, and rake angles are much larger on the negative side.

In addition to the chip type and shape information obtained from the finite element simulation results, some mechanical parameters such as stress, strain, strain rate, temperature rise, which are very difficult to measure on the experimental test, can be obtained via finite element modelling of chip formation process.

Simulation results show that discontinuous chips are generated with very low fracture energy, while continuous chips are generated with increasing fracture energy. The chip shape is also changing from curling to straight with increasing fracture energy. High depth of cut results in serrated chip while the low depth of cut results in the continuous chip. Moreover, the transition from continuous to the discontinuous chip is observed when tool rake angle moves from positive values to negative values.

4 REFERENCES

- [1] Xie, J.Q., Bayoumi, A.E., Zbib, H.M. (1996). A study on shear banding in chip formation of orthogonal machining. *International Journal of Machine Tools Manufacture*, vol. 36, no. 7, p. 835-847, DOI:10.1016/0890-6955(95)00016-X.
- [2] Mabrouki, T., Courbon, C., Zhang, Y., Rech, J., Nélías, D., J., Asad, M., Hamdi, H., Belhadi, S., Salvatore, F. (2016). Some insights on the modelling of chip formation and its morphology during metal cutting operations. *Comptes Rendus Mécanique*, vol. 344, no. 4-5, p. 335-354, DOI:10.1016/j.crme.2016.02.003.
- [3] Batra, R.C., Liu, D.S. (1990). Adiabatic shear banding in dynamic plane strain compression of a viscoplastic material. *International Journal of Plasticity*, vol. 6, no. 2, p. 231-246, DOI:10.1016/0749-6419(90)90023-8.
- [4] Sima, M., Özel, T. (2010). Modified material constitutive models for serrated chip formation simulations and experimental validation in machining of titanium alloy Ti-6Al-4V. *International Journal of Machine Tools Manufacture*, vol. 50, no. 11, p. 943-960, DOI:10.1016/j.ijmachtools.2010.08.004.
- [5] Aurich, J.C., Bil, H. (2006). 3D finite element modelling of segmented chip formation. *CIRP Annals – Manufacturing Technology*, vol. 55, no. 1, p. 47-50, DOI:10.1016/S0007-8506(07)60363-1.
- [6] Calamaz, M., Coupard, D., Nouari, M., Girot F. (2011). Numerical analysis of chip formation and shear localisation processes in machining the Ti-6Al-4V titanium alloy. *International Journal of Advanced Manufacturing Technology*, vol. 52, no. 9, p. 887-895, DOI:10.1007/s00170-010-2789-x.
- [7] Bäker, M., Rösler, J., Siemers, C. (2002). A finite element model of high speed metal cutting with adiabatic shearing. *Computers and Structures*, vol. 80, no. 5-6, p. 495-513, DOI:10.1016/S0045-7949(02)00023-8.
- [8] Wang, B., Liu, Z. (2015). Shear localization sensitivity analysis for Johnson-Cook constitutive parameters on serrated chips in high speed machining of Ti6Al4V. *Simulation Modelling Practice and Theory*, vol. 55, p. 63-76, DOI:10.1016/j.simpat.2015.03.011.
- [9] Strenkowski, J.S., Carroll, J.T. (1985). A finite element model of orthogonal metal cutting. *Journal of Engineering for Industry*, vol. 107, no. 4, p. 347-354, DOI:10.1115/1.3186008.
- [10] Mamalis, A.G., Horváth, M., Branis, A.S., Manolakos, D.E. (2001). Finite element simulation of chip formation in orthogonal metal cutting. *Journal of Materials Processing Technology*, vol. 110, p. 19-27, DOI:10.1016/S0924-0136(00)00861-X.
- [11] Huang, J.M., Black, J.T. (1996). An Evaluation of chip separation criteria for the FEM simulation of machining. *Journal of Manufacturing Science and Engineering*, vol. 188, no. 4, p. 545-554, DOI:10.1115/1.2831066.
- [12] Bil, H., Kılıç, S.E., Tekkaya, A.E. (2004). A comparison of orthogonal cutting data from experiments with three different finite element models. *International Journal of Machine Tools and Manufacture*, vol. 44, no. 9, p. 933-944, DOI:10.1016/j.ijmachtools.2004.01.016.
- [13] Shet, C., Deng, X. (2000). Finite element analysis of the orthogonal metal cutting process. *Journal of Materials Processing Technology*, vol. 105, no. 1-2, p. 95-109, DOI:10.1016/S0924-0136(00)00595-1.
- [14] Movahhedy, M.R., Gadala, M.S., Altintas, Y. (2000). Simulation of chip formation in orthogonal metal cutting process: An ALE finite element approach. *Machining Science and Technology*, vol. 4, no. 1, p. 15-42, DOI:10.1080/10940340008945698.
- [15] Özel, T., Zeren, E. (2007). Finite element modelling the influence of edge roundness on the stress and temperature fields induced by high speed machining. *International Journal of Advanced Manufacturing Technology*, vol. 35, no. 3, p. 255-267, DOI:10.1007/s00170-006-0720-2.
- [16] ABAQUS/CAE User's Manual, Version 6.8, (2009). Simulia, Providence.
- [17] Ambati, R., Yuan, H. (2010). FEM mesh-dependence in cutting process simulation. *International Journal of Advanced Manufacturing Technology*, vol. 53, no. 1, p. 313-323, DOI:10.1007/s00170-010-2818-9.
- [18] Mabrouki, T., Girardin, F., Asad, M., Rigal, J.F. (2008). Numerical and experimental study of dry cutting for an aeronautic aluminium alloy (A2024-T351). *International Journal of Machine Tools and Manufacture*, vol. 48, no. 11, p. 1187-1197, DOI:10.1016/j.ijmachtools.2008.03.013.
- [19] Ijaz, H., Zain-ul-abdein, M., Saleem, W., Asad, M., Mabrouki, T. (2016). A numerical approach on parametric sensitivity analysis for an aeronautic aluminium alloy turning process. *Mechanika*, vol. 22, no. 2, p. 149-155, DOI:10.5755/j01.mech.22.2.12825.
- [20] Chen, G., Li, J., He, Y., Ren, C. (2014). A new approach to the determination of plastic flow stress and failure initiation strain for aluminum alloys cutting process. *Computational Materials Science*, vol. 95, p. 568-578, DOI:10.1016/j.commatsci.2014.08.029.
- [21] Zhang, Y.C., Mabrouki, T., Nélías, D., Gong, Y.D. (2011). Chip formation in orthogonal cutting considering interface limiting shear stress and damage evolution based on fracture energy approach. *Finite Elements in Analysis and Design*, vol. 47, no. 7, p. 850-863, DOI:10.1016/j.finel.2011.02.016.
- [22] Johnson, G.R., Cook, W.H. (1983). A constitutive model and data for metals subjected to large strains, high strain rates and high temperatures. *Proceeding of the 7th International Symposium on Ballistics*, Hague, p. 541-547.
- [23] Johnson, G.R., Cook, W.H. (1985). Fracture characteristics of three metals subjected to the various strains, strain rates, temperatures and pressures. *Engineering Fracture Mechanics*, vol. 21, no. 1, p. 31-48, DOI:10.1016/0013-7944(85)90052-9.
- [24] Teng, X., Wierzbicki, T. (2006). Evaluation of six fracture models in high velocity perforation. *Engineering Fracture Mechanics*, vol. 73, no. 12, p. 1653-1678, DOI:10.1016/j.engfracmech.2006.01.009.
- [25] Öpöz, T. T., Chen, X. (2012). Influential parameters in determination of chip shape in high speed machining. *Key Engineering Materials*, vol. 496, p. 211-216, DOI:10.4028/www.scientific.net/KEM.496.211.
- [26] Hillerborg, A., Modéer, M., Peterson, P.E. (1976). Analysis of crack formation and crack growth in concrete by means of fracture mechanics and finite elements. *Cement and Concrete*

- Research, vol. 6, no. 6, p. 773-781, DOI:10.1016/0008-8846(76)90007-7.
- [27] He, M., Li, F. (2010). Modified transformation formulae between fracture toughness and CTOD of ductile metals considering pre-deformation effects. *Engineering Fracture Mechanics*, vol. 77, no. 14, p. 2763-2771, DOI:10.1016/j.engfracmech.2010.06.021.
- [28] Garrison, Jr W.M., Moody, N.R. (1987). Ductile fracture. *Journal of Physics and Chemistry of Solids*, vol. 48, no. 11, p. 1035-1047, DOI:10.1016/0022-3697(87)90118-1.
- [29] Sisto, T.S.D., Carr, F.L., Larson, F.R. (1964). *The influence of section size on the mechanical properties and fracture toughness of 7075-T6 aluminum, 6Al-6V-2Sn titanium, and AISI 4340 steel*. Material testing laboratory U.S. Army Materials Research Agency Watertown, Massachusetts.
- [30] Belhadi, S., Mabrouki, T., Rigal, J-F., Boulanouar, L. (2005). Experimental and numerical study of chip formation during straight turning of hardened AISI 4340 steel. *Proceedings of the Institution of Mechanical Engineers, Part B: Journal of Engineering Manufacture*, vol. 219, no. 7, p. 515-524, DOI:10.1243/095440505X32445.
- [31] Haddag, B., Atlati, S., Nouari, M., Barlier, C., Zenasni, M. (2012). Analysis of the Cutting Parameters Influence During Machining Aluminium Alloy A2024-T351 with Uncoated Carbide Inserts. *Engineering Transactions*, vol. 60, no. 1, p. 31-39.
- [32] Wang, B., Liu, Z. (2015). Shear localization sensitivity analysis for Johnson-Cook constitutive parameters on serrated chips in high speed machining of Ti6Al4V. *Simulation Modelling Practice and Theory*, vol. 55, p. 63-76, DOI:10.1016/j.simpat.2015.03.011.

Local Corner Smoothing Transition Algorithm Based on Double Cubic NURBS for Five-axis Linear Tool Path

Liqiang Zhang^{1,*} – Kai Zhang¹ – Yecui Yan²

¹ Shanghai University of Engineering Science, College of Mechanical Engineering, China

² Shanghai University of Engineering Science, Automotive Engineering College, China

A five-axis tool path is often composed of a linear path that has a tangential discontinuity so that the tangential velocity will be abrupt or be equal to zero at the corner of the adjacent segments. Therefore, it greatly affects the machining efficiency and quality. Thus, a corner smoothing transition algorithm based on double cubic NURBS, which is curvature-continuous and satisfies the given accuracy constraint, is proposed to smooth the local corner at the adjacent five-axis linear path. On the basis of the smoothing transition model, the parametric synchronization between the smoothed double NURBS trajectories and the remaining two linear segments are respectively constructed to realize the smoothing variation along the tool tip translational trajectory and tool axis rotational trajectory. The simulation and examples show that the proposed transition algorithm can satisfy the error constraints, reduce the feedrate fluctuation, and improve the machining quality.

Keywords: five-axis machining, corner transition, double NURBS curves, tool path

Highlights

- A corner smoothing transition algorithm based on double cubic NURBS is proposed to smooth the five-axis linear tool path.
- The proposed algorithm is curvature-continuous and satisfies the given accuracy constraint.
- The approximation error has an analytical relationship with the transition length of the smoothed curve.
- The synchronization method can guarantee tool-tip translation and tool axis rotation with continuous and smooth variation.
- The proposed method has been validated with simulations and experimental results.

0 INTRODUCTION

Five-axis numerical control (NC) machining has become an important technique for high-efficient machining of the complex surface parts [1]. Compared with traditional three-axis NC machining, five-axis NC machining can significantly improve the tool accessibility by changing the tool orientation and possess the superiority in high speed and precision machining [2]. However, one main factor affecting the five-axis high speed and precision machining is the smoothing problem of the tool path. Most of the CAM software use a series of linear segments to approximate the complex surface to generate a five-axis tool path, which is composed of many discrete tool positions [3]. Thus, the five-axis tool path is a linear segment and will result in the tangency and curvature discontinuity that appear at the junction of adjacent segments. During the machining process, the tangential velocity will be a mutation or be equal to zero at the corner of the adjacent segments so that it greatly affects the machining efficiency and machining quality [4] and [5]. Therefore, geometrical smoothing of the linear tool path must be achieved first to guarantee smooth motion and avoid frequent acceleration/deceleration. Once the linear tool path is smoothed, feedrate planning can be performed using the jerk continuous planning method to produce a

smooth cutting movement along the tool path [6]. As a result, cutting efficiency and machining quality will be improved significantly.

In recent years, with much deeper research on the parametric curves, such as Bezier, B-Spline and non-uniform rational basis spline (NURBS), the tool path of parametric curves has been widely used to describe smooth trajectories and realize tangential continuities [7] to [9]. Thus, there are two kinds of ways available in the literature to smooth the linear tool path by utilizing these smooth parametric curves: global smoothing and local smoothing [10], as shown in Fig. 1.

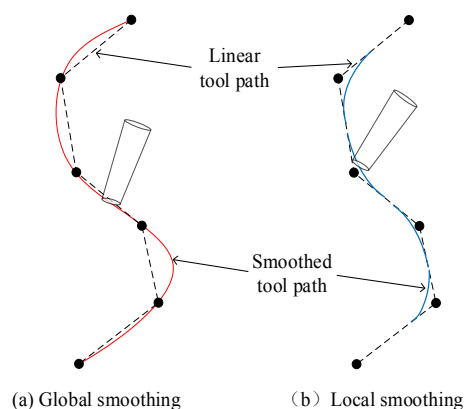


Fig. 1. Linear toolpath smoothing

*Corr. Author's Address: Shanghai University of Engineering Science, Shanghai, China, zhangzliq@gmail.com

Global smoothing means that the discrete tool points are approximated or interpolated by using one parametric curve to generate the smooth toolpath with G1 and above continuity. Langeron et al. [11] proposed a new method to generate the five-axis tool path by double NURBS, which described the trajectories of the tool tip points and the tool axis points, respectively. Li et al. [12] extended the three-axis NURBS codes format to five-axis machining by the double NURBS interpolation method to smooth the linear five-axis tool path. Bi et al. [13] presented compact dual-NURBS tool paths with isometric distance algorithm to smooth the linear five-axis tool paths and used the quaternion to realize the spatial motion of the tool. All the above methods are performed in a work coordinate system (WCS), and some smoothing algorithm are also realized in a machine coordinate system (MCS) [14] and [15]. Li et al. [16] proposed a linear five-axis toolpath smoothing algorithm based on double NURBS in MCS.

The local smoothing means that a smooth curve satisfying the predefined error constraint was inserted at the corner of two adjacent linear segments to realize the smoothness and continuity of the linear tool path. In recent years, more and more methods have been developed for three-axis corner smoothing [17] to [19]. However, because it is difficult to realize the smoothing of the tool orientation for five-axis tool paths, there have been only a few studies and further effort should be made on this subject. Buedaert et al. [5] presented a five-axis corner rounding method to smooth the tool path satisfying the acceleration and jerk limit. Two B-Spline curves were inserted at the corner of the tool path to smooth the tool tip trajectory and the tool orientation, respectively. Shi et al. [20] proposed a smoothing method to round the corners of the five-axis tool paths with a pair of quintic PH curves, in which one curve rounded the corner of the tool-tip trajectory and the other curve rounded the corner of the trajectory of the tool axis. Tulsyan et al. [10] proposed a new approach to achieving the smoothing corner by inserting quintic and septic splines for the tool tip points and tool orientations at the adjacent linear five-axis tool path, respectively.

However, the overcuts on the parts caused by the tool orientation adjustment are not strictly restricted. Thus, it remains a challenge for a five-axis NC system to maintain the requirements of machining accuracy and smoothness of the tool motion trajectory simultaneously.

In this paper, a pair of double cubic NURBS curves satisfying the predefined fitting accuracy are used to fair the corners of the adjacent five-axis linear

segments and generate the smooth toolpath with G2 continuity in WCS. The rest of this paper is organized as follows: Section 1 proposes the five-axis corner smoothing transition algorithm based on double cubic NURBS curves in WCS. Section 2 performs the synchronization of the smoothed five-axis paths. In Section 3, computational example and experiment are adopted to evaluate the validity and effectiveness of the proposed algorithm. Finally, Section 4 is the conclusion of this paper.

1 CORNER SMOOTHING TRANSITION

1.1 Local Corner Smoothing by Double Cubic NURBS Curves with G2 Continuity

The discrete tool location data in WCS, which can be acquired from the CAM module in five-axis NC machining, consists of a series of tool tip points $\{A_i = (x_{ai}, y_{ai}, z_{ai}), i = 1, \dots, m\}$ and a series of tool axis vectors $\{O_i = (o_{xi}, o_{yi}, o_{zi})\}$. Therefore, the five-axis linear tool path in WCS can be described by two linear trajectories. One represents the translational linear trajectory which is defined by a sequence of tool tip points A_i and another represents the rotational linear trajectory defined by a sequence of tool axis points (which are the second points on the tool axis) $\{B_i = (x_{bi}, y_{bi}, z_{bi})\}$, as shown in Fig. 2. The tool axis vector O_i can be computed by the pair of tool tip point and tool axis point (A_i, B_i) . Thus, the tool tip point, tool axis point, and tool axis vector satisfy the following relations:

$$B_i = A_i + H \cdot O_i \tag{1}$$

$$O_i = \frac{B_i - A_i}{\|B_i - A_i\|}, \tag{2}$$

where H is the distance between the tool tip point and tool axis point.

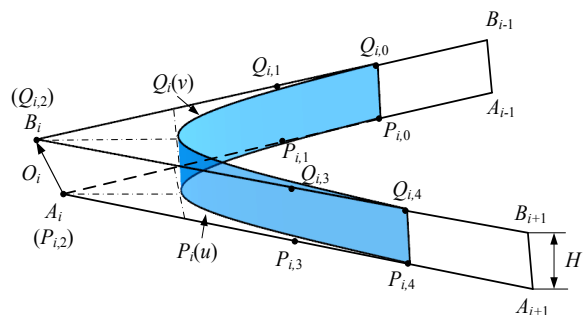


Fig. 2. Five-axis linear tool path and corner transition curves

The term “curvature-continuous” (also called as “G2 continuous”) means that two curves share

the same curvature centre at the junction. The path with G^2 continuity can guarantee the continuities of tangency and curvature so that the fluctuation in feed, acceleration and jerk can be improved greatly. Meanwhile, the minimum degree of the NURBS curve satisfying the G^2 continuity is cubic. Thus, double cubic NURBS curves are utilized to fair the corner of the adjacent five-axis linear segments and generate the smooth toolpath with G^2 continuity. The smooth transition cubic NURBS pair, which are constrained with five control points, are respectively given as [21]:

$$\begin{cases} P_i(u) = \frac{\sum_{j=0}^4 N_{j,3}(u) w_{i,j} P_{i,j}}{\sum_{j=0}^4 N_{j,3}(u) w_{i,j}}, & u \in [0,1] \\ Q_i(v) = \frac{\sum_{j=0}^4 N_{j,3}(v) w_{i,j} Q_{i,j}}{\sum_{j=0}^4 N_{j,3}(v) w_{i,j}}, & v \in [0,1] \end{cases}, \quad (3)$$

where $N_{j,3}(u)$ are the 3rd degree B-spline basis functions defined on the knot vector $U = \{0, 0, 0, 0, 0.5, 1, 1, 1, 1\}$ and can be computed as:

$$\begin{cases} N_{j,3}(u) = \frac{u-u_j}{u_{j+3}-u_j} N_{j,2}(u) + \frac{u_{j+4}-u}{u_{j+4}-u_{j+1}} N_{j+1,2}(u) \\ N_{j,0}(u) = \begin{cases} 1, & \text{if } u_j \leq u < u_{j+1} \\ 0, & \text{else} \end{cases} \end{cases}. \quad (4)$$

1.2 Corner Smoothing of the Linear Trajectory of Tool Tip Points

Corner smoothing in three-axis linear segments can be regarded as the foundation of the corner smoothing in the five-axis tool path. One cubic NURBS curve is utilized to fair the corner of the translational path, and another cubic NURBS curve is used to smooth the corner of the rotational path. Thus, by inserting the double cubic NURBS curves to fair the translational and rotational paths, the corner of the five-axis linear tool path can be smoothed. Therefore, in this section, take the translational trajectory of the tool tip points as an example, the NURBS corner smoothing transition model satisfying the error constraint and G^2 continuity will be constructed.

1.2.1 Construction of the Corner Smoothing Transition Model

As shown in Fig. 3, the corner is formed by two adjacent segments of the translation trajectory $A_{i-1}A_i$

and A_iA_{i+1} . The unit vectors of the two adjacent segments are $E_{i,1}$ and $E_{i+1,1}$, respectively, and the angle of the two unit vectors is $\alpha_i \in [0, \pi]$.

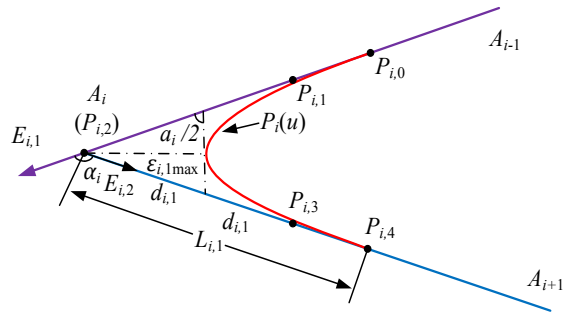


Fig. 3. The corner smoothing model with NURBS transition

Then the corner is rounded by a cubic NURBS curve satisfying the error constraint and G^2 continuity. $P_{i,0}, P_{i,1}, P_{i,2}, P_{i,3}$ and $P_{i,4}$ are five control points of the NURBS curve, and the weights are $w_{i,0}=w_{i,4}, w_{i,1}=w_{i,3}$ and $w_{i,2}$, and the knot vector is $U = \{0, 0, 0, 0, 0.5, 1, 1, 1, 1\}$. Meanwhile, point $P_{i,2}$ coincides with point A_i so that it is convenient to fix the NURBS curve. In addition, the points $P_{i,0}, P_{i,1}$ and $P_{i,3}, P_{i,4}$ symmetrically located in linear segments $A_{i-1}A_i$ and A_iA_{i+1} , and satisfy the following relations:

$$L_{i,1} = |P_{i,0}A_i| = |A_iP_{i,4}|, \quad (5)$$

$$2d_{i,1} = |P_{i,1}A_i| = |A_iP_{i,3}|, \quad (6)$$

where $L_{i,1}$ presents the transition length of the NURBS curve. According to [5], the relationship between $L_{i,1}$ and $d_{i,1}$ satisfy that $L_{i,1}/2d_{i,1} = |P_{i,0}A_i|/|P_{i,1}A_i| \in [1.4, 1.75]$. Sets the ratio $L_{i,1}/2d_{i,1} = 1.5$, then Eqs. (5) and (6) can be reformulated as:

$$L_{i,1} = 1.5 |P_{i,1}A_i| = 1.5 |A_iP_{i,3}| = 3d_{i,1}, \quad (7)$$

$$|P_{i,1}A_i| = |A_iP_{i,3}| = 2L_{i,1}/3. \quad (8)$$

when the tool tip points and the transition lengths are acquired, the five control points of the cubic NURBS curve can be located as:

$$\begin{cases} P_{i,0} = A_i - L_{i,1}E_{i,1} \\ P_{i,1} = A_i - \frac{2}{3}L_{i,1}E_{i,1} \\ P_{i,2} = A_i \\ P_{i,3} = A_i + \frac{2}{3}L_{i,1}E_{i+1,1} \\ P_{i,4} = A_i + L_{i,1}E_{i+1,1} \end{cases}, \quad (9)$$

where the transition length $L_{i,1}$ must be limited by the predefined approximation error ε , and it can be obtained using the analytical relationship between the transition length and the approximation error shown in the next section.

1.2.2 Estimation Error of the Smoothed Curve

As shown in Fig. 3, the inconsistency of the machining path between the newly inserted transition curve and the original linear segments will cause the approximation error. Therefore, the inserted NURBS path must satisfy the constraint of the approximation error.

Because the curve $P_i(u)$ is symmetrical with the angular bisector of the angle $\angle A_{i-1}A_iA_{i+1}$, the maximal error between the transition curve and two linear segments is the distance between the midpoint of the curve $P_i(u)$ at $u=0.5$ and the point A_i , that is $|P_i(0.5)A_i|$. Suppose that the approximation error, the maximal approximation error, and the predefined approximation error are $\varepsilon_{i,1}$, $\varepsilon_{i,1max}$ and ε , respectively. If $\varepsilon_{i,1max} \leq \varepsilon$, then the approximation error between the transition curve and the adjacent segments can be limited.

The approximation error of the transition NURBS curve must satisfy the following condition:

$$\varepsilon_{i,1} \leq \varepsilon_{i,1max} = \frac{2w_{i,1}L_{i,1} \sin(\alpha_i / 2)}{3(w_{i,1} + w_{i,2})} \leq \varepsilon. \quad (10)$$

1.2.3 Analytical Relationship between the Transition Length and the Approximation Error

According to Eq. (10), the transition length $L_{i,1}$ must satisfy the restraint of the predefined approximation error ε , so the transition length $L_{i,1}$ can be expressed as:

$$L_{i,1} = \frac{3(w_{i,1} + w_{i,2})\varepsilon_{i,1max}}{3w_{i,1} \sin(\alpha_i / 2)} \leq \frac{3(w_{i,1} + w_{i,2})\varepsilon}{2w_{i,1} \sin(\alpha_i / 2)}, \quad (11)$$

when $\varepsilon_{i,1max} = \varepsilon$, the transition length $L_{i,1}$ has the maximum value, and it can be written as:

$$L_{i,1} = \frac{3(w_{i,1} + w_{i,2})\varepsilon}{2w_{i,1} \sin(\alpha_i / 2)}. \quad (12)$$

Meanwhile, the sum of the transition lengths at the adjacent segments must not exceed the length of linear segment they lie in, that means:

$$\begin{cases} L_{i-1,1} + L_{i,1} \leq |A_{i-1}A_i| \\ L_{i,1} + L_{i+1,1} \leq |A_iA_{i+1}| \end{cases} \quad (13)$$

It can be concluded that $L_{i,1}$ satisfy the following constraint:

$$L_{i,1} \leq \min(0.5|A_{i-1}A_i|, 0.5|A_iA_{i+1}|) \quad (14)$$

The transition length $L_{i,1}$ can be obtained as:

$$L_{i,1} \leq \min\left(0.5|A_{i-1}A_i|, 0.5|A_iA_{i+1}|, \frac{3(w_{i,1} + w_{i,2})\varepsilon_{i,1max}}{2w_{i,1} \sin(\alpha_i / 2)}\right). \quad (15)$$

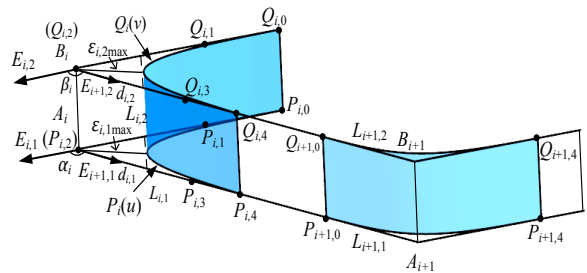


Fig. 4. Five-axis corner transition model based on double cubic NURBS with G² continuity

1.3 Generation of Five-Axis Corner Smoothing Model with G² Continuity

Similarly to the generation of the corner smoothing transition model of the translation paths, the corner smoothing transition model of the tool axis points can also be constructed. Thus, by using a series of double cubic NURBS curves $P_i(u)$ and $Q_i(v)$, the corners in five-axis linear paths can be smoothed with G² continuity, as shown in Fig. 4. The NURBS curve $P_i(u)$ is used to smooth the corner $\angle A_{i-1}A_iA_{i+1}$, and the maximal tool tip approximation error between the smoothed curve and the original linear segments is $\varepsilon_{i,1max}$. The NURBS curve $Q_i(v)$ is utilized to fair the corner $\angle B_{i-1}B_iB_{i+1}$, and the maximum tool axis approximation error is $\varepsilon_{i,2max}$. If both the maximal approximation errors $\varepsilon_{i,1max}$ and $\varepsilon_{i,2max}$ are constrained under the predefined approximation error ε as Eq. (16), then the transition lengths can be obtained.

$$\max(\varepsilon_{i,1max}, \varepsilon_{i,2max}) \leq \varepsilon. \quad (16)$$

Next, it is necessary to determine the maximal approximation errors $\varepsilon_{i,1max}$ and $\varepsilon_{i,2max}$. In this paper, the distance between the tool tip point and the reference tool axis point is constant with H . Taking the original tool location $(P_{i,0}, Q_{i,0})$ as an example, the distance between points $P_{i,0}$ and $Q_{i,0}$ must satisfy the following equation:

$$|Q_{i,0} - P_{i,0}| = H. \quad (17)$$

Left of the above equation can be computed as:

$$\begin{aligned}
 |Q_{i,0} - P_{i,0}| &= |(B_i - L_{i,2}E_{i,2}) - (A_i - L_{i,1}E_{i,1})| = \\
 &= |(B_i - A_i) + L_{i,1}E_{i,1} - L_{i,2}E_{i,2}| = \\
 &= \left| H \cdot O_i + \frac{3\varepsilon_{i,1\max} E_{i,1}}{\sin(\alpha_i/2)} - \frac{3\varepsilon_{i,2\max} E_{i,2}}{\sin(\beta_i/2)} \right| \geq \\
 &\geq H + \frac{3\varepsilon_{i,1\max}}{\sin(\alpha_i/2)} - \frac{3\varepsilon_{i,2\max}}{\sin(\beta_i/2)}. \tag{18}
 \end{aligned}$$

If Eq. (17) is tenable, the right part of Eq. (18) must only exist H , so we can conclude that:

$$\frac{3\varepsilon_{i,1\max}}{\sin(\alpha_i/2)} - \frac{3\varepsilon_{i,2\max}}{\sin(\beta_i/2)} = 0.$$

The above formula can be calculated as:

$$\frac{3\varepsilon_{i,1\max}}{3\varepsilon_{i,2\max}} = \frac{\sin(\alpha_i/2)}{\sin(\beta_i/2)}. \tag{19}$$

Hence, according to Eqs. (16) and (19), the approximation errors $\varepsilon_{i,1\max}$ and $\varepsilon_{i,2\max}$ can be determined. Then the transition lengths can be computed based on Eq. (15). Moreover, taking the transition lengths into Eq. (9), all the control points of the transition NURBS curves are given. Finally, the smoothed double cubic NURBS curves for translation paths and rotation trajectories can be written based on Eq. (3).

2 SYNCHRONIZATION OF THE SMOOTHED FIVE AXIS PATHS

After inserting a sequence of double cubic NURBS curves at the adjacent segments, the smooth five-axis tool paths with G^2 continuity can be generated. However, in five-axis tool path interpolation, both the tool-tip translation and the tool axis rotation must be guaranteed with continuous and smooth variation, so it is a key point to realize synchronous movement between the translational trajectory of tool-tip points and the rotational trajectory of tool axis points.

2.1 Parametric Synchronization of the Double Cubic NURBS Curves

By analysing the interpolation process along the double NURBS trajectories, the synchronous movement can be regarded as the synchronous relationship between the parameter u and v . That is, if there is parameter $u \in [u_n, u_{n+1}]$, there must be a parameter v with $v \in [v_n, v_{n+1}]$. In addition, the distances between the tool tip trajectory $P_i(u)$ and the

corresponding tool axis trajectory $Q_i(v)$ always keep a fixed value H .

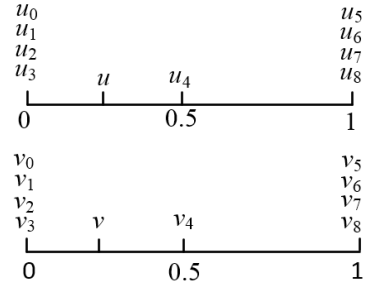


Fig. 5. Parametric synchronization between the double NURBS curves

Fig. 5 shows the parametric synchronization between the double NURBS paths. If there is parameter $u \in [u_n, u_{n+1}]$, there must be a parameter v with $v \in [v_n, v_{n+1}]$, where $n=3, 4$, and they satisfy the following equation:

$$|Q_i(v) - P_i(u)| = H. \tag{20}$$

Supposing the parameter u of the NURBS curve $P_i(u)$ is known, then Eq. (20) is translated into Eq. (21) which is solved in a given interval.

$$\varphi(v) = |Q_i(v) - P_i(u)|^2 - H^2 = 0. \tag{21}$$

Solving Eq. (21), the parameter v of the NURBS curve $Q_i(v)$ corresponding to u can be obtained. Then according to the relation of u and v , the tool vector corresponding to the tool-tip point can be expressed as:

$$\vec{O}_i = \frac{Q_i(v) - P_i(u)}{|Q_i(v) - P_i(u)|}. \tag{22}$$

Thus, the tool positions in the five-axis corner paths interpolation are known. In addition, the continuous and smooth variation of the rotational trajectory is proved by using the first-order geometrical derivative of the tool vector with respect to the displacement s of the tool tip trajectory. A detailed presentation had been proposed in [22], so parameter u and displacement s is linked by a C^3 continuous ninth-order spline, which is written as $u=f(s)$. According to Eq. (21), the relation between u and v is simply written as $v=g(u)$. Then there is:

$$\begin{aligned}
 \frac{d\vec{O}_i}{ds} &= \frac{d\vec{O}_i}{du} \cdot \frac{du}{ds} = \frac{d \frac{Q_i g(u) - P_i(u)}{|Q_i g(u) - P_i(u)|}}{du} \Big/ f'(s) = \\
 &= \frac{Q_i' g(u) g'(u) - P_i'(u)}{|Q_i g(u) - P_i(u)|} \Big/ f'(s). \tag{23}
 \end{aligned}$$

It can be concluded from the above equation that the rotational motion of the tool axis is continuous and smooth. Meanwhile, the tool tip point and the corresponding tool vector can be obtained.

2.2 Synchronization of the Remained Linear Tool Paths

The remaining five-axis path is the linear path between the tool positions $(P_{i,4}, Q_{i,4})$ and $(P_{i+1,0}, Q_{i+1,0})$ in WCS. Therefore, the synchronization interpolation of five-axis linear paths can be achieved by constructing the parametric synchronization method between the translational trajectory and the rotational trajectory, which can be defined as:

$$\frac{|A_{i,n} - P_{i,4}|}{|P_{i+1,0} - P_{i,4}|} = \frac{\theta_{i,n}}{\theta_i} = x_{i,n} \tag{24}$$

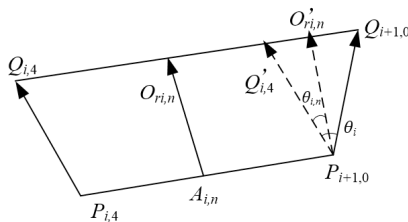


Fig. 6. Synchronization of the linear tool path

As shown in Fig. 6, $P_{i,4}$ and $P_{i+1,0}$ are the control points on the translational path, $Q_{i,4}$ and $Q_{i+1,0}$ are the control points on the rotational path; both of them are obtained by using the method in Section 2.2. Setting $A_{i,n}$ is any point on the translational path $P_{i,4}P_{i+1,0}$, and it can be computed as:

$$A_{i,n} = (1 - t_n) P_{i,4} + t_n P_{i+1,0}, \quad t_n \in [0, 1]. \tag{25}$$

θ_i is the angle between the start vector $\overrightarrow{P_{i,4}Q_{i,4}}$ and the end vector $\overrightarrow{P_{i+1,0}Q_{i+1,0}}$, which is expressed as:

$$\theta_i = \arccos \left(\frac{\overrightarrow{P_{i,4}Q_{i,4}} \cdot \overrightarrow{P_{i+1,0}Q_{i+1,0}}}{\left| \overrightarrow{P_{i,4}Q_{i,4}} \right| \left| \overrightarrow{P_{i+1,0}Q_{i+1,0}} \right|} \right), \tag{26}$$

where $\theta_{i,n}$ is the angle between the start vector $\overrightarrow{P_{i,4}Q_{i,4}}$ and the vector at any position of the path $P_{i,4}P_{i+1,0}$ and it can be obtained by Eqs. (24) to (26).

Next, the unit vector $\overrightarrow{O_{ri,n}}$ at any position of the path $P_{i,4}P_{i+1,0}$ can be obtained according to the rotation formula in [23]:

$$\begin{aligned} \overrightarrow{O_{ri,n}} = & \overrightarrow{P_{i,4}Q_{i,4}} \cos \theta_{i,n} / \left| \overrightarrow{P_{i,4}Q_{i,4}} \right| + \\ & + \left(\overrightarrow{O_{i,4}} \cdot \overrightarrow{E_{i,1}} \right) \cdot \overrightarrow{E_{i,1}} \cdot \left(1 - \cos \theta_{i,n} \right) + \left(\overrightarrow{O_{i,4}} \cdot \overrightarrow{E_{i,1}} \right) \sin \theta_{i,n}, \end{aligned} \tag{27}$$

in which $\overrightarrow{O_{i,4}}$ is the unit vector of the tool vector $\overrightarrow{P_{i,4}Q_{i,4}}$ and can be calculated as:

$$\overrightarrow{O_{i,4}} = \frac{Q_{i,4} - P_{i,4}}{\left| Q_{i,4} - P_{i,4} \right|}. \tag{28}$$

Thus, by utilizing the method in Sections 1.2.1 and 1.2.2, the tool tip points and the corresponding tool vector in five-axis interpolation are obtained, and the parametric synchronization interpolation between the remained two linear paths and the double NURBS paths are constructed to achieve continuous and smooth variation along the translational trajectory and rotational trajectory.

3 COMPUTATIONAL EXAMPLE AND EXPERIMENT VALIDATION

In this section, the proposed local corner smoothing transition algorithm based on double cubic NURBS is utilized to fair the corners for five-axis linear tool paths. Two examples are adopted to evaluate the validity and effectiveness of the proposed algorithm.

3.1 Example 1

In this experiment, a flank-milling simulation for an impeller is used to generate the linear five-axis path formed by discrete tool data in WCS, as shown in Fig. 7. For the convenience of description, four tool positions are chosen to describe the proposed corner smoothing transition algorithm. Each of the tool positions consists of the tool-tip point A_i , and the tool axis point B_i , and their coordinates are shown in Table 1.

The linear five-axis path of the four tool positions in WCS is generated by MATLAB, as shown in Fig. 8. Then, the proposed local corner smoothing transition algorithm is used to smooth the corners of linear tool paths, as shown in Fig. 9.

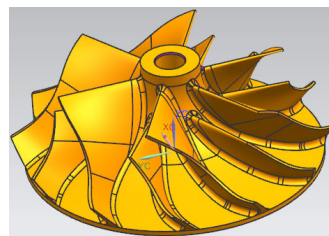


Fig. 7. Flank milling for an impeller part

It is known from Eqs. (10) and (15) that the approximation errors of the smoothed curves are affected by the transition lengths. While the transition

lengths are mainly limited by the predefined approximation error and the half length of the adjacent segments. Thus, setting two groups fitting precision to smooth the corners of the linear path, as shown in Table 2, and the results show that the proposed corner-smoothing algorithm can be used to generate the double NURBS path satisfying the given precision error.

Table 1. The tool positions in WCS

No.	Tool-tip points A_i [mm]	Tool axis points B_i [mm]
1	(174.1311,-6.4621,-68.1138)	(174.2154,-7.4301,-58.1611)
2	(176.0862,-6.8579,-68.1299)	(176.2593,-7.9576,-58.1921)
3	(178.2366,-8.4623,-68.2326)	(178.4059,-9.7816,-58.3215)
4	(179.5084,-11.8775,-68.4966)	(179.5424,-13.4244,-58.6170)

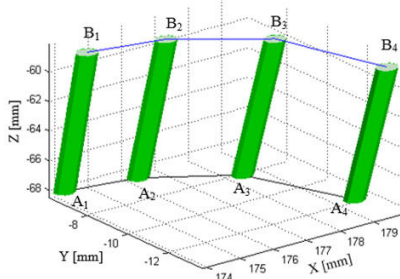


Fig. 8. The five-axis linear tool path in WCS

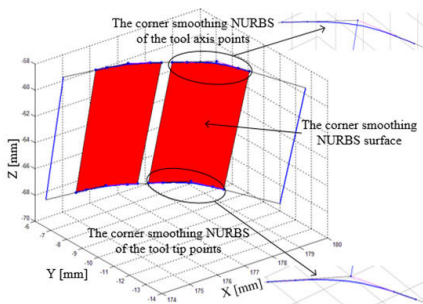


Fig. 9. Five-axis corners smoothing based on double NURBS curve

Table 2. The double NURBS smoothing results under two fitting precision restriction

No.	The approximation error for tool position (A_2, B_2)		The approximation error for tool position (A_3, B_3)	
	Tool tip curve [mm]	Tool axis curve [mm]	Tool tip curve [mm]	Tool axis curve [mm]
1	0.0729	0.078	0.078	0.0768
2	0.0729	0.079	0.1265	0.1307

The first group result shows the maximal approximation errors for tool positions (A_2, B_2)

and (A_3, B_3) under the constraint of the predefined approximation error as 0.078 mm. From Table 2, both of the maximal approximation errors for tool positions (A_2, B_2) and (A_3, B_3) are 0.08 mm, which appears at the centre points of the tool axis curve $Q_2(v)$ and the tool tip curve $P_3(u)$. It can be concluded that the approximation errors are influenced by the predefined approximation error. Fig. 10 shows the error distribution along the double NURBS paths, and it can be seen the approximation errors for tool positions (A_2, B_2) and (A_3, B_3) are less than the predefined error restriction.

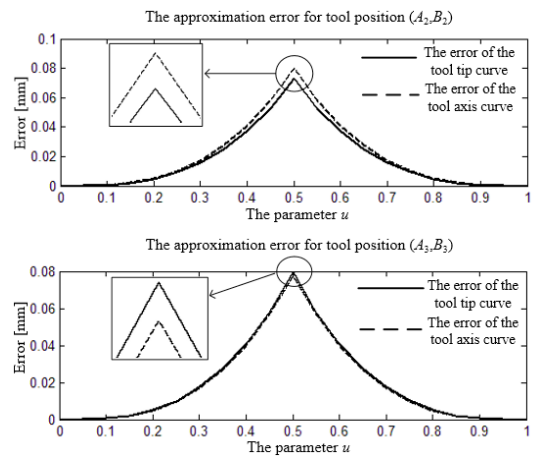


Fig. 10. The approximation error for tool positions (A_2, B_2) and (A_3, B_3) under No. 1 group fitting precision

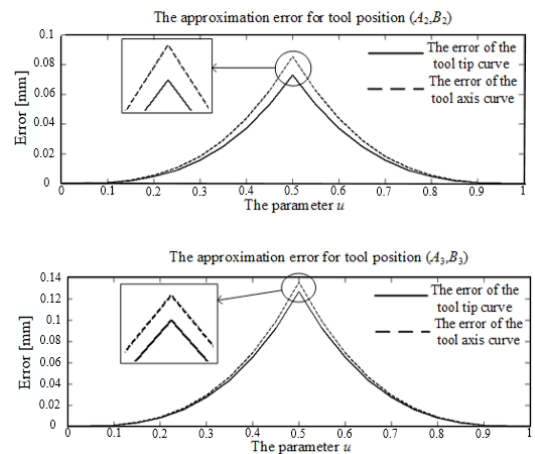


Fig. 11. The approximation error for tool positions and under No. 2 group fitting precision

Utilizing the proposed algorithm to smooth the tool positions (A_2, B_2) and (A_3, B_3) under the restriction of the predefined error as 0.15 mm, it can be seen from the second group results that the maximal approximation errors for tool positions

(A_2, B_2) and (A_3, B_3) are 0.079 mm and 0.1307 mm, which appears at the center points of the tool axis curve $Q_2(v)$ and $Q_3(v)$, respectively. Fig. 11 shows the error distribution along the double NURBS paths and all the approximation errors for tool positions (A_2, B_2) and (A_3, B_3) do not exceed the given precision.

3.2 Example 2

As shown in Fig. 12, to verify the availability of the proposed corner smoothing and synchronization transition algorithm, the flank milling of the impeller on the five-axis machine tool with dual-table is performed by comparing the proposed algorithm and the direct G^1 machining method, which do not use corner smoothing and still maintains the linear paths. It can be seen from Fig. 13 that the results show the proposed algorithm can smooth the linear tool path of blades to satisfy the given fitting accuracy and generate the double NURBS paths with G^2 continuity.

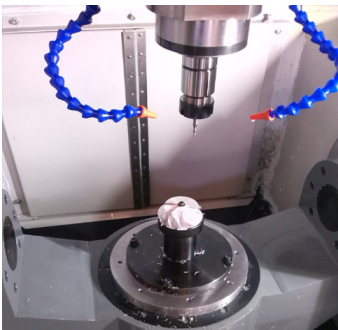


Fig. 12. The flank milling of an impeller

It can be seen from Fig. 13a that tool marks obviously appear on the blades by using the G^1 machining method. While the machined surfaces of the impeller using the proposed algorithm in Fig. 13b are smoother and possess better finished quality.

Both the proposed corner-smoothing algorithm and the direct G^1 method are implemented by setting the velocity as 1800 mm/min, the acceleration as 1000 mm/s², the jerk as 5000 mm/s³, and the interpolation period as 2 ms. The results of the velocity and acceleration curves are shown in Figs. 14 and 15, respectively. From the results, it can be seen that the proposed algorithm possesses higher velocity with less fluctuation. Compared with the direct G^1 block methods, the proposed algorithm only takes 12.074 s to machine one path of the impeller, while the direct G^1 method spends 14.780 s, so the machining time of the proposed algorithm is reduced by about 18.3%. It can be concluded that the proposed algorithm can possess a higher machining efficiency, and it can be

advantageous to improve the machining accuracy and surface quality.

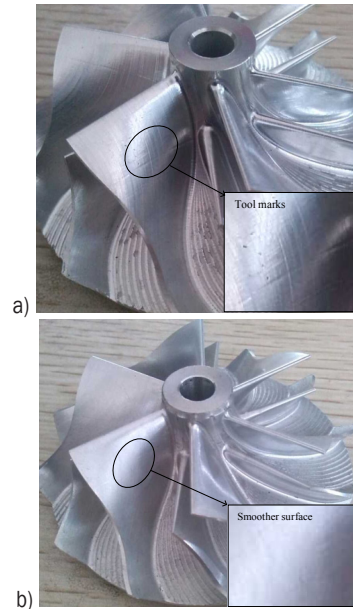


Fig. 13. Comparison of the impellers machining quality using two methods; a) the impeller machining quality in direct G^1 block machining method; and b) the impeller machining quality in proposed algorithm

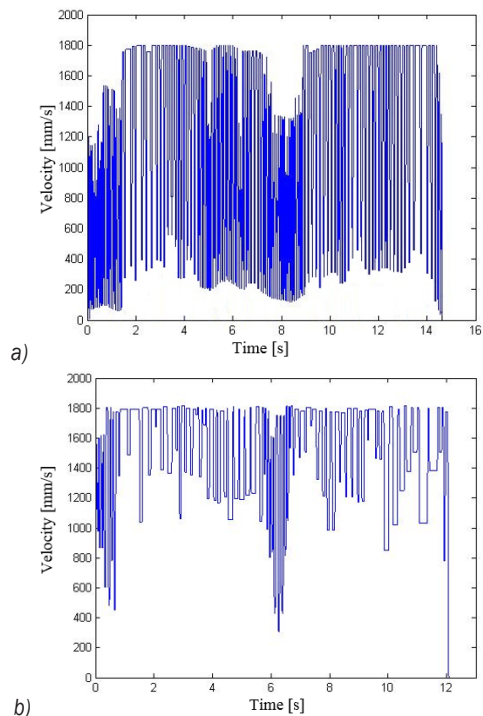


Fig. 14. Comparison of the velocity on flank milling of a blade; a) the velocity in proposed algorithm and b) the velocity in direct G^1 block-machining method

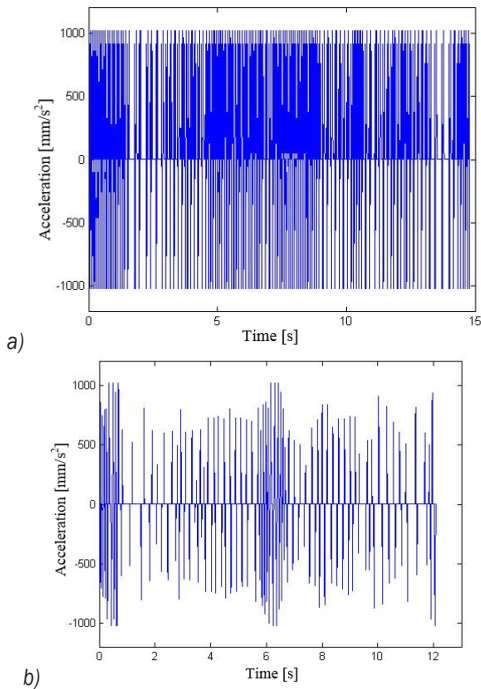


Fig. 15. Comparison of the acceleration on flank milling of a blade; a) the acceleration in direct G^1 block machining method, b) the acceleration in proposed algorithm

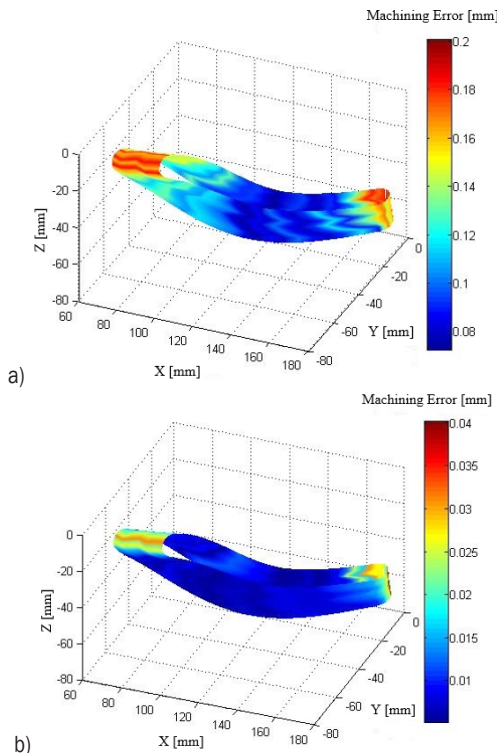


Fig. 16. Comparison of the error distribution on flank milling of a blade; a) the impeller machining quality in direct G^1 block machining method, and b) the impeller machining quality in proposed algorithm

To verify the availability and precision of the proposed algorithm, the machining errors on the flank milling of a blade are obtained by calculating the deviation of the machined surface. Both of the error results are achieved by setting the predefined error as 0.04 mm. Then, by using the Coordinate Measuring Machining (CMM), 70×7 points can be acquired from the machined blade to compare with the corresponding points of the surface. The error distributions of the machined surface for the two methods are shown in Fig. 16. It can be seen from Fig. 16b that the machining errors, by using the proposed methods, satisfy the predefined error 0.04 mm and most of the machining errors are less than 0.015 mm. However, most of the machining errors exceed the predefined error greatly in the conventional G^1 method. Thus, the comparison results show that the proposed corner smoothing algorithm possesses higher precision and can improve the machining surface quality significantly.

4 CONCLUSIONS

In this paper, a pair of double cubic NURBS curves satisfying the predefined fitting accuracy are utilized to fair the corners of the adjacent five-axis linear segments and generate the smooth toolpath with G^2 continuity in WCS.

The proposed algorithm has three advantages: (1) The smoothed cubic NURBS pair are constrained with five control points and can smooth the translation trajectory of the tool tip points and the tool axis points with G^2 continuity, respectively. Then, velocity and acceleration can be improved due to continuities of the tangential direction and curvature. (2) The approximation error has an analytical relationship with the transition length of the smoothed curve. It is easy to construct the analytical double NURBS curves satisfying the pre-defined error limit. (3) The synchronization method can guarantee the continuity in tool orientation variation.

5 ACKNOWLEDGEMENTS

This research is sponsored by the National Natural Science Foundation of China (No. 51305254) and the Capacity Building Project for Local Universities of the Shanghai Science and Technology Committee (No. 14110501200).

6 REFERENCES

[1] Feng, J.C., Li, Y.H., Wang, Y.H., Chen, M. (2010). Design of a real-time adaptive NURBS interpolator with axis acceleration

- limit. *International Journal of Advanced Manufacturing Technology*, vol. 48, no. 1, p. 227-241, DOI:10.1007/s00170-009-2261-y.
- [2] Lasemi, A., Xue, D.Y., Gu, P.H. (2010). Recent development in CNC machining of freeform surfaces: A state-of-the-art review. *Computer-Aided Design*, vol. 42, no. 7, p. 641-654, DOI:10.1016/j.cad.2010.04.002.
- [3] Sencer, B. Ishizaki, K., Shamoto, E. (2015). A curvature optimal sharp corner smoothing algorithm for high-speed feed motion generation of NC systems along linear tool paths. *International Journal of Advanced Manufacturing Technology*, vol. 76, no. 9, p. 1977-1992, DOI:10.1007/s00170-014-6386-2.
- [4] Erkorkmaz, K., Altintas, Y. (2005). Quintic spline interpolation with minimal feed fluctuation. *Journal of Manufacturing Science and Engineering*, vol. 127, no. 2, p. 339-349, DOI:10.1115/1.1830493.
- [5] Beudaert, X., Lavernhe, S., Tournier, C. (2013). 5-axis local corner rounding of linear tool path discontinuities. *International Journal of Machine Tools and Manufacture*, vol. 73, p. 9-16, DOI:10.1016/j.ijmactools.2013.05.008.
- [6] Heng, M., Erkorkmaz, K. (2010). Design of a NURBS interpolator with minimal feed fluctuation and continuous feed modulation capability. *International Journal of Machine Tools and Manufacture*, vol. 50, no. 3, p. 281-293, DOI:10.1016/j.ijmactools.2009.11.005.
- [7] Yau, H.T., Wang, J.B. (2007). Fast Bezier interpolator with real-time lookahead function for high-accuracy machining. *International Journal of Machine Tools and Manufacture*, vol. 47, no. 10, p. 1518-1529, DOI:10.1016/j.ijmactools.2006.11.010.
- [8] De Santiago-Perez, J.J., Osornio-Rios, R.A., Romero-Troncoso, R.J., Morales-Velazquez, L. (2013). FPGA-based hardware CNC interpolator of Bezier, splines, B-splines and NURBS curves for industrial applications. *Computers & Industrial Engineering*, vol. 66, no. 4, p. 925-932, DOI:10.1016/j.cie.2013.08.024.
- [9] Chen, Z.-Z.C., Khan M.A. (2014). A new approach to generating arc length parameterized NURBS tool paths for efficient three-axis machining of smooth, accurate sculptured surfaces. *International Journal of Advanced Manufacturing Technology*, vol. 70, no. 5, p. 1355-1368, DOI:10.1007/s00170-013-5411-1.
- [10] Tulsyan, S., Altintas, Y. (2015). Local toolpath smoothing for five-axis machine tools. *International Journal of Machine Tools and Manufacture*, vol. 96, p. 15-26, DOI:10.1016/j.ijmactools.2015.04.014.
- [11] Langeron, J.M., Duc, E., Lartigue, C., Bourdet, P. (2004). A new format for 5-axis tool path computation, using Bspline curves. *Computer-Aided Design*, vol. 36, no. 12, p. 1219-1229, DOI:10.1016/j.cad.2003.12.002.
- [12] Li, Y.Y., Wang, Y.H., Feng, J.C., Yang, J.G. (2008). The research of dual NURBS curves interpolation algorithm for high-speed five-Axis machining. *Intelligent Robotics and Applications, Lecture Notes in Computer Science*, vol. 5315, p. 983-992, DOI:10.1007/978-3-540-88518-4_105.
- [13] Bi, Q., Wang, Y.H., Zhu, L.M., Ding, H. (2010). An algorithm to generate compact dual NURBS tool path with equal distance for 5-axis NC machining. *Intelligent Robotics and Applications, Lecture Notes in Computer Science*, vol. 6425, p. 553-564, DOI:10.1007/978-3-642-16587-0_51.
- [14] Ho, M.-C., Hwang, Y.-R., Hu, C.-H. (2003). Five-axis tool orientation smoothing using quaternion interpolation algorithm. *International Journal of Machine Tools and Manufacture*, vol. 43, no. 12, p. 1259-1267, DOI:10.1016/S0890-6955(03)00107-X.
- [15] Beudaert, X., Pechard, P.Y., Tournier, C. (2011). 5-axis tool path smoothing based on drive constraints. *International Journal of Machine Tools and Manufacture*, vol. 51, no. 12, p. 958-965, DOI:10.1016/j.ijmactools.2011.08.014.
- [16] Li, W., Liu, Y.D., Yamazaki, K. Fujisima, M., Mori, M. (2008). The design of a NURBS pre-interpolator for five-axis machining. *International Journal of Advanced Manufacturing Technology*, vol. 36, no. 9, p. 927-935, DOI:10.1007/s00170-006-0905-8.
- [17] Pateloup, V., Duc E., Ray, P. (2010). Bspline approximation of circle arc and straight line for pocket machining. *Computer-Aided Design*, vol. 42, no. 9, p. 817-827, DOI:10.1016/j.cad.2010.05.003.
- [18] Zhao, H., Zhu, L.M., Ding, H. (2013). A real-time look-ahead interpolation methodology with curvature-continuous B-spline transition scheme for CNC machining of short line segments. *International Journal of Machine Tools and Manufacture*, vol. 65, p. 88-98, DOI:10.1016/j.ijmactools.2012.10.005.
- [19] Zhang, L.B., You, Y.P., He, J., Yang, X.F. (2011). The transition algorithm based on parametric spline curve for high-speed machining of continuous short line segments. *International Journal of Advanced Manufacturing Technology*, vol. 52, no. 1, p. 245-254, DOI:10.1007/s00170-010-2718-z.
- [20] Shi, J., Bi, Q.Z., Zhu, L.M., Wang, Y.H. (2015). Corner rounding of linear five-axis tool path by dual PH curves blending. *International Journal of Machine Tools and Manufacture*, vol. 88, p. 223-236, DOI:10.1016/j.ijmactools.2014.09.007.
- [21] Piegl, L., Tiller, W. (1997). *The NURBS Book*, Springer-Verlag, Berlin, Heidelberg, DOI:10.1007/978-3-642-59223-2.
- [22] Yuen, A., Zhang, K., Altintas, Y. (2013). Smooth trajectory generation for five-axis machine tools. *International Journal of Machine Tools and Manufacture*, vol. 71, p. 11-19, DOI:10.1016/j.ijmactools.2013.04.002.
- [23] Schneider, P.J., Eberly, D.H. (2003). *Geometric Tools for Computer Graphics*. Elsevier, Amsterdam.

Application of Thermographic Measurements for the Determination of the Impact of Selected Cutting Parameters on the Temperature in the Workpiece During Milling Process

Piotr Zgórniak* – Wojciech Stachurski – Dariusz Ostrowski

Lodz University of Technology, Institute of Machine Tools and Production Engineering, Poland

In this paper, the impact of selected cutting parameters (both cutting and feed speed) on the temperature generated in the workpiece being machined during milling is assessed. The investigations were carried out by milling of 41Cr4 alloy steel using disc cutter mill with F40M sintered carbide inserts with the anti-wear coating. The investigations were conducted with the dry cutting manner. During the investigations three cutting speeds and three feed speeds were applied, with a constant depth of cut. In the course of the investigations, the temperature in the machining, the zone was recorded using the Flir SC6000HS infrared camera. As a result of the measurements, the mean temperature in the defined measurement zone was determined, and, based on that, a procedure for the determination of the t_{W-max} maximum temperature in the workpiece being machined has been proposed. Finally, on the basis of the obtained results, it has been found that the increase in cutting speed leads to the increase in the t_{W-max} maximum temperature, whereas the increase in feed speed leads to the reduction of that temperature in the workpiece being machined.

Keywords: machining, IR measurements, workpiece temperature

Highlights

- Application of thermography measurements for the determination of the temperature produced in the workpiece being machined.
- Description of the methodology of the determination of the t_{W-max} maximum temperature in the workpiece being machined.
- Determination of the impact of both cutting and feed speeds on the t_{W-max} maximum temperature, in the workpiece being machined.

0 INTRODUCTION

It is well known that the temperature distribution in the cutting zone is highly uneven which causes this zone to be characterized by the presence of a complex temperature field. Because of that, in the literature, e.g. [1], the term of the t cutting temperature is introduced, i.e. the mean temperature on the contact of the cutting edge with chip and the machined surface. In most cases as the cutting temperature the mean temperature in the zone of the contact of the chip with the rake face of the cutting tool is assumed. That temperature is the result of the summary effect of the heat generated due to the plastic strain in the shear zone and the friction of the chip against the rake face of the tool.

Because of the above, many researchers are involved in the determination of the t temperature and analysis of its adverse impact on the cutting edge of the cutting tool. This impact is mainly seen with the reduction of machinability resulting from the reduction of the hardness and durability of the cutting edge [1] to [3].

The temperature distribution in the cutting zone also includes the workpiece being machined. The t_W

temperature occurring there is the combined effect of the heat generated due to the friction of the flank face of the tool against the machined surface, and the plastic strains preceding the shear of workpiece material and penetrating the surface layer of the workpiece. The adverse effect of temperature in the workpiece being machined may result in the occurrence and increase of adverse internal stresses in the surface layer, or changes in linear dimensions occurring during cooling down, and by this causing errors in the quality of final products [2] and [4]. It should be noted here that the maximum values of the t_{W-max} temperature occurring in the workpiece being machined are normally much lower than those in chips and the tool [4].

The main factor affecting the temperature value and its distribution in the tool zone, the workpiece being machined and the chip are: the properties of the material being machined and that of the tool, cutting parameters, the cutting edge stereometry and the type and way of cooling down and finally the type of machining operation [5]. As has already been mentioned, most researchers concentrate on the analysis of the cutting edge temperature. In many publications, e.g. [1], the order of the importance of

*Corr. Author's Address: Lodz University of Technology, Institute of Machine Tools and Production Engineering, ul. Stefanowskiego 1/15, 90-924 Łódź, Poland, piotr.zgorniak@p.lodz.pl

the impact of cutting parameters on the t temperature value is described. The strongest impact comes from the v_c , cutting speed, whereas the impact of the f feed is definitely lower. The impact of the a_p cutting depth on the t temperature can normally be neglected. In the study [6], the impact of cutting parameters on cutting temperature was described via the experimental relationship:

$$t = C_t \cdot f^{y_t} \cdot v_c^{z_t} \quad (1)$$

where C_t , y_t , and z_t are constants determined experimentally. For example, for turning low-carbon steel with tool made of sintered carbides the following was obtained:

$$t = 410 \cdot f^{0.13} \cdot v_c^{0.23}, \quad (2)$$

and the results are presented in Fig. 1.

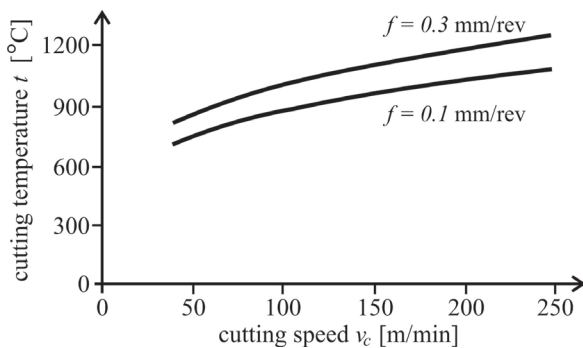


Fig. 1. The impact of cutting speed and feed on the temperature of the cutting blade made of sintered carbides

The comparison of the exponents in the (2) confirms the impact of cutting parameters described above on cutting temperature: the higher impact comes from cutting speed, and the lower one from the feed. As can be seen in Fig. 1, increases in both cutting speed and feed leads to the increase in the temperature of the cutting edge.

The impact of cutting parameters on the temperature of the workpiece being machined is also described in the literature. However, it concerns selected machining conditions and a narrow group of materials being machined. Le Coz and Dudziński [7] carried out investigations concerning the impact of cutting speed on the temperature of the workpiece being machined during the milling of Inconel 718 alloy without the use of any cutting fluid. The investigations were carried out with constant feed and cutting depth. On the basis of those investigations, it was found that similarly as in the case of the temperature of the cutting edge, temperature also increases along with the increase in cutting speed. In

another study, O'Sullivan and Cotterell [8] determined the impact of cutting parameters on the temperature of the workpiece during the machining of aluminium alloy. Also, in this case, a similar nature of the temperature changes of the workpiece was observed due to changes in cutting speed. In the case of changes in feed, the matter looked differently. With the increase in feed, the temperature was dropping.

Another important issue that results from the review of the available literature is the influence of many factors, such as cutting conditions, the type of machining process employed to manufacture the part, etc. on the temperatures registered in the cutting zone, particularly within the workpiece. The biggest differences in the temperature values, obtained during the cutting process, result from the type of work performed by the cutting edge. In the case of continuous cutting processes, such as turning or orthogonal cutting, temperatures are much higher than in the case of intermittent cutting once that occurs in the milling process. For example, in [9], Inconel 718 and Ti-6Al-6V-2Sn was machined. Depending on cutting conditions, temperatures obtained in the cutting zone during turning operations ranged from 600 °C to 1050 °C. In the case of intermittent cutting, temperatures measured on the rake face of the tool varied from 350 °C to 800 °C. Referring to the results for the orthogonal cutting presented by Artozoul et al. [10], tool temperatures measured with an IR camera ranged from 335 °C to 670 °C. For comparison, Jiang et al. measured workpiece temperature (1045 steel) by thermocouples during the milling process [11]. Among others results presented in this paper, scientists obtained workpiece temperatures ranging from 35 °C to 70 °C for the cutting speeds from 500 m/min to 3000 m/min.

Such a disparity in the obtained temperature values is connected with the nature of the intermittent cutting process in which variable times of heating and cooling appear in the cutting zone. During milling, the ratio of cutting time to time of brake in cutting has a very significant effect on the heat balance in the cutting zone, and thus the value of recorded temperatures. The value of this ratio is primarily determined by the number of cutting teeth, the diameter of the tool or even the dimensions of the samples used in the tests. All this makes it very difficult to compare results achieved in other scientific centres even if was conducted under comparable conditions.

For the determination of cutting temperature analytical, numerical, and experimental methods are used [3] and [4]. In experimental methods, one very popular way of the monitoring of temperature is

the thermography method using infrared radiation. However, the application of the thermography is not easy in practice [8]. Due to the high sensitivity of this method and the influence of environmental factors on the accuracy of the determination of temperature by means of an IR camera, the interpretation of thermographs requires extensive knowledge and experience in many fields [3] and [12]. Nevertheless, according to the opinions of authors [4], this method illustrates very well the maximum temperatures occurring in the workpiece during the cutting process.

Despite the fact that infrared measurements are considered particularly useful when the tool is rotating, the factors affecting the value of the recorded temperature must be mentioned. One of them is the phenomenon of changes in the emissivity of objects with changes of temperature into the cutting zone. One of the most common ways to eliminate this negative phenomenon is the use of the mean emissivity coefficient for objects made from the same construction materials and equal surface properties. In addition, for the proper determination of the temperature in different areas of the cutting zone often it is necessary to perform many tests and trials to obtain comparable values of temperatures for each component from recorded scene such as the tool, chips, workpiece, surrounding area, etc.

Another way to eliminate the phenomenon of changing emissivity is to apply constant measurement conditions, giving the possibility to use the results of the comparative analysis.

Due to the above drawbacks, many researchers performed analysis of thermal phenomena using the finite element method [13]. The advantage of this solution is undoubtedly the ability to make rapid changes in input variables, regarding the conditions and treatment of its course, in a wider range than is possible in experimental studies. It is thus less expensive, sometimes faster and simpler to implement. However, it should be kept in mind that the temperature values and temperature distributions generated by computer programs do not correspond to strictly experimental results. In addition, lack of knowledge about the algorithms used or assumptions made may result in incorrect conclusions. For obvious reasons, such a comparative analysis of the results obtained from infrared measurement with the results obtained by means of finite element method analysis loses its meaning.

In the Institute of Machine Tools and Production Engineering of the Lodz University of Technology some tests for the measurements of temperature by the thermography method during milling with the

use of disc mills were carried out. The investigations were aimed at the development of the methodology of the measurements of the tW temperature in the area of the workpiece being machined along with its determination, and to determine the impact of selected cutting parameters on the tW temperature value.

1 CONDITIONS OF EXPERIMENTAL INVESTIGATIONS

In the course of the investigations the samples sized 70 mm × 70 mm × 5 mm made of 41Cr4 normalized steel were milled. The milling with the backward method was carried out on a conventional horizontal milling machine.

As the tool, the 335.18-125.17.40-4N disc mill manufactured by SECO was used. It is a three-sided mill clamped on the cutter arbor (An FP type) with 12 cutting edges of the total cutting width $a_e = 17$ mm. Due to the significantly smaller width of the samples (5 mm) 4 edges (no. 1, 4, 7 and 10) arranged on the circumference of the tool every 90° were used. The way of the setting up of the mill in relation to the material being machined is illustrated in Fig. 2. The LNKT060504PPN-E05 cutting inserts made of F40M sintered carbides from the P40 application area with anti-wear (Ti, Al)N/TiN multilayer coating were used. F40M is the PVD-coated grade for the fine to medium rough milling. The corner radius of the insert was $r_e = 0.4$ mm, and the tool rake angle $\gamma = 15^\circ$ [14].

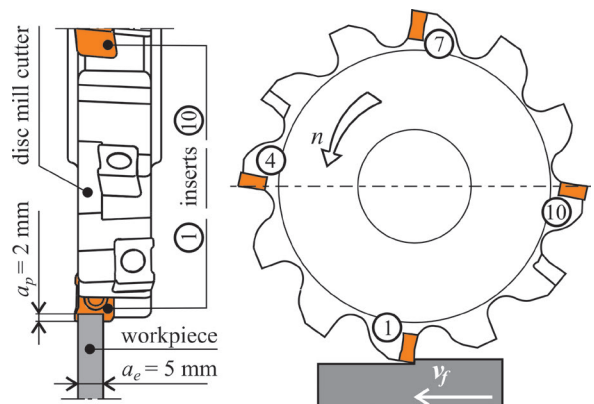


Fig. 2. The view of the cutting zone

Machining was carried out without the use of any cutting fluids (dry machining). Cutting parameters were selected on the basis of the manufacturer's data [15] and the workshop practice. The parameters are presented in Table 1.

The investigation included nine cutting tests. For three cutting speed values, three feed speed levels have been selected. All tests have been done with constant

depth of cut $a_p = 2$ mm. Each test has been recorded by scientific infrared camera Flir SC6000HS.

Table 1. Cutting parameters

Test No	Feed speed v_f [mm/min]	Cutting speed v_c [m/min]	Depth of cut a_p [mm]
1	42	55	2
2	52		
3	69		
4	42		
5	52	69	
6	69		
7	42	86	
8	52		
9	69		

2 THE METHODOLOGY OF THERMOGRAPHIC MEASUREMENTS

During the measurements, thermal photos were recorded with the use of the dynamic expansion of the measurement range of the Flir SC6000HS infrared camera [16] and [17]. To this end, three temperature sub-ranges were used. This enabled assessing the produced temperature in the range of 360 °C, wider than the standard one which is about 120 °C. The milling process was recorded at the maximum possible recording level using 6000 frames being recorded with the ultimate frequency up to 100 Hz. This limitation was caused by the quantity of data being recorded in the RAM memory of the available computer and the possibilities of the recording of infrared thermographic sequences on the hard disk of this computer.

The photos were taken with the resolution of 128×160 pixels. It means that each thermal frame consists of 128 rows and 160 columns. Because the value of the temperature being recorded is affected by many factors, including the change of the thermal emissivity of the workpiece being machined as temperature increases, in the investigations described here, the average emissivity coefficient $\varepsilon = 0.14$ was assumed. The value of this coefficient was obtained based on the emissivity table [17]. This assumption has caused that the ambient temperature being recorded in cutting tests was taking the value of about 45 °C. In fact, the ambient temperature was lower, but the assumption of the thermal emissivity ($\varepsilon = 0.92$) corresponding to that temperature would cause the temperatures being recorded concerning the material being machined to be understated.

For the support of the infrared camera, the IR Control software was used, the graphical interface of which is shown in Fig. 3. The program enables to record the sequences of thermal photos and then, based on the photos, to determine the mean mean temperature in the AOI0 area which corresponds to the whole thermal frame. Mean temperatures were calculated for the whole sequence. The example of first stage results is presented in Fig. 4. In the second stage authors investigated only the areas that correspond to the workpiece location. Because in each frame the position of the workpiece was different, and the workpiece was moving, only maximum temperatures from rows that correspond to the location of the workpiece were taken into consideration. The maximum temperature was found for a selected frame where the mean maximum temperature was observed and cutting process took place. The next step considered the determination of maximum temperature for the columns where the maximum temperature appeared in the location of the workpiece. The example of the results of maximum temperature in selected frame 3673 is presented in Fig. 6. Here, you can observe greater temperatures concerning chips and lower workpiece temperatures (columns from 1 to 108).

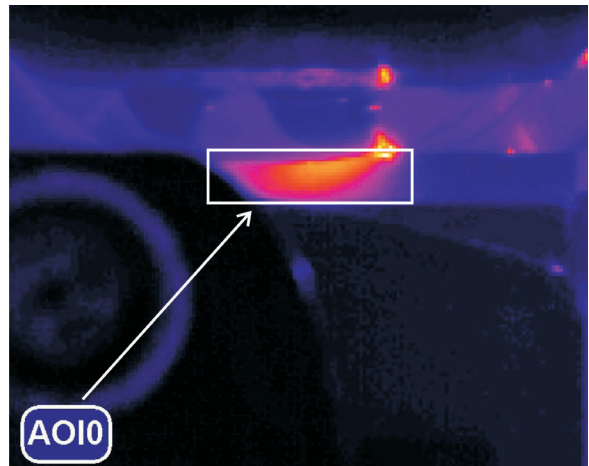


Fig. 3. Graphical interface of the IR Control software

The process of the determination of the temperatures occurring during milling and their assessment were conducted in two stages.

In the first stage, a sequence of thermal photos was recorded (6000 frames), and 9 such sequences were recorded in accordance with the cutting parameters listed in Table 1 (three cutting speeds for three feed values). Next, for each sequence, the program was automatically determining the t_{mean} mean temperature

value from the AOIO area, thus enabling drawing up a chart of the course of its changes during machining.

However, the limitation in the precise definition of the analysed area should be taken into consideration so that it covers the zone of the workpiece being machined. Because of that, the determination of the t_{mean} temperature is burdened with serious error since the mean temperature value is determined from the area where the temperature of the workpiece being machined, the tool and chips and the environment are recorded. In addition, the milling process is characterized by the lack of permanent contact of the cutting edge with the workpiece being machined and the excess material removed by the cutting edge is uneven. All this leads to the fact that the chart of the course of the changes of the temperature being measured is not stabilized, and the mean temperature value may differ significantly from the maximum temperatures. Fig. 4 illustrates the inconsistencies described above. The charts were made up for three v_c cutting speeds at the constant feed speed $v_f = 42$ mm/min and they are limited to the time of 30 seconds from the start of machining. When analysing the obtained courses, some local increases in temperature can be noted. This is especially well seen when analysing the chart for the cutting speed $v_c = 69$ mm/min in the time interval from the 13th up to the 17th second. The disturbances of this type are caused by the presence of the heated up chips the temperature of which increases the mean temperature in the thermal photo frame.

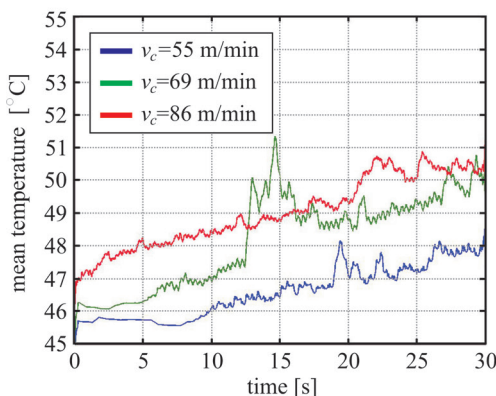


Fig. 4. Mean cutting temperature for the constant feed speed $v_f = 42$ m/min

In the authors' opinion, only the maximum temperature values being recorded in the course of the contact of the cutting edge with the workpiece being machined can be the basis for the determination of cutting temperature and its assessment.

Consequently, the authors developed a procedure for the determination of the maximum temperatures based on the thermographic sequences recorded earlier. That procedure was used in the 2nd stage of the investigations. This stage was limited to the determination of the t_{W-max} maximum temperature in the workpiece being machined only.

For each single thermal photo sequence, that procedure was starting from the selection of the thermal image in which the cutting with one of four cutting edges was observed. This was because each cutting edge was removing the different amount of the excess material because of the uneven protrusion of cutting inserts from the mill body, and the run-out of the cutter arbor. During the initial analyses of the thermographs, it was found that those factors significantly affect the values of the generated temperatures. Then, from such selected frames, those corresponding to the period after the thermal machining conditions had been stabilized were taken. In practice, they were the frames recorded from the time when half of the milling travel (distance) was reached. The procedure of the determination of the maximum temperature was finishing with the selection of one representative frame of thermal photos and, based on that, the determination of the value of the t_{W-max} temperature. To this end, the selected frame was exported to the *.mat format, and then the distribution of temperature fields was determined in the MatLAB software. As a result of the export, two files come into being. The first one contained the information coming from the calibration file of the infrared camera for specific measurement conditions, whereas the second one included the data concerning the signal values in consecutive matrix pixels of the size equal to the resolution of the thermal frame. Consequently, information the maximum value in the area of the workpiece being machined can be read in the chart of the temperature fields.

For the consecutive sequences of thermal images, the described procedure was repeating itself, whereas every time the same cutting edge was taken into consideration.

3 RESULTS OF THE INVESTIGATIONS

In Fig. 5, an example of the chart of the distribution of the temperature fields for the single frame (no. 3673) selected from the sequence of thermal photos is presented. The frame was selected using the procedure described in Section 2. The chart was obtained for the cutting speed $v_c = 86$ m/min and the feed speed $v_f = 69$ mm/min. In order to improve the contrast

between the isothermal lines of the frame being analysed, the range of the colour changes at the display of various temperatures was narrowed to 60 °C. This was done to improve the readability of the chart.

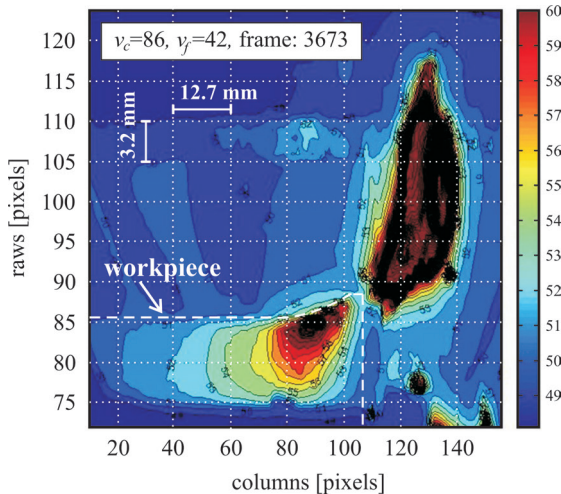


Fig. 5. The distribution of temperature fields for $v_c = 86$ m/min, $v_f = 69$ m/min; frame no. 3673

The process of the determination of the t_{W-max} maximum temperature was starting from the drawing up of the chart of temperature profiles for consecutive columns of the selected frame. Each profile corresponded to one row of the frame. As a result, the chart presented in Fig. 6 was obtained.

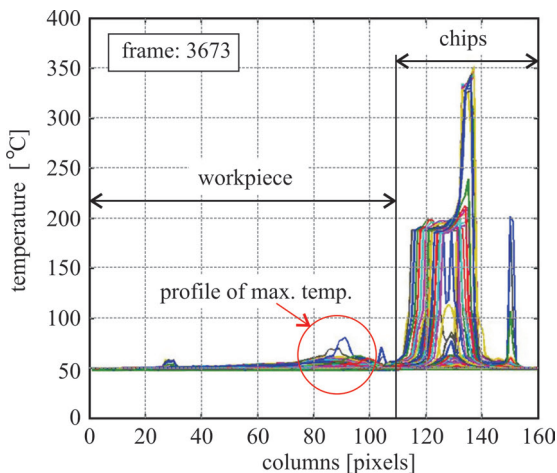


Fig. 6. The temperature profiles for the consecutive columns of the analysed frame no. 3673

After comparing Fig. 6 with Fig. 5 it can be seen that the workpiece is included in the columns from 0 up to 110. The highest temperature value read in that range was 84.37 °C. It should be observed here that

the temperatures being recorded on chips are close to 350 °C (columns from 110 up to 140). The so determined temperature was assumed as the maximum temperature value in the workpiece being machined and compared with the temperatures determined for the frames obtained for other sequences of thermal photos.

In Fig. 7, as an example a chart is presented in which the profiles of the t_{W-max} maximum temperatures obtained for three v_c cutting speeds at constant feed speed $v_f = 42$ mm/min are plotted.

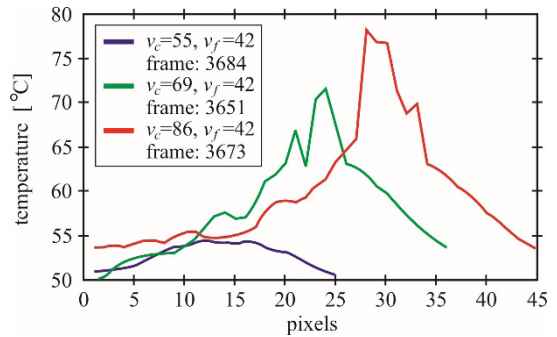


Fig. 7. The profiles of the t_{W-max} maximum temperatures for different v_c cutting speeds at constant feed speed $v_f = 42$ mm/min

Based on the chart presented above it can be seen that the increase in cutting speed at constant feed speed leads to the fact that the t_{W-max} maximum temperature in the workpiece being machined increases. The values of the measured maximum temperature, and, for comparison, the t_{mean} mean temperature are tabulated in Table 2. The similar character of the relationship between temperature and cutting speed was observed for the other two v_f feed speeds.

Table 2. The maximum and the mean temperature in the workpiece for $v_f = 42$ mm/min

cutting speed v_c [m/min]	feed speed v_f [mm/min]	max. temp. t_{W-max} [°C]	mean temp. t_{mean} [°C]
55	42	54.57	50.03
69	42	71.58	53.59
86	42	78.20	54.27

Based on the results presented in Table 2, it can be seen that the values t_{W-max} of the maximum temperatures in the workpiece differ substantially from the values t_{mean} of the mean temperatures. Only for the cutting speed $v_c = 55$ m/min is the difference small, and it amounts to about 9 %. For the two other cases, i.e. $v_c = 69$ m/min and $v_c = 86$ m/min this difference amounts to 33 % and 44 % respectively.

In Fig. 8, as an example a chart with the t_{W-max} profiles of the maximum temperatures plotted is presented. The profiles were obtained for three v_f feed speeds at constant cutting speed $v_c = 86$ m/min.

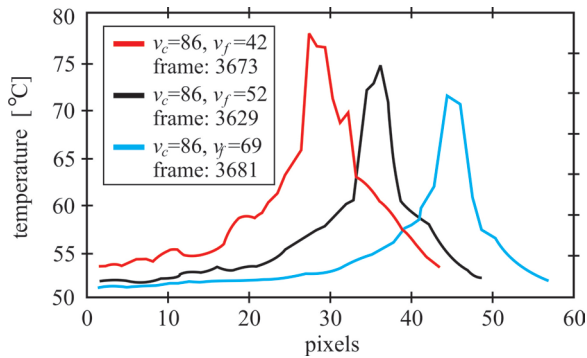


Fig. 8. The profiles of the t_{W-max} maximum temperatures for different v_f feed speeds at constant cutting speed $v_c = 86$ m/min

On the basis of the chart presented above it can be seen that the increase in feed speed at constant cutting speed leads to the drop of the t_{W-max} maximum temperature in the workpiece being machined. The values of the maximum measured temperature, and, for comparison, the mean mean temperature, are tabulated in Table 3. A similar character of the relationship between temperature and feed speed has been observed for the two other v_c cutting speeds.

Table 3. The maximum and the mean temperature in the workpiece for $v_c=86$ m/min

cutting speed v_c [m/min]	feed speed v_f [mm/min]	max. temp. t_{W-max} [°C]	mean temp. t_{mean} [°C]
86	42	78.20	54.27
86	52	74.95	53.94
86	69	71.37	53.55

The feature described above is justified in the fact that the increase in feed speed at the same cutting speed leads to the increase in the volume of the material being removed by the tool cutting edge. Thereby the share of the chips in the carrying away of heat from the cutting zone increases.

Based on the results presented in Table 3 it can be seen that the values of the t_{W-max} maximum temperatures differ substantially from the values of the t_{mean} mean temperatures. For the speed $v_f = 42$ mm/min that difference amounts to 44 %, for $v_f = 52$ mm/min it is 39 % and for $v_f = 69$ m/min: 33 %.

However, results obtained by authors might seem to be too low; it should be taken into consideration that differences in comparison to others' works are

the result of the methodology adopted. Kitigawa et al. [9] investigated temperature during the high-speed machining of Inconel 718 and Ti-6Al-6V-2Sn hard to cut materials. It is not surprising that in this case, authors obtained a higher temperature value (350 °C). Temperatures have been determined by a thermocouple mounted into single point cutting tool. In the paper Artozoul et al. [10], investigated infrared measurements, but temperatures were investigated using an orthogonal cutting model, and the temperature was determined by a cutting tool, not in the workpiece. In this case, intermittent cutting phenomena was not taken into consideration, so the values were higher than author's results. Moreover, cutting parameters used by Artozoul et al. [10], are higher ($v_c = 100$ m/min and $v_c = 250$ m/min) than values applied in our tests, so it is not surprising that the values obtained in these studies are higher. Referring to the work of Jiang et al. [11], temperatures were measured by a thermocouple mounted into the workpiece, and an intermittent cutting effect appeared during the cutting test. Here, the results of the workpiece temperature obtained by the authors are close to ours, despite the fact that the cutting velocity applied was higher and ranges from 500 m/min to 3000 m/min. In this case, the measured temperatures obtained ranges from 30 °C to 70 °C.

3 CONCLUSIONS

On the basis of the results presented above, the following conclusion can be formulated:

1. The use of an infrared camera enables carrying out the analyses of the impact of cutting parameters on the temperature generated in the workpiece being machined.
2. For the investigations of cutting processes, the maximum temperature should be used. It is more reliable than the mean temperature.
3. The application of the method proposed by the authors enables the precise temperature analyses for the individual cutting edges. This is so because the limitation in the temperature recording time to the period in the conditions stabilized by the elimination of the heating up phase (start of cutting) and the retraction of the tool from the workpiece phase makes it possible to increase the frequency of recording thermal images. On the basis of the current investigations [12], it was found that the phases of entering and retracting the tool to/from the workpiece being machined cause significant discrepancies in the final results being obtained.

4. The increase in the cutting speed at constant feed speed in the investigated range causes the increase in the t_{W-max} maximum temperature in the workpiece being machined.
5. The increase in the feed speed at constant cutting speed in the investigated range causes the t_{mean} mean temperature to drop in the workpiece being machined. This is because the share of chips in carrying away the heat from the cutting zone increases.
6. The level of temperature values presented in the paper, concerning workpiece temperature distribution, is close to the results presented in other available literature, e.g. [11]
7. Further investigations should take into account the variability of the thermal emissivity coefficient as the temperature in various areas of the cutting zone increases. It is planned to take into account the changes of the emissivity coefficient of the workpiece being machined, the tool, and the environment.
8. Despite the fact that thermocouple measurements have many disadvantages, e.g. difficulties in precise location in the workpiece, disruption of thermal field, measurements only in one or several points into the cutting zone, etc., it might be a good idea to use this measuring method for the validation and calibration of thermographic measurements. This issue will be the subject of future research.

4 REFERENCES

- [1] Grzesik W. (2008). *Advanced Machining Processes of Metallic Materials. Theory, Modeling and Applications*, Elsevier Science, Amsterdam.
- [2] Grzesik, W., Kruszyński, B. Ruszaj, A. (2010). Surface integrity of machined surfaces. Davim, J.P. (ed.) *Surface Integrity in Machining*, Springer, London, DOI:10.1007/978-1-84882-874-2.
- [3] Abukhshim, N.A., Mativenga, P.T., Sheikh, M.A. (2006). Heat generation and temperature prediction in metal cutting: A review and implications for high speed machining. *International Journal of Machine Tools and Manufacture*, vol. 46, no. 7-8, p. 782-800, DOI:10.1016/j.ijmachtools.2005.07.024.
- [4] Da Silva, M.B., Wallbank, J. (1999). Cutting temperature: prediction and measurement methods – a review. *Journal of Materials Processing Technology*, vol. 88, no. 1-3, p. 195-202, DOI:10.1016/S0924-0136(98)00395-1.
- [5] Byrne G., Dornfeld, D., Denkena, B. (2003). Advancing cutting technology. *CIRP Annals - Manufacturing Technology*, vol. 52, no. 2, p. 483-507, DOI:10.1016/S0007-8506(07)60200-5.
- [6] Jemielniak, K. (2012). *Metal Machining*. Warsaw University of Technology Publishing House, Warsaw. (in Polish)
- [7] Le Coz, G., Dudzinski, D. (2014). Temperature variation in the workpiece and in the cutting tool when dry milling Inconel 718. *The International Journal of Advanced Manufacturing Technology*, vol. 74, no. 5, p. 1133-1139, DOI:10.1007/s00170-014-6006-1.
- [8] O'Sullivan, D., Cotterell, M. (2002). Workpiece temperature measurement in machining. *Proceedings of the Institution of Mechanical Engineers, Part B: Journal of Engineering Manufacture*, vol. 216, no. 1, p. 135-139, DOI:10.1243/0954405021519645.
- [9] Kitigawa, T., Kubo, A., Maekawa, K. (1997). Temperature and wear of cutting tools in high-speed machining of Inconel 718 and Ti-6Al-6V-2Sn. *Wear*, vol. 202, no. 2, p. 142-148, DOI:10.1016/S0043-1648(96)07255-9.
- [10] Artozoul, J., Lescaulier, Ch., Bomont, O., Dudzinski, D. (2014). Extended infrared thermography applied to orthogonal cutting: Mechanical and thermal aspects. *Applied Thermal Engineering*, vol. 64, no. 1-2, p. 441-452, DOI:10.1016/j.applthermaleng.2013.12.057.
- [11] Jiang, F., Liu, Z., Wan, Y., Shi, Z. (2013). Analytical modeling and experimental investigation of tool and workpiece temperatures for interrupted cutting 1045 steel by inverse heat conduction method. *Journal of Materials Processing Technology*, vol. 213, no. 6, p. 887-894, DOI:10.1016/j.jmatprotec.2013.01.004.
- [12] Kuczmaszewski, J., Zagórski, I. (2013). Methodological problems of temperature measurement in the cutting area during milling magnesium alloys. *Management and Production Engineering Review*, vol. 4, no. 3, p. 26-33, DOI:10.2478/MPER-2013-0025.
- [13] Özel, T., Altan, T. (2000). Process simulation using finite element method – prediction of cutting forces, tool stresses and temperatures in high-speed flat end milling. *International Journal of Machine Tools and Manufacture*, vol. 40, no. 5, p. 713-738, DOI:10.1016/S0890-6955(99)00080-2.
- [14] SECO (2014). 335 Series Disc Milling, from <http://www.secotools.com>, accessed on 2015-06-17.
- [15] SECO (2014). Milling – catalogue and technical guide, from <http://www.secotools.com>, accessed on 2015-06-17.
- [16] Zgórnjak, P., Grdulska, A. (2012). Investigation of temperature distribution during milling process of AZ91HP magnesium alloys. *Mechanics and Mechanical Engineering*, vol. 16, no. 1, p. 33-40.
- [17] Bramson, M.A. (1968). *Infrared Radiation, A Handbook for Applications*. Plenum Press, New York, DOI:10.1007/978-1-4757-0911-7, DOI:10.1007/978-1-4757-0911-7.

Stiffness and Damping Model of Bolted Joints with Uneven Surface Contact Pressure Distribution

Yongsheng Zhao^{1,*} – Cheng Yang¹ – Ligang Cai¹ – Weimin Shi² – Yi Hong¹

¹ Beijing University of Technology, Key Laboratory of Advanced Manufacturing Technology, China

² Beijing University of Technology, College of Computer Science, China

Bolted connections are widely employed to fix the structural components, in which the bolted joint is one of the weakest parts and can significantly affect the dynamic characteristics of the machine tool. In this research, a stiffness and damping model based on the uneven surface contact pressure is presented for the bolted joint to accurately predict the dynamic characteristic of a bolted assembly. The normal and tangential stiffness and damping of the contact surface can be deduced based on the fractal contact theory. However, the contact surface pressure of bolted joint is unevenly distributed due to the influence of the concentrated force of multi-bolts. Therefore, the pressure of the contact surface is introduced to define the stiffness and damping of bolted joint. The assumption is that the contact surface is flat in the macro-scale. Then, we can obtain the pressure distribution of contact surface through the finite element (FE) method. The nonlinear relationship of stiffness, the damping of the bolted joint, and the pressure of contact surface can be obtained and assigned to the FE model based on the pressure distribution of the contact surface. An experimental set-up with a box-shaped specimen is designed for validating the proposed model. The equal pre-tightening force and bending moment effect case studies are provided to demonstrate the effectiveness of the model. The results show that the proposed model can be used to accurately predict the dynamic characteristic of the machine tool.

Keywords: bolted joint, contact stiffness and damping, fractal contact theory, uneven pressure distribution, machine tool

Highlights

- A stiffness and damping model based on the uneven surface contact pressure is presented for the bolted joint to accurately predict the dynamic characteristic of a bolted assembly.
- The surface contact pressure is introduced to define the stiffness and damping of bolted joint, in which the uneven pressure distribution of contact surface can be obtained through the finite element (FE) method.
- The nonlinear relationship of stiffness, the damping of the bolted joint, and the pressure of contact surface can be obtained and assigned to the FE model based on the pressure distribution of the contact surface.
- An experimental set-up with a box-shaped specimen is designed for validating the proposed model.
- The equal pre-tightening force and bending moment effect case studies are provided to demonstrate the effectiveness of the model.

0 INTRODUCTION

It is well known that the dynamic behaviour of bolted joints plays a significant role in determining the machining stability and precision of a machine tool. The dynamic behaviour of bolted joint can be affected by the geometry and machining precision of the surface, the property of material, external load, and pre-tightening force of bolts [1]. All of those factors and the complicated contact mechanism make it difficult to build an accurate model of bolted joints. The bolted joint also shows a strong nonlinear property, and it depicts with difficulty the relationship of the dynamic characteristic of bolted joints and influencing factors. The displacement measurement techniques can be used to obtain the frictional properties of bolted joint, such as LVDT Method [2], extensometer method [3], digital image correlation method [4] and [5], laser interferometer [6] or ultrasound method [7]. However, the contact surface of a bolted joint is difficult to measure directly by using

those experimental methods. Recently, the receptance coupling substructure analysis (RCSA) method was adopted to identify the stiffness and damping of bolted joints [8] to [10]. However, the RCSA method is easily affected by the measuring noise and environment. The identified results could not be applied to the bolted assembly with different technological parameters.

The micro-contact theory is another method to obtain the contact stiffness and damping of bolted joints, which make it possible to accurately model bolted joints and to optimize bolted assemblies. The micro-contact mechanics of bolted joints is based on the geometry topography of surface and Hertz contact theory. There are three methods in geometry topography of surface: the statistics method [11], the fractal geometry method [12], and the reconstruction of experimental data method [13]. The statistics method can be affected by the resolution and sampling length of the measuring instrument, which do not adequately reflect all features of the rough surface. However, the actual surface is always multi-scaled

*Corr. Author's Address: Beijing University of Technology, Key Laboratory of Advanced Manufacturing Technology, China, yszhao@bjut.edu.cn

with non-uniform asperities. The reconstruction of the experimental data method is also limited by the testing instrument. In contrast, the fractal geometry method has the merit of independent resolution and sampling length of measuring instrument and is suitable for the machined surface [14]. Therefore, researchers have focused on studying the contact mechanics of surface based on the fractal contact theory.

For the normal and tangential contact stiffness of bolted joints, most researchers have studied the contact model of asperities based on the Hertz contact theory and obtained the contact stiffness by integrating each micro-contact in the contact surface. Majumdar and Bhushan [14] and [15] introduced scale-independent fractal parameters to characterize the contact surface topography, known as the Majumdar-Bhushan (MB) model. Zhang et al. [16] built up the fractal model for normal contact stiffness of machine joint surfaces based on the Hertz contact theory between a sphere and a plane. Jiang et al. [17] used three different machining methods (milling, grinding, and scraping) iron specimens to obtain the contact stiffness under different contact loads. Shi et al. [18] established the contact stiffness and micro parameters on the joint surface based on the Greenwood and Williamson theory. Sherif [19] found that the ratio between the normal and tangential contact stiffness is constant and is merely a function of Poisson's ratio of the contact surfaces. Fuadi et al. [20] estimated the tangential contact stiffness of the contact interface with controlled contact asperities based on an experimental method.

For the normal and tangential contact damping of bolted joints, the energy dissipation model of bolted joints is adopted to obtain the contact damping. Zhang and Ding [21] proposed a fractal model of normal damping for joint interfaces based on the modified MB fractal model and mechanism of normal contact damping dissipating energy. Bograd et al. [22] studied tangential damping parameters based on a generic isolated joint test bench. The influence of joint parameters, such as normal contact force and frequency dependence is examined. Li et al. [23] proposed the fractal prediction model of the tangential contact damping of joint surface based on the "solid-gap-solid" contact model and the Hertz theory. Zhang et al. [24] also proposed tangential contact damping of joint interfaces by considering the mechanism of energy dissipation and the elastic-plastic deformation regime of joint plane interfaces. The studies show that the stiffness and damping model of contact surfaces have a close relationship with pre-tightening force, geometry, material and other influencing factors,

and could be modeled by using the fractal method. Nevertheless, it does not correspond well with the case of a larger contact area and sparse distribution of multi-bolts.

The main objective of this study is to obtain the normal and tangential stiffness, and the damping of the bolted joint with uneven pressure distribution. The contact surface is assumed as flat in macro-scale, and the finite element method is used to obtain the uneven pressure distribution. The relationship of stiffness, damping, and pressure of contact surface can be deduced based on the fractal contact theory. The finite element model of assembly with bolted joint can be established, in which the MATRIX27 element is introduced to define the bolted joint. An experimental set-up with two box-shaped specimens is designed for validating the presented model. By comparing the experimental and theoretical natural frequency and mode shape, the maximum error of presented model is less than 5.1 %. The equal pre-tightening force and bending moment effect cases are also considered to demonstrate the effectiveness of the presented model.

1 NORMAL AND TANGENTIAL STIFFNESS, DAMPING MODEL BASED ON THE CONTACT PRESSURE

The normal, tangential stiffness and damping model is widely adopted to depict the bolted joint. It is usually assumed to be equal for each stiffness and damping element in the overall contact surface during the process of modelling the bolted assembly [8] to [10]. However, this hypothesis is not suitable for the bolted joint because of the influence of the concentrated force of multi-bolts. The uneven pressure distribution makes the stiffness and damping of bolted joint different for each other in the contact surface. In this section, the contact pressure is assumed to be evenly distributed locally but unevenly distributed across the whole contact surface. The contact pressure of surface is used as a variable to deduce the stiffness, damping of the contact surface.

1.1 Normal Stiffness and Damping Model

Fractal geometry theory can describe profile features of a rough surface and thus provide a means of characterizing asperities of a large range of sizes. Previous studies [12] to [14], have shown that machined surface can be simulated by the Weierstrass-Mandelbrot (W-M) function as:

$$z(x) = G^{(D-1)} \sum_{n=0}^{n_{\max}} \left(\frac{\cos 2\pi\gamma^n x}{\gamma^{(2-D)n}} \right) \quad 1 < D < 2, \gamma > 1, \quad (1)$$

where, n is the frequency index, n_{\max} is the upper limit of frequency, Z is the height of the machined surface, z is the lateral distance, γ denotes the scaling parameter for determining the spectral density and self-affine property, G is the fractal roughness parameter where a higher value of G indicates a rougher surface. D denotes the fractal dimension of a surface profile, which determines the contribution of high and low-frequency components in the surface profile. The fractal parameters D and G can be obtained by the power spectral density method based on the measured data of surface.

Nominal flat surfaces are rough in micro-scale. When brought into contact, an asperity is plastically or elastically deformed depending on its size. For simplicity, the two contact rough surfaces are supposedly equivalent to an assumed rigid flat surface and a rough surface, as shown in Fig. 1a. The real contact area is only a very small part of the nominal contact area ($< 1\%$). It is assumed that the numerous circular asperities are sufficiently apart from each other, and the asperities interactions are neglected [24]. The statistical distribution of the truncated micro-contact area a' can be described as [6]:

$$n(a') = \frac{1}{2} D \psi^{(2-D)/2} a_L^{D/2} a'^{-(2+D)/2} \text{ for } 0 < a' \leq a'_L, \quad (2)$$

where, $a' = 2a$ represents the truncated area of a micro-contact, and a is the real contact area of a micro-contact, a'_L is the truncated area of the largest elastic micro-contact, which is shown in Fig. 1b, ψ describes the domain extension factor for micro-contact size distribution and decided by the equation:

$$\left[\psi^{(2-D)/2} - (1 + \psi^{-D/2})^{-(2-D)/D} \right] / [(2-D)/D] = 1. \quad (3)$$

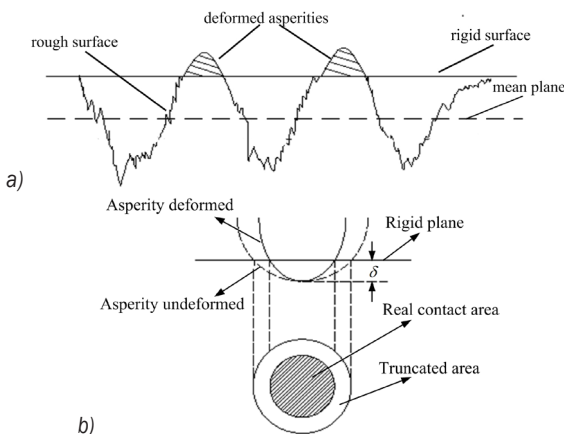


Fig. 1. Contact mechanism; a) contact of a rough surface and a flat surface, and b) contact region of a single asperity

The critical truncated area demarcating the elastic and plastic deformation regimes can be expressed as [24]:

$$a'_c = 2a_c = 2 \left(\frac{2E^*}{H} \right)^{2/(D-1)} G^2, \quad (4)$$

where, $H = 2.8Y$ is the hardness of the softer material [25], Y is the yield strength of softer material. Asperities with $a' > a'_c$ are in the full elastic deformation regime, and the asperities are in plastic deformation if they satisfy $a' \leq a'_c$.

Based on Hertz contact theory, the deformation δ and the equivalent radius R for one micro-contact are determined by the W-M fractal function as [8]:

$$\delta = 2^{3-D} G^{(D-1)} (\ln \gamma)^{1/2} \pi^{(D-2)/2} (a')^{(2-D)/2}, \quad (5)$$

$$R = \frac{a'^{D/2}}{2^{4-D} \pi^{D/2} G^{D-1} (\ln \gamma)^{1/2}}. \quad (6)$$

For the cases of elastic or fully plastic asperity deformations, the relationship of contact force f and truncated area a' for one micro-contact can be given by [16].

$$f_e = \frac{4}{3} E^* R^2 \delta^3 = \frac{2^{9/2-D} E^*}{3} \pi^{(D-3)/2} (\ln \gamma)^{1/2} G^{(D-1)} a'^{(3-D)/2}, \quad (7)$$

$$f_p = H a', \quad (8)$$

where the subscripts e and p denote elastic and full plastic deformations, respectively. $E^* = \left(\frac{1-\nu_1^2}{E_1} + \frac{1-\nu_2^2}{E_2} \right)^{-1}$ is equivalent elastic modulus, E_1 , E_2 , ν_1 and ν_2 are the elastic modulus and Poisson ratios of two surfaces, respectively.

The total elastic force F_E , plastic force F_P , and real contact area A_r can be obtained by integrating the asperities over the contact surface.

$$F_E = \int_{a'_c}^{a'_L} f_e n(a') da' = \begin{cases} \frac{2^{(9-2D)/2} D}{3(3-2D) \pi^{(3-D)/2}} E^* (\ln \gamma)^{1/2} G^{(D-1)} \times \psi^{1-D/2} a_L^{D/2} \left(a'_L^{3-D} - a'_c^{3-D} \right) & (D \neq 1.5), \\ 2E^* \psi^{1/4} \pi^{3/4} (\ln \gamma)^{1/2} G^{1/2} a_L^{3/4} \ln \frac{a'_L}{a'_c} & (D = 1.5) \end{cases} \quad (9)$$

$$F_p = \int_0^{a'_c} f_p n(a') da' = \frac{HD\psi^{(2-D)/2}}{2-D} a_L^{D/2} a_c'^{(2-D)/2}, \quad (10)$$

$$A_r = \int_0^{a'_c} a' n(a') da' + \frac{1}{2} \int_{a'_c}^{a'_L} a' n(a') da' = \frac{D}{4-2D} \psi^{1-\frac{D}{2}} a_L^{D/2} (a_L^{1-D/2} + a_c'^{1-D/2}). \quad (11)$$

The total force F of contact surface is composed of the elastic and plastic force. Based on the definitions of pressure in the contact surface, the mean pressure of contact surface in the nominal area A_r can be written as:

$$\sigma_m = \frac{F_E + F_P}{A_0} = \begin{cases} \frac{2^{(9-2D)/2} DE^* (\ln \gamma)^{1/2} G^{(D-1)} \psi^{1-\frac{D}{2}} a_L^{\frac{D}{2}} \times}{3(3-2D) A_0 \pi^{(3-D)/2}} \times \\ \times \left(a_L^{\frac{3-D}{2}} - a_c'^{\frac{3-D}{2}} \right) + \frac{HD\psi^{\frac{(2-D)}{2}}}{(2-D) A_0} a_L^{D/2} a_c'^{\frac{(2-D)}{2}}, (D \neq 1.5) \\ \frac{2E^* \psi^{\frac{1}{4}} (\ln \gamma)^{\frac{1}{2}} G^{\frac{1}{2}} a_L^{\frac{3}{4}} \ln \left(\frac{a'_L}{a'_c} \right)}{\pi^{\frac{3}{4}} A_0} + \\ + \frac{2HD\psi^{\frac{1}{4}}}{A_0} a_L^{\frac{3}{4}} a_c'^{\frac{1}{4}}, (D = 1.5) \end{cases} \quad (12)$$

The normal contact stiffness k_n for each elastic micro-contact can be written as:

$$k_n = \frac{df_e}{d\delta} = \frac{df_e/da'}{d\delta/da'} = \frac{4E^*(3-D)}{3\sqrt{2\pi}(2-D)} a'^{\frac{1}{2}}. \quad (13)$$

Since all asperities are plastic deformations when $a' \leq a'_c$, the normal contact stiffness should take $k_n = 0$. The whole normal stiffness K_N of contact surface can be given as:

$$K_N = \int_{a'_c}^{a'_L} k_n n(a') da' = \frac{4E^*(3-D)D}{3\sqrt{2\pi}(1-D)(2-D)} \times \psi^{1-D/2} a_L^{D/2} (a_L^{(1-D)/2} - a_c'^{(1-D)/2}). \quad (14)$$

The asperities of contact surface are elastic or plastic deformations. The elastic energy is generated due to the effect of stiffness in the elastic deformation region, and the plastic energy is generated due to the effect of damping in the plastic deformation region. It is plastic deformation for micro-contact when $a' \leq a'_c$,

the plastic energy of one micro-contact is given by [21]:

$$w_{np} = \int_0^\delta f_p d\delta = Ha'\delta. \quad (15)$$

The plastic strain energy in plastic contact region can be obtained as:

$$W_{NP} = \int_0^{a'_c} w_{np} n(a') da' = \frac{2^{2-D} HDG^{D-1}}{2-D} \psi^{\frac{2-D}{2}} (\ln \gamma)^{\frac{1}{2}} \pi^{\frac{D-2}{2}} a_L^{\frac{D}{2}} a_c'^{2-D}. \quad (16)$$

When the truncated area a' of a micro-contact satisfies $a'_c < a' < a'_L$, the elastic energy of one micro-contact can be written as:

$$w_{ne} = \int_0^\delta f_e d\delta = \frac{8}{15} E^* R^{\frac{1}{2}} \delta^{\frac{5}{2}}. \quad (17)$$

The elastic energy of contact surface can be obtained by integrating Eq. (17), results in:

$$W_{NE} = \int_{a'_c}^{a'_L} w_{ne} n(a') da' = \frac{2^{\frac{17}{2}-2D} E^* DG^{2(D-1)} \psi^{1-\frac{D}{2}} \ln \gamma}{15(5-3D)\pi^{\frac{5-D}{2}}} (a_L^{\frac{5-2D}{2}} - a_c'^{\frac{D}{2}} a_c'^{\frac{5-3D}{2}}). \quad (18)$$

The normal contact damping dissipation factor can be obtained as [21]:

$$\frac{W_{NP}}{W_{NE}} = \frac{15(5-3D)H\pi^{\frac{3}{2}-D} a_c'^{2-D}}{2^{\frac{13}{2}-D} E^* G^{D-1} (2-D) (\ln \gamma)^{\frac{1}{2}} (a_L^{\frac{5-3D}{2}} - a_c'^{\frac{5-3D}{2}})}. \quad (19)$$

The normal damping of contact surface can be written as:

$$C_N = \eta_n \sqrt{MK_N} = \frac{15(5-3D)H\pi^{\frac{3}{2}-D} a_c'^{2-D}}{2^{\frac{13}{2}-D} E^* G^{D-1} (2-D) (\ln \gamma)^{\frac{1}{2}} (a_L^{\frac{5-3D}{2}} - a_c'^{\frac{5-3D}{2}})} \times \sqrt{M \frac{4E^*(3-D)D}{3\sqrt{2\pi}(1-D)(2-D)} \psi^{1-D/2} a_L^{D/2} (a_L^{(1-D)/2} - a_c'^{(1-D)/2})}, \quad (20)$$

where, M is the mass of the structure.

1.2 Tangential Stiffness and Damping Model

When the contact surface suffers tangential force under a certain normal force, the deformation of asperities on the surface will occur in the shear direction. According to [25], the tangential deformation of the single asperity can be given as:

$$\delta_t = \frac{3\mu p}{16G'r} \left[1 - \left(1 - \frac{t}{\mu p} \right)^{2/3} \right], \quad (21)$$

where p , t is the normal and tangential load of a single asperity respectively, G is the equivalent shear modulus of the contact surfaces, $1/G' = (2-\nu_1)/G_1 + (2-\nu_2)/G_2$, where G_1 , G_2 is he modulus of the two materials, respectively. μ is the static friction factor. r is the contact radius of one micro-contact.

For one micro-contact, the ratio of shear force and normal force satisfies $t/p = T/P$, T is the tangential force acting on the contact surface and described as $T = \tau_b A_r$, where τ_b is the shear strength of the softer material [26]. The tangential stiffness of one micro-contact can be expressed as $k_t = dt/d\delta_t$, then the total tangential stiffness can be written as follows:

$$\begin{aligned} K_T &= \int_{a_c}^{a_L} k_t n(a') da' = \\ &= \frac{8G'D\psi^{(2-D)/2}}{\sqrt{2\pi}(1-D)} \left(1 - \frac{T}{\mu P} \right)^{1/3} \times \\ &\times a_L^{D/2} (a_L^{(1-D)/2} - a_c^{(1-D)/2}). \end{aligned} \quad (22)$$

For one single micro-contact, a small relative motion will be caused when a tangential force is less than the limiting friction force, as depicted in [24]. The contact area of micro-contact can be divided into a “microslip” section and a “stick” section. The hysteretic damping of contact surface mainly depends on the microslip of asperities for the contact surface, which is the main reason for the energy dissipation of contact surface.

According to [24], the energy dissipation of one micro-contact per cycle in the vibration can be expressed as:

$$\begin{aligned} w_d &= \frac{9\pi^{1/2} a^{3/2} \mu^2 P^2}{10G'A_r^2} \times \\ &\times \left\{ 1 - \left(1 - \frac{T}{\mu P} \right)^{5/3} - \frac{5T}{6\mu P} \left(1 + \left(1 - \frac{T}{\mu P} \right)^{2/3} \right) \right\}. \end{aligned} \quad (23)$$

The energy dissipation of contact damping for the whole surface can be expressed as:

$$\begin{aligned} W_d &= \int_{a_c}^{a_L} w_d n(a') da' \\ &= \frac{9(2\pi)^{1/2} \mu^2 P^2 (4-2D)^2}{20G'\psi^{(2-D)/2} D(3-D) a_L^{D/2} (a_L^{(2-D)/2} + a_c^{(2-D)/2})^2} \times \\ &\left(a_L^{(3-D)/2} - a_c^{(3-D)/2} \right) \left\{ 1 - \left(1 - \frac{T}{\mu P} \right)^{5/3} - \frac{5T}{6\mu P} \left[1 + \left(1 - \frac{T}{\mu P} \right)^{2/3} \right] \right\}. \end{aligned} \quad (24)$$

The total energy input W is a combination of dissipation energy W_d and elastic strain energy W_e of the two contact surfaces. Then, the elastic strain energy of the two surfaces can be obtained by the difference of total energy storage and dissipation energy per cycle. The energy storage of one micro-contact w caused by the tangential force can be expressed as [27]:

$$w = 2\pi \frac{3\mu^2 a^2 P^2}{16A_r^2 G'r} \left[\frac{3}{5} + \frac{2}{5} \left(1 - \frac{T}{\mu P} \right)^{5/3} - \left(1 - \frac{T}{\mu P} \right)^{2/3} \right]. \quad (25)$$

The total energy input W per cycle for the contact surface due to tangential force can be obtained as:

$$\begin{aligned} W &= \int_{a_c}^{a_L} w n(a') da' \\ &= \frac{3\pi(2\pi)^{1/2} \mu^2 P^2 (4-2D)^2}{32G'\psi^{(2-D)/2} D(3-D) a_L^{D/2} (a_L^{(2-D)/2} + a_c^{(2-D)/2})^2} \times \\ &\left(a_L^{(3-D)/2} - a_c^{(3-D)/2} \right) \left[\frac{3}{5} + \frac{2}{5} \left(1 - \frac{T}{\mu P} \right)^{5/3} - \left(1 - \frac{T}{\mu P} \right)^{2/3} \right]. \end{aligned} \quad (26)$$

The elastic strain energy of two surfaces W_e can be written as:

$$W_e = W - W_d. \quad (27)$$

According to the definition of damping dissipation factor, it is the ratio of the dissipated energy to total elastic strain energy. The tangential contact damping dissipation factor can be expressed as:

$$\eta_t = \frac{W_d}{W_e}. \quad (28)$$

The tangential contact damping mainly depends on hysteretic damping, which is the result of energy dissipation in the contact surfaces. The total tangential contact damping can be written as [24]:

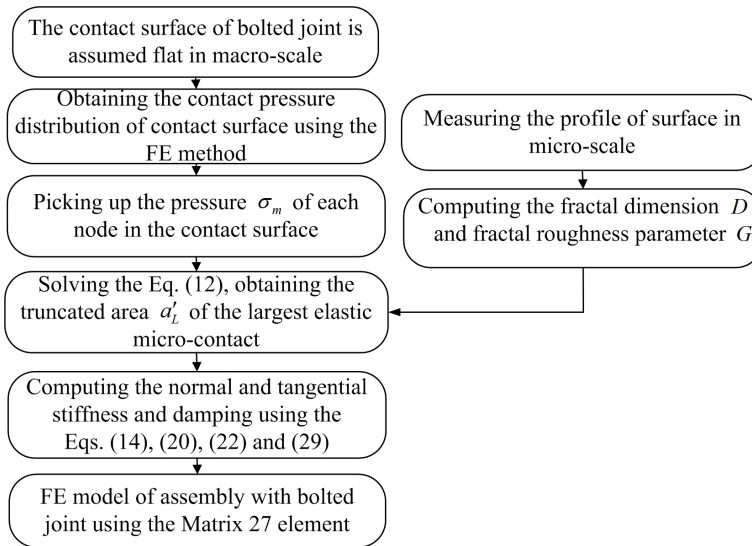


Fig. 2. Flowchart diagram for the stiffness and damping model of the bolted joint

$$C_T = \eta_t K_T = \frac{1}{(5\pi / 24)(H_2 / H_1) - 1} \times \frac{8G'D\psi^{(2-D)/2}}{\sqrt{2\pi}(1-D)} \left(1 - \frac{T}{\mu P}\right)^{1/3} a_L^{D/2} (a_L^{(1-D)/2} - a_c^{(1-D)/2}). \quad (29)$$

where, H_1, H_2 are two nonlinear functions of T and P , which can be expressed as:

$$H_1 = 1 - \left(1 - \frac{T}{\mu P}\right)^{5/3} - \frac{5T}{6\mu P} \left[1 + \left(1 - \frac{T}{\mu P}\right)^{2/3}\right],$$

$$H_2 = \frac{3}{5} + \frac{2}{5} \left(1 - \frac{T}{\mu P}\right)^{5/3} - \left(1 - \frac{T}{\mu P}\right)^{2/3}.$$

In this section, the local uniform pressure case is introduced to study the normal and tangential stiffness, damping of contact surfaces based on the fractal contact theory. However, the contact pressure of bolted joint is uneven distribution due to the effect of the concentrated force of multi-bolts. To obtain the contact pressure distribution of surface, the contact surface is assumed to be flat in macro-scale. Then, the nodes of the contact surface are selected, and the contact stress can be extracted from the general Postproc section of ANSYS software. Based on the nodal stress of contact surface, the largest truncated area a'_L can be calculated by using Eq. (12). The normal and tangential stiffness, damping of the contact surface can be obtained by using Eqs. (14), (20), (22) and (29) based on the obtained area a'_L . The

values of stiffness and damping are assigned to the MATRIX27 element, which is used to connect the node-to-node of two contact surfaces. Fig. 2 shows the flowchart diagram for the stiffness and damping model of the bolted joint.

2 EXPERIMENTAL SET-UP AND VALIDATION FOR THE BOLTED JOINT

In order to validate the presented model of the bolted joint, a box-shaped specimen is designed as shown in Fig. 3. The material of the specimen is nodular cast iron (material type QT600-3). The contact surfaces are machined by milling with roughness $R_a = 1.6 \mu\text{m}$. The material property of the specimen is listed in Table 1. A surface profilometer is used to measure the contact surface for obtaining the data of surface profile. The fractal dimension D and fractal roughness parameter G can be computed based on the power spectrum density method [17], the reticular cell counting method [28], the variation method [29], yardstick method [30] and structure-function method [31]. In this paper, the power spectrum density method is used to obtain the fractal dimension D and fractal roughness parameter G . The power spectral density $P(\omega)$ of W-M function can be calculated by the following equation as:

$$P(\omega) = \frac{G^{2(D-1)}}{2 \ln \gamma} \omega^{2D-5}, \quad (30)$$

where γ is the scaling parameter for determining the spectral density and self-affine property $\gamma = 1.5$, and ω is the spatial frequency. Taking the logarithm of Eq.

(30), the linearized equation can be obtained, and its slope k and intercept b can be given by:

$$k = 2D - 5, \quad b = 2(D - 1)\lg G - \lg(2 \ln \gamma), \quad (31)$$

The power spectrum density of a specimen surface and its linear fitting function can be obtained by adopting the least square method, as shown in Fig. 3. Based on the slope and intercept of the fitting function, the fractal dimension and fractal roughness parameter can be obtained as $D = 1.42$, $G = 1.21E-8$ m.

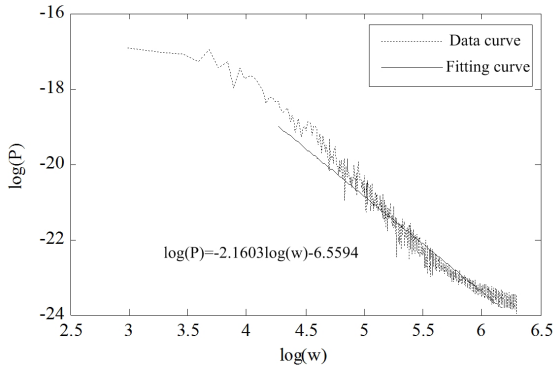


Fig. 3. Power spectrum density of a specimen surface

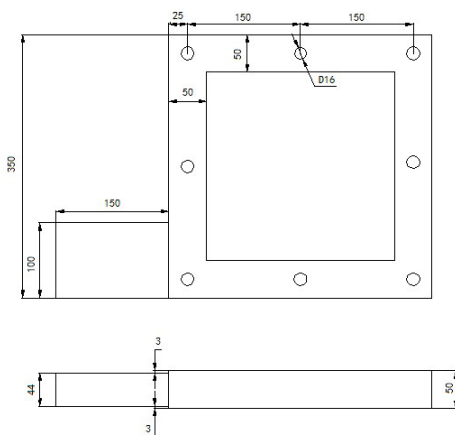


Fig. 4. Plane dimension of box-shaped specimen

The assembly is composed of two specimens and connected by eight M16 bolts. The material of bolts is 45# steel. The assembly is suspended to simulate the free degree of a freedom state, as shown in Fig. 5. Two group sensors are placed in two specimens, respectively. Each group consists of nine piezoelectric acceleration sensors. The sensor type is PCB Mode 330B30. An impact hammer is adopted for excitement. The signals of the impact hammer and the sensors are collected and analysed in an LMS modal analyser. In the experiment, the key problem is how to ensure an accurate pre-tightening force for each bolt. The errors

of the pre-tightening force will affect the contact status and dynamic characteristic of the bolted joint. It is difficult to obtain the accurate pre-tightening force only using the torque wrench, due to the effect of friction and the coupling effect of multi-bolts. Therefore, the pre-calibrated tension bolts are used to provide the accurate pre-tightening force.

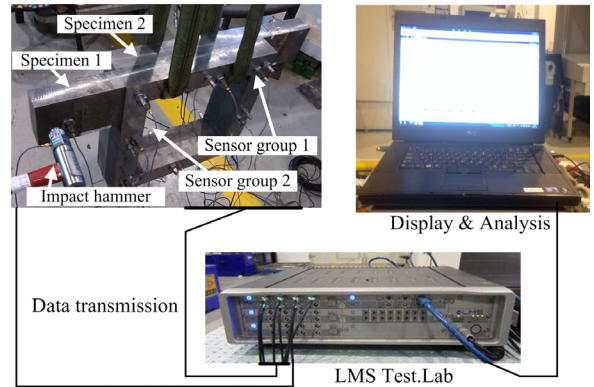


Fig. 5. Experimental set-up of bolted joint

Table 1. Material property of two specimens

Parameter name	Parameter value
Density ρ (kg/m ³)	7800
Elastic modulus E (Pa)	1.5E11
Poisson modulus	0.28
Hardness H (Pa)	1.96E9

In order to verify the presented stiffness and damping model based on the surface contact pressure, a finite element model for the assembly bolted joint is established in ANSYS as shown in Fig. 6. The contact pressure distribution of the bolted joint can be obtained based on the static analysis method. The pre-tightening force can be loaded in the ① to ⑧ for each bolt as shown in Fig. 6. The nodes of the contact surface are selected, and the contact pressure could be extracted from analysis results. Then, we can use the values of nodes pressure to compute the contact stiffness and damping in the normal and tangential directions as depicted in section 2. Fig. 7 shows the mesh of contact surface with 1019 nodes, and two surfaces have identical meshes so that the nodes are in one-to-one correspondence on two surfaces, which makes it possible to add the self-defined element between two nodes. Here, the MATRIX27 element of ANSYS software is introduced to define the normal and tangential stiffness, damping of bolted joint respectively. The MATRIX27 stiffness element for a pair of nodes could be expressed as follows,

$$\begin{bmatrix} K_{xx} & 0 & 0 & 0 & 0 & 0 & -K_{xx} & 0 & 0 & 0 & 0 & 0 \\ 0 & K_{yy} & 0 & 0 & 0 & 0 & 0 & -K_{yy} & 0 & 0 & 0 & 0 \\ 0 & 0 & K_{zz} & 0 & 0 & 0 & 0 & 0 & -K_{zz} & 0 & 0 & 0 \\ 0 & 0 & 0 & 0 & 0 & 0 & 0 & 0 & 0 & 0 & 0 & 0 \\ 0 & 0 & 0 & 0 & 0 & 0 & 0 & 0 & 0 & 0 & 0 & 0 \\ 0 & 0 & 0 & 0 & 0 & 0 & 0 & 0 & 0 & 0 & 0 & 0 \\ -K_{xx} & 0 & 0 & 0 & 0 & 0 & K_{xx} & 0 & 0 & 0 & 0 & 0 \\ 0 & -K_{yy} & 0 & 0 & 0 & 0 & 0 & K_{yy} & 0 & 0 & 0 & 0 \\ 0 & 0 & -K_{zz} & 0 & 0 & 0 & 0 & 0 & K_{zz} & 0 & 0 & 0 \\ 0 & 0 & 0 & 0 & 0 & 0 & 0 & 0 & 0 & 0 & 0 & 0 \\ 0 & 0 & 0 & 0 & 0 & 0 & 0 & 0 & 0 & 0 & 0 & 0 \\ 0 & 0 & 0 & 0 & 0 & 0 & 0 & 0 & 0 & 0 & 0 & 0 \end{bmatrix}$$

where K_{xx} , K_{yy} are the tangential stiffness along the contact surface, K_{zz} is the normal stiffness perpendicular to the contact surface. The MATRIX27 damping element has a similar expression.

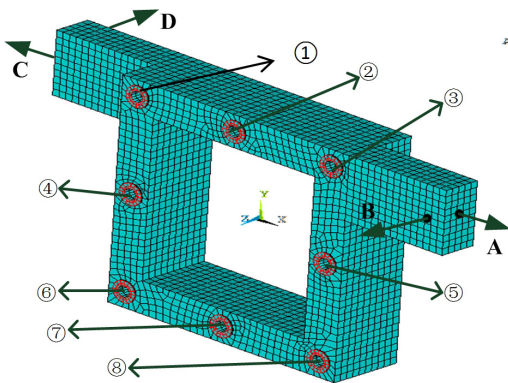


Fig. 6. FE model of assembly with bolted joint

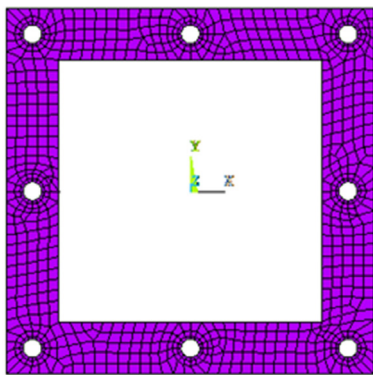


Fig. 7. Mesh of contact surface

3 RESULTS AND DISCUSSION

The dynamic characteristic of a bolted joint can be affected by the contact status of the surface. Usually, the initial status of a bolted joint is always different with its operating status. The main reason is that

the bolted parts of the machine tool are affected by the external loads. As a result, the contact status of bolted joint can be changed by those external loads. Therefore, two typical cases are introduced to verify the presented method in this paper: the bolted joint with the equal pre-tightening force for each bolt and the bolted joint with bending moment effect. Figs. 8 and 9 show the contact pressure distribution of bolted joint. The pressure of contact surface is an uneven symmetrical distribution for the case of equal pre-tightening force, as shown in Fig. 8. For example, the maximum pressure appears near the bolt hole with 7.98 MPa and the pressure gradually declines to 0.62 MPa in the middle of two bolt holes when the pre-tightening force of each bolt is 9 kN. Fig. 9 shows the pressure distribution of contact surface with bending moment effect. The bending moment acting on the assembly alters the stress of the contact surface. An equivalent model can be presented to represent the bending moment effect by adjusting the pre-tightening force of each bolt. For example, the pre-tightening force of bolts increase from F_b to F_b' for ① to ③ and decrease from F_b to F_b'' for ⑥ to ⑧, where F_b is the pre-tightening force without the effect of bending moment, F_b' and F_b'' are the pre-tightening force with the effect of bending moment, respectively. The

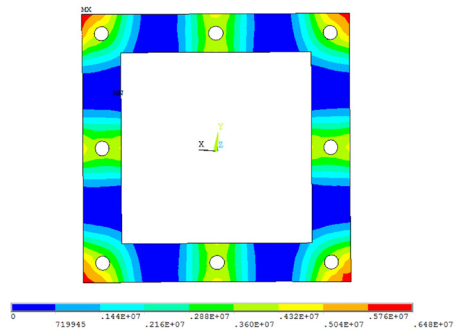


Fig. 8. Contact pressure distribution with the identical pre-tightening force for each bolt

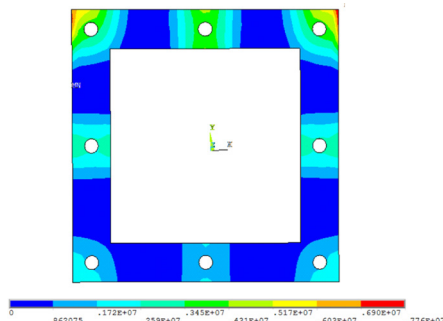


Fig. 9. Contact pressure distribution with bending moment effect

equivalent bending moment acting on the assembly can be written as $M=L_a/2(F_b'-F_b'')N_b$, where L_a is the distance between two-row bolts and $N_b=3$ is the number of bolts in each side of the assembly. The pressure distribution is more non-uniform, in which the pressure of one side of the contact surface is improved, and that of the other side is decreased. Compared with the pressure distribution of the contact surface with only an equal pre-tightening force effect for each bolt, the bending moment can significantly affect the pressure distribution of the contact surface.

The finite element model of assembly with bolted joint can be established by assigning the values of stiffness and damping between two surfaces based on the contact pressure. In order to verify the presented stiffness and damping model based on the surface contact pressure for the bolted joint, the frequency response analysis is necessary for the presented model. The hammer mode experiment is adopted to obtain the experimental mode. The points of A and B are chosen as the exciting point, and points C, and D points are chosen as the pick-up point in the normal and tangential directions, respectively. The tangential and normal displacements of bolted assembly can be obtained. The frequency responses in a normal and tangential directions at pre-tightening force 15 kN for each bolt are shown in Figs. 10 and 11. Comparing the predicted frequency response with the measured one, it is almost coincident in the frequency range.

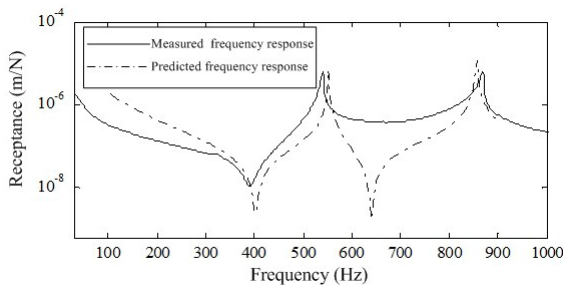


Fig. 10. Frequency response in normal direction

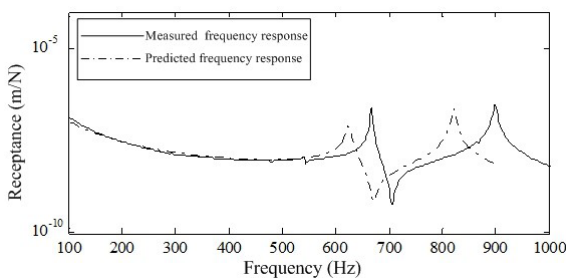


Fig. 11. Frequency response in tangential direction

Table 2 shows the numerical and experimental 1st to 6th order mode shapes. The experimental mode shapes are measured by a modal hammering impact testing method and the average results of three times for the existing test are adopted to reduce the random error and improve the signal-to-noise ratio. In order to ensure the same pre-tightening force for each bolt, the numerical constant torque wrench is used to adjust the pre-tightening force of bolts. The results show that the mode shapes from the introduced method have good agreement with those of the experiment. In order to verify the effect of uneven pressure distribution in the contact surface, the uniform pressure distribution case is introduced as depicted in [11]. The surface pressure for the uniform pressure distribution case can be obtained by the equation of $P_u = \sum_{n=1}^{N_u} P_n / A$, where, N_u is the number of bolts, P_n is the pre-tightening force for each bolt, A is the whole area of bolted joint.

The 1st to 6th order natural frequencies of structure can be obtained as shown in Table 3. For obtaining the accurate experimental results, the specimens are decomposed and assembled three times again in the experiment. Every time the maximum error of pre-tightening force is less than 0.1 kN for each bolt. Furthermore, comparing the natural frequencies of three experiments, the maximum error is 0.41%, which indicates good agreement for the bolted joint. In Table 3, the experimental natural frequency is the mean value of the natural frequency of three experiments. For the uniform pressure case with 9 kN pre-tightening force of each bolt, the errors of 1st to 6th order natural frequencies of assembly are 5.47%, -8.62%, -2.43%, -8.1%, -6.7% and 4.7%, respectively. Corresponding the errors of 1st to 6th order natural frequencies of assembly are 1.09%, -3.79%, 1.74%, -3.88%, -2.66% and 2.48% for the non-uniform pressure case. Comparing the natural frequency of the uniform pressure case, those of non-uniform pressure case are much closer to the experimental results. The results show that the uneven pressure distribution of contact surface can seriously affect the accuracy analysis of the bolted assembly. The contact stiffness and damping of the bolted joint can be changed by improving bolted pre-tightening force, which can enlarge the natural frequency of assembly. With the hammering test, the first order natural frequency is 526.03 Hz and 550.83 Hz for the pre-tightening force 9 kN and 15 kN of each bolt, respectively. The dynamic characteristic of the bolted assembly can be significantly improved with the increasing of the pre-tightening force.

When the bolted assembly is loaded by the bending moment, the contact pressure distribution is altered, as shown in Table 3. The pre-tightening force for each bolt is 15 kN, and the bending moment is $M = 4500 \text{ N}\cdot\text{m}$. An equivalent model is adopted to represent the bending moment effect by adjusting the pre-tightening force of each bolt. The pre-tightening forces of the bolts are 20 kN for ① to ③, 15 kN for ④ and ⑤ and 10 kN for ⑥ to ⑧, as shown in Fig. 6. In comparison with the case without a bending moment, the 1st to 6th order natural frequency are depressed, which shows that the contact stiffness of the bolted joint is weakened by the bending moment. The main reason is that the uneven distribution of contact pressure is intensified due to the effect of the bending moment. The results show that it is unable to reflect

the effect of bending moment and has much error for the uniform pressure case. However, it still maintains good consistency with the experimental results for the non-uniform stress case. The presented stiffness and damping method based on the contact surface pressure is more accurate in the modeling of the bolted joint, whether or not considering the influence of external load. The presented method can be used to accurately predict the behavior of the bolted assembly. It is also found that the first order natural frequency can be increased with the improvement of the pre-tightening force, as shown in Fig. 12. However, the first order natural frequency increases slowly when the pre-tightening force is larger than 24 kN. The main reason is that the contact pressure near the bolts can increase with the increasing of pre-tightening force;

Table 2. Comparison of theoretical and experimental mode shapes (total displacement)

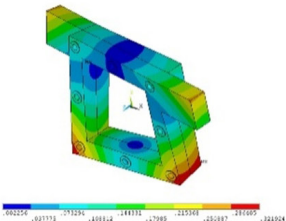
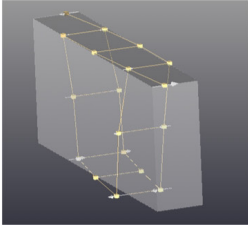
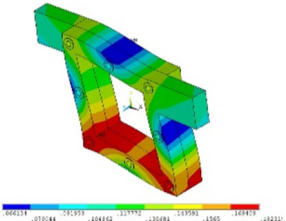
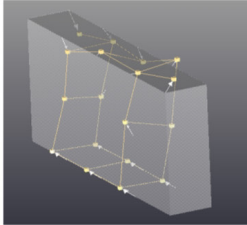
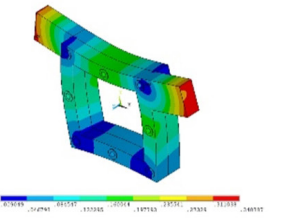
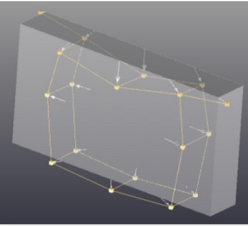
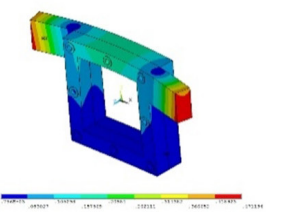
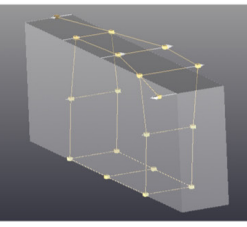
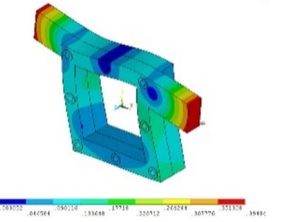
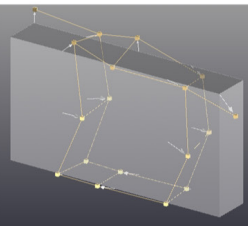
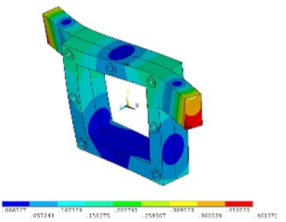
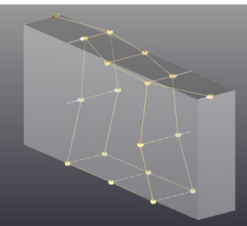
The model shape adopting presented method	The experimental modal shape	The model shape adopting presented method	The experimental modal shape
			
1 st order		2 nd order	
			
3 rd order		4 th order	
			
5 th order		6 th order	

Table 3. Comparison of natural frequency for experimental result, uniform and non-uniform pressure adopting the presented method

Pre-tightening force for each bolt		f_1	f_2	f_3	f_4	f_5	f_6
9 kN	Experimental results	526.03	666.09	820.16	897.98	1334.41	1373.73
	Uniform pressure case	556.5	613.21	840.12	830.64	1250.63	1441.49
	Error of uniform pressure case [%]	5.47	-8.62	2.43	-8.1	-6.7	4.7
	Non-uniform pressure case	531.74	640.83	834.67	863.05	1299.8	1408.7
	Error of non-uniform pressure case [%]	1.09	-3.79	1.74	-3.88	-2.66	2.48
15 kN	Experimental results	550.83	668.11	871.12	903.26	1390.67	1414.80
	Uniform pressure case	588.61	619.16	835.20	838.19	1263.35	1467.82
	Error of uniform pressure case [%]	6.42	-7.9	-4.3	-7.76	-10.07	3.6
	Non-uniform pressure case	555.26	641.8	854.63	872.8	1319.8	1407.5
	Error of non-uniform pressure case [%]	0.8	-3.94	-1.89	-3.37	-5.1	-0.52
15 kN (with bending moment effect $M = 4500 \text{ N}\cdot\text{m}$)	Experimental results	547.49	667.59	834.22	900.36	1355.13	1380.96
	Uniform pressure case	588.61	619.16	835.20	838.19	1263.35	1467.82
	Error of uniform pressure case [%]	6.98	-7.82	0.12	-7.42	-7.26	5.92
	Non-uniform pressure case	551.81	637.53	836.72	878.42	1308.1	1416.8
	Error of non-uniform pressure case [%]	0.78	-4.5	0.29	-2.44	-3.59	2.53

nevertheless, the contact stress far away from the bolts is almost invariant for the bolted joint.

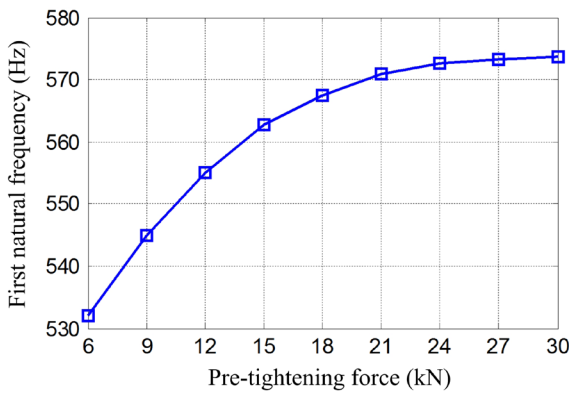


Fig. 12. Effect of pre-tightening force on the natural frequency of assembly

4 CONCLUSIONS

In this paper, a normal and tangential stiffness damping model based on the contact surface pressure is presented for the bolted joint. The relationship of stiffness, the damping bolted joint, and the contact surface pressure can be deduced. An experimental set-up with a box-shaped specimen is designed for validating the proposed model. The equal pre-tightening force and bending moment effect case studies are provided to demonstrate the effectiveness of the model. The maximum error of natural frequency for the uniform pressure case is twice that of non-uniform pressure cases. The stiffness of bolted joint is weakened as the pressure distribution is more uneven,

caused by the bending moment. The results show that the presented model is effective in the modeling of bolted joints whether having the influence of external load or not, which can meet the requirement of accurately predicting the behaviour of the bolted assembly for the machine tool.

5 ACKNOWLEDGEMENTS

This work was supported by Beijing Municipal Natural Science Foundation (CN) (No. 3132004), National Natural Science Foundation of China (No. 51375025) and National Science and Technology Major Project of China (No. 2013ZX04013-011).

6 NOMENCLATURES

- a real contact area of one micro-contact [m^2]
- A_0 nominal area [m^2]
- A_r total real contact area [m^2]
- C total normal damping
- D fractal dimension
- E equivalent elastic modulus [Pa]
- E_1, E_2 elastic modulus of two surfaces [Pa]
- f normal load of one micro-contact [N]
- F total normal load of contact surface [N]
- G fractal roughness parameter [m]
- G' equivalent shear modulus [Pa]
- G_1, G_2 shear modulus of two surfaces [Pa]
- H hardness of the soft material [MPa]
- k stiffness of one micro-contact [N/m]
- K total stiffness for contact surface [N/m]
- L sampling length, [m]

M mass of the structure [kg]
 n frequency index
 n_{\max} upper limit of frequency index
 p normal load of one micro-contact [N]
 P normal force of contact surface [N]
 r radius of the real contact region [m]
 R curvature radius [m]
 t tangential load of one micro-contact [N]
 T shear force of contact surface [N]
 w energy storage of one micro-contact [J]
 w_d dissipated energy of one micro-contact [J]
 W energy storage of contact surface [J]
 W_d dissipated energy of contact surface [J]
 x lateral distance [m]
 Y yield stress of the soft material [Pa]
 z height of machined surface [m]
 δ deformation of one micro-contact [m]
 γ scaling parameter of the spectral density
 η contact damping dissipation factor
 ν_1, ν_2 Poisson ratio
 μ static friction coefficient
 σ_m mean pressure of contact surface [Pa]
 τ_b shear strength of the soft material [Pa]
 ψ expand coefficient

Subscripts or superscripts:

$'$ truncated section of one micro-contact
 c critical parameter demarcating the elastic and plastic regimes
 e parameter of one micro-contact in the elastic regime
 E parameter of contact surface in the elastic regime
 L parameter for the largest asperity
 n normal parameter of one micro-contact
 N normal parameter of contact surface
 p parameter of one micro-contact in the plastic regime
 P parameter of contact surface in the plastic regime
 t tangential parameter of one micro-contact
 T tangential parameter of contact surface

8 REFERENCES

- [1] Mao, K.M., Li, B., Wu, J., Shao, X.Y. (2010). Stiffness influential factor-based dynamic modeling and its parameter identification method of fixed joints in machine tool. *International Journal of Machine Tools and Manufacture*, vol. 50, no. 2, p. 156-164, DOI:10.1016/j.ijmachtools.2009.10.017.
- [2] Mohd Tobi, A.L., Ding, J., Bandak, G., Leen, S.B., Shipway, P.H. (2009). A study on the interaction between fretting wear and cyclic plasticity for Ti-6Al-4V. *Wear*, vol. 267, no. 1-4, p. 270-282, DOI:10.1016/j.wear.2008.12.039.
- [3] Fridrici, V., Fouvry, S., Kapsa, Ph. (2003). Fretting wear behavior of a Cu-Ni-In plasma coating. *Surface and Coatings Technology*, vol. 163-164, p. 429-434, DOI:10.1016/S0257-8972(02)00639-4.
- [4] Kartal, M.E., Mulvihill, D.M., Nowell, D., Hills, D.A. (2011). Determination of the frictional properties of titanium and nickel alloys using the digital image correlation method. *Experimental Mechanics*, vol. 51, no. 3, p. 359-371. DOI:10.1007/s11340-010-9366-y.
- [5] Kartal, M.E., Mulvihill, D.M., Nowell, D., Hills, D.A. (2011). Measurements of pressure and area dependent tangential contact stiffness between rough surfaces using digital image correlation. *Tribology International*, vol. 44, no. 10, p. 1188-1198, DOI:10.1016/j.triboint.2011.05.025.
- [6] Filippi, S., Akay, A., Gola, M.M. (2004). Measurement of tangential contact hysteresis during microslip. *Journal of Tribology*, vol. 126, no. 3, p. 482-489, DOI:10.1115/1.1692030.
- [7] Mulvihill, D.M., Brunskill, H., Kartal, M.E., Dwyer-Joyce, R.S., Nowell, D. (2013). A comparison of contact stiffness measurements obtained by the digital image correlation and ultrasound techniques. *Experimental Mechanics*, vol. 53, no. 7, p. 1245-1263, DOI:10.1007/s11340-013-9718-5.
- [8] Kashani, H., Nobari, A.S. (2010). Identification of dynamic characteristics of nonlinear joint based on the optimum equivalent linear frequency response function. *Journal of Sound and Vibration*, vol. 329, no. 9, p. 1460-1479, DOI:10.1016/j.jsv.2009.11.007.
- [9] Čelič, D., Boltežar, M. (2009). The influence of the coordinate reduction on the identification of the joint dynamic properties. *Mechanical Systems and Signal Processing*, vol. 23, no. 4, p. 1260-1271, DOI:10.1016/j.ymsp.2008.11.002.
- [10] Wang, L.Y., Yin, G.G., Zhang, J.F. (2006). Joint identification of plant rational models and noise distribution function using binary-valued observation. *Automatica*, vol. 42, no. 4, p. 535-547, DOI:10.1016/j.automatica.2005.12.004.
- [11] Shi, X., Polycarpou, A.A. (2005). Measurement and modeling of normal contact stiffness and contact damping at the meso scale. *Journal of Vibration and Acoustics*, vol. 127, no.1, p. 52-60, DOI:10.1115/1.1857920.
- [12] Ciulli, E., Ferreira, L.A., Pugliese, G., Tavares, S.M.O. (2008). Rough contacts between actual engineering surfaces: Part I. Simple models for roughness description. *Wear*, vol. 264, no. 11-12, p. 1105-1115, DOI:10.1016/j.wear.2007.08.024.
- [13] Komvopoulos, K., Ye, N. (2000). Three-dimensional contact analysis of elastic-plastic layered media with fractal surface topographies. *Journal of tribology*, vol.123, no.1, p.632-640, DOI:10.1115/1.1327583.
- [14] Majumdar, A., Bhushan, B. (1990). Role of fractal geometry in roughness characterization and contact mechanics of surfaces. *Journal of Tribology*, vol. 112, no. 2, p. 205-216, DOI:10.1115/1.2920243.
- [15] Majumdar, A., Bhushan, B. (1991). Fractal model of elastic-plastic contact between rough surfaces. *Journal of Tribology*, vol. 113, no. 1, p. 1-11, DOI:10.1115/1.2920588.
- [16] Zhang, X.L., Huang, Y.M., Han, Y. (2000). Fractal model of the normal contact stiffness of machine joint surfaces based on the fractal contact theory. *China Mechanical Engineering*, vol. 11, no. 7, p. 727-729. (in Chinese)

- [17] Jiang, S.Y., Zheng, Y., Zhu, H. (2009). A contact stiffness model of machined plane joint based on fractal theory. *Journal of Tribology*, vol. 132, no. 1, p. 1-6, DOI:10.1115/1.4000305.
- [18] Shi, J.P., Ma, K., Liu, Z.Q. (2012). Normal contact stiffness on unit area of a mechanical joint surface considering perfectly elastic elliptical asperities. *Journal of Tribology*, vol. 134, no. 3, p. 1-6, DOI:10.1115/1.4006924.
- [19] Sherif, H.A., Kossa, S.S. (1991). Relationship between normal and tangential contact stiffness of nominally flat surfaces. *Wear*, vol. 151, no. 1, p. 49-62, DOI:10.1016/0043-1648(91)90345-U.
- [20] Fuadi, Z., Takagi, T., Miki, H., Adachi, K. (2013). An experimental method for tangential contact stiffness evaluation of contact interfaces with controlled contact asperities. *Proceedings of the Institution of Mechanical Engineers, Part J: Journal of Engineering Tribology*, vol. 227, no. 10, p. 1117-1128, DOI:10.1177/1350650113481293.
- [21] Zhang, X.L., Ding, H.Q. (2013). Normal contact damping and dissipation factor model of joint interfaces based on fractal theory. *Chinese Transactions of the Chinese Society for Agricultural Machinery*, vol. 44, no. 6, p. 287-294, DOI:10.6041/j.issn.1000-1298.2013.06.050.
- [22] Bograd, S., Schmidt, A., Gaul, L. (2008). Joint damping prediction by thin layer elements. *Proceedings of the IMAC 26th*. Society of Experimental Mechanics Inc. Bethel.
- [23] Li, X.P., Wang, W., Zhao M.Q., Nie, H.F., Wen, B.C. (2012). Fractal prediction model for tangential contact damping of joint surface considering friction factors and its simulation. *Journal of Mechanical Engineering*, vol. 23, no. 12, p. 46-50, DOI:10.3901/jme.2012.23.046. (in Chinese)
- [24] Zhang, X.L., Wang, N.S., Lan, G.S., Wen, S.H., Chen, Y.H. (2013). Tangential damping and its dissipation factor models of joint interfaces based on fractal theory with simulations. *Journal of Tribology*, vol. 136, no. 1, p. 1-10, DOI:10.1115/1.4025548.
- [25] Kogut, L., Etsion, I. (2002). Elastic-plastic contact analysis of a sphere and a rigid flat. *Journal of Applied Mechanics*, vol. 69, no. 5, p. 657-662, DOI:10.1115/1.1490373.
- [26] Johnson, K.L. (1985). *Contact Mechanics*. Cambridge University Press, Cambridge, DOI:10.1017/CB09781139171731.
- [27] Tian, H.L., Zhao, C.H., Fang, Z.F. Zhu, D.L., Li, X., Mao, K.M. (2013). Improved model of tangential stiffness for joint interface using anisotropic fractal theory. *Transactions of the Chinese Society for Agricultural Machinery*, vol. 44, no. 3, p. 257-266, DOI:10.6041/j.issn.1000-1298.2013.03.046.
- [28] Goerke, D., Willner, K. (2008). Normal contact of fractal surfaces—Experimental and numerical investigations. *Wear*, vol. 264, no. 7, p. 589-598, DOI:10.1016/j.wear.2007.05.004.
- [29] Boneh, Y., Sagy, A., Reches, Z. (2013). Frictional strength and wear-rate of carbonate faults during high-velocity, steady-state sliding. *Earth and Planetary Science Letters*, vol. 381, p. 127-137, DOI:10.1016/j.epsl.2013.08.050.
- [30] Ai, T., Zhang, R., Zhou, H.W., Pei, J.L. (2014). Box-counting methods to directly estimate the fractal dimension of a rock surface. *Applied Surface Science*, vol. 314, p. 610-621, DOI:10.1016/j.apsusc.2014.06.152.
- [31] Wang, T., Wang, L., Zheng, D., Zhao, X., Gu, L. (2015). Numerical simulation method of rough surfaces based on random switching system. *Journal of Tribology*, vol. 137, no. 2, p. 021403, DOI:10.1115/1.4029644.

Dynamic Simulation of Wind Turbine Planetary Gear Systems with Gearbox Body Flexibility

Xiangyang Xu^{1,2*} – Youchuan Tao³ – Changrong Liao² – Shaojiang Dong¹ – Renxiang Chen¹

¹ Chongqing Jiaotong University, School of Mechatronics and Vehicle Engineering, China

² Chongqing University, College of Optoelectronic Engineering, China

³ CSIC(Chongqing) Haizhuang Windpower Equipment Co., China

Gearbox body flexibility has a great influence on the dynamic response and load sharing among the planetary gears. In this paper, through investigating the coupling boundary conditions between planetary gears transmission subsystem and the gearbox body subsystem, a new dynamic model that integrates gearbox body flexible supporting stiffness is developed to simulate the effects of gearbox body flexibility on the dynamic response and the dynamic load sharing. The numerical results demonstrate that the dynamic transmission error and the dynamic mesh force are obviously lower in the system with the gearbox body flexibility than without it. Furthermore, peak position also gradually moves towards to the lower frequency when gearbox body flexibility is included. In addition, the dynamic loading factor tends to be decreased when gearbox body flexibility is taken into account, which is also verified by experiments conducted on a planetary gear test rig.

Keywords: wind turbine gearbox, planetary gears system, gearbox body flexibility, coupled dynamic model, dynamic characteristic, load sharing

Highlights

- An approach to building a dynamic model of a planetary transmission system including gearbox body flexibility.
- Dynamic response of planetary transmission system including gearbox body flexibility is investigated.
- Effects of gearbox body flexibility on load sharing are analysed.
- Load sharing is verified by experiments.

0 INTRODUCTION

The planetary gear system has many advantages such as the large transmission ratio, the compact structure, and good power split ability, which are widely applied in a wind turbine. Most of the previous studies of planetary gear transmission system assumed that the gearbox body is rigid. This is a supportable assumption for the light load planetary gear transmission system whose gear body deformation can be neglected. However, in the case of a heavy load, such as in a wind turbine, gearbox body flexibility can cause large deviations of calculation results. Therefore, it has great practical significance to establish the relationship between gearbox body flexibility and dynamic characteristics.

The dynamic characteristics of wind turbine planetary gearboxes have been studied recently. August et al. [1] developed a methodology including time-varying mesh stiffness and time mesh phasing for the static and dynamic load analysis of planetary gear trains. Kahraman [2] used three-dimensional models to examine the dynamic response of both time-invariant and time-varying representations. Parker et al. [3] used a semi-analytical finite element model to study the comprehensive dynamic response results of planetary gear system under a range of

operating speeds and torques. Peeters et al. [4] and [5] investigated the natural frequencies and dynamic responses of the planetary gearbox with the finite element method. Montestruc [6] studied the effects of Hicks type flexible planetary gear pin on the load sharing by using a finite element model, and also compared it with the straddle-type carrier. Gu and Velez [7] and [8] developed a lumped parameters model to study the effects of planet gear position error and eccentricity errors on dynamic behaviours of planetary gear systems. Wang et al. [9] applied a mixed flexible-rigid multi-body model to investigate dynamic behaviours of the transmission system of a wind turbine. Zhu et al. [10] and [11] studied the dynamic characteristics of planetary gear system of a wind turbine. Feng et al. [12] and Teng et al. [13] conducted fault diagnosis for a wind turbine planetary gear system through demodulation analysis. Ambarisha and Parker [14] examined the gear tooth contact loss in a planetary gear system and validated these results by comparing them with a finite element model. Guo [15] studied complex nonlinear effects with tooth wedging, bearing clearance and its correlation with planet bearing forces. Chen et al. [16] establish a gear mesh stiffness model included the ring deformation based on the Timoshenko beam theory to calculate the mesh stiffness of ring gear and planet

gear mesh. These studies provide valuable guidance for the optimum design of wind turbine gearboxes, but the gearbox body flexibility is still not included. Meanwhile, due to the complicated gearbox body structures and multi-floating components, it is also difficult to reflect the dynamic characteristics of the planetary gear transmission system when gearbox body flexibility is included.

In this paper, a new dynamic model of planetary gear the includes the gearbox body flexibility is established. Here, the gearbox body flexibility is obtained via the finite element method. Then the flexibility is integrated into the lumped parameters dynamic model to simulate the effects of gearbox body flexibility on dynamic characteristics and load sharing.

1 COUPLING DYNAMIC MODEL

A wind turbine planetary gearbox consists of internal planetary gear transmission subsystem and gearbox body subsystem.

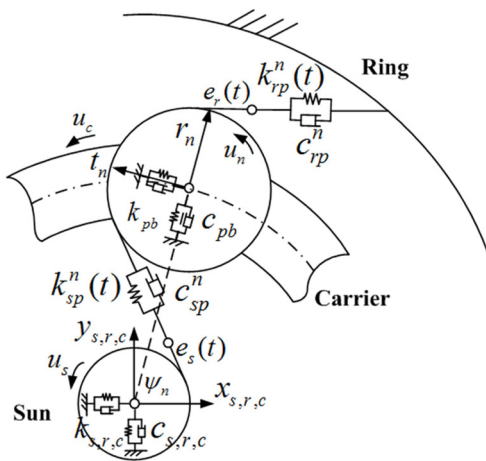


Fig. 1. Lumped parameters dynamic model of the planetary gear transmission subsystem

To demonstrate the effects of gearbox body flexibility on the dynamic characteristics, a four planet gear wind turbine gearbox is employed in this study. The dynamic model of internal planetary gear transmission subsystem is based on the lumped-parameter method as shown in Fig. 1. The planetary gear transmission subsystem includes sun (s), carrier (c), ring (r) and the n^{th} planet gear ($P_n, n = 1, 2, 3, 4$). The input component is carrier c , while the output component is sun gear s . The rotational motion of the ring gear is constrained. In the dynamic model, each central element has vibration amplitudes in

the one rotation degree of freedom $u_i (i = r, c, s)$ and two translation degrees of freedom $x_i, y_i (i = r, c, s)$. Moreover, the n^{th} planet gear u_n (rotational), t_n (tangential), $r_n (n = 1, 2, 3, 4)$ (radial) are defined in a rotating carrier reference frame which is fixed to the carrier with the origin at point O. The supporting bearings and gear mesh along the line of action are modelled by linear springs. Here, unloaded static transmission errors $e_s(t)$ and $e_r(t)$ are involved as representing $s-P_n$ mesh and $r-P_n$ mesh. Mesh damping and bearing damping are captured by using modal damping method. The main parameters of the planetary gear set are listed in Table 1.

Table 1. Main parameters of the planetary gear set

	Ring	Planet	Sun	Carrier
Teeth number	95	37	21	-
Modulus [mm]	15	15	15	-
Teeth width [mm]	335	315	335	-
Mass [kg]	1478	301	205	1526
I/R2 [kg]	1456	328	199	1744
Pressure angle [deg]	25	25	25	-
Bearing stiffness [N/m]	1.0×10^{10}	2.1×10^8	1.3×10^6	9.9×10^9
Torsional stiffness [N/m]	5.0×10^{10}	0	0	0

The dynamic transmission error of the gear pairs $s-P_n$ and $r-P_n$ along the line of action expressed as DTE_{sp}^n and DTE_{rp}^n , respectively, can be determined as:

$$\begin{aligned}
 DTE_{sp}^n &= y_s \cos \psi_{sn} - x_s \sin \psi_{sn} - r_n \sin \alpha_{sn} \\
 &\quad - t_n \cos \alpha_{sn} + u_s + u_n + e_s(t), \\
 DTE_{rp}^n &= y_r \cos \psi_{rn} - x_r \sin \psi_{rn} + r_n \sin \alpha_{rn} \\
 &\quad - t_n \cos \alpha_{rn} + u_r - u_n + e_r(t).
 \end{aligned}
 \tag{1}$$

where, α_{sn} and α_{rn} are the meshing angles of the gear pairs $s-P_n$ and $r-P_n$, respectively; ψ_{sn} and ψ_{rn} are the projected angles of the sun gear and the ring on the coordinate of the planets, and $\psi_{sn} = \psi_n - \alpha_{sn}$, $\psi_{rn} = \psi_n - \alpha_{rn}$; $e_s(t)$, $e_r(t)$ are the static transmission error of the gear pairs $s-P_n$ and $r-P_n$, respectively.

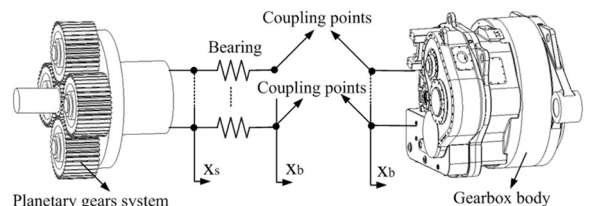


Fig. 2. The coupling method between the transmission system and gearbox body flexibility

The internal planetary gear transmission subsystem and the gearbox body subsystem are coupled through mass-less supporting springs, as shown in Fig. 2. In the coupling model, take X_s , X_b and X_h as the displacements vector of the planetary gears transmission subsystem, the springs and the gearbox body subsystem, then the coupling equations between massless supporting springs and the gear transmissions is as follows:

$$T + F(t) = M_s \ddot{X}_s + (C_s + \Omega_c G) \dot{X}_s + (K_b + K_m(t) - \Omega_c^2 K_\omega) X_s + K_{sb} X_b, \quad (2a)$$

$$F_b = M_b \ddot{X}_b + K'_{sb} X_s + (K_b + K_b) X_b, \quad (2b)$$

where, M_s , M_b are the discrete mass matrix of the transmission subsystem and the springs, respectively, K_b is the stiffness matrix of the springs, $K_m(t)$ is the matrix of the mesh stiffness of the transmission system, K_{sb} is the coupling stiffness matrix between the springs and the transmission sub-systems, C_s is the damping matrix of the transmission subsystem; G and K_ω are the gyroscopic matrix and the centripetal stiffness matrix, respectively; Ω_c is the angular speed of carrier; T is the vector of the external torques, $F(t)$ is the excitations due to the static transmission errors and time-varying mesh stiffness, F_b is the force vector applied on the spring.

The coupling equations between massless supporting springs and the gearbox body is as follows:

$$-F_b = M_b \ddot{X}_b + (K_b + K_b) X_b + K_{bh} X_h, \quad (3a)$$

$$F_h = M_h \ddot{X}_h + K_{bh} X_b + K_h X_h, \quad (3b)$$

where M_h is the discrete mass matrix of the body subsystem, respectively, K_{bh} is the coupling stiffness matrix between the bearings and the body of the gearbox, K_h is the matrix of the stiffnesses of the discrete body system, F_h is the force vector applied on the gearbox body, and here $F_h = 0$.

Next, the motion equations of the whole system can be obtained through Eqs. (2) and (3) as follows:

$$\begin{bmatrix} T + F(t) \\ 0 \\ 0 \end{bmatrix} = \begin{bmatrix} M_s & 0 & 0 \\ 0 & M_b & 0 \\ 0 & 0 & M_h \end{bmatrix} \begin{bmatrix} \ddot{X}_s \\ \ddot{X}_b \\ \ddot{X}_h \end{bmatrix} + \begin{bmatrix} C_s + \Omega_c G & 0 & 0 \\ 0 & 0 & 0 \\ 0 & 0 & 0 \end{bmatrix} \begin{bmatrix} \dot{X}_s \\ \dot{X}_b \\ \dot{X}_h \end{bmatrix} + \begin{bmatrix} K_b + K_m(t) - \Omega_c^2 K_\omega & K_{sb} & 0 \\ K'_{sb} & K_b + K_b & K_{bh} \\ 0 & K'_{bh} & K_h \end{bmatrix} \begin{bmatrix} X_s \\ X_b \\ X_h \end{bmatrix}, \quad (4)$$

Eq. (4) represents the general form of a coupling gears-bearings-body gearbox system, in which the supporting stiffness and the inertia of the body are included. Here, If the inertia of the body of the gearbox is neglected, i.e., $M_h \ddot{X}_h = 0$, only gearbox body flexibility needs to be considered. Based on the third line and the second line of the Eq. (4),

$X_h = -K_h^{-1} K_{bh} X_b$ and $X_b = -[K_b + K_b - K_{bh} K_h^{-1} K'_{bh}]^{-1} K'_{sb} X_s$. Then, the first line of the Eq. (4) can be read:

$$T + F(t) = M_s \ddot{X}_s + C_s \dot{X}_s + \Omega_c G \dot{X}_s + (K_b + K_m - K_{sb} (K_b + K_b - K_{bh} K_h^{-1} K'_{bh})^{-1} K'_{sb} - \Omega_c^2 K_\omega) X_s. \quad (5)$$

Thus, it is very difficult to directly obtain K_h and K_{bh} , but the matrix $K_f = K_b - K_{bh} K_h^{-1} K'_{bh}$ can be easily obtained. If a unit load $F_{unit} = 1$ is applied on each coupling point of the gearbox body in one direction, the reverse matrix of K_f is defined as $A_h^j(k)$. Here, $A_h^j(k)$ is the displacement of the k th degree of freedom when the unity force is applied on the j th coupling point. The assembled influential coefficient matrix of the body K_f reads:

$$K_f = [(A_h^j(k))']^{-1}. \quad (6)$$

Similarly, to obtain the coupling stiffness of bearing-planetary gear system K_{sb} , a unit load $F_{unit} = 1$ is applied on each coupling point of the planetary gear transmission system in one direction. The rotational direction stiffness of bearing is zero. Thus, K_{sb} can be calculated in the other five degrees of freedom by Eq. (7).

$$K_{sb}^j = [F_{unit} = 1] [A_{sb}^j(k)]^{-1}, \quad (7)$$

where, A_{sb}^k is the displacement of gear transmission subsystem along one degree of freedom when the unity force is applied on the coupling points.

Taking the damping, the external forces, and the excitations of the system into account, the completed dynamic equations can be read:

$$T + F(t) = M_s \ddot{X}_s + C_s \dot{X}_s + \Omega_c G \dot{X}_s + (K_b + K_m - (A_{sb}^j(k))^{-1} \times (K_b + ((A_h^j(k))')^{-1} ((A_{sb}^j(k))^{-1})' - \Omega_c^2 K_\omega) X_s, \quad (8a)$$

$$X_s = (x_i, y_i, u_i, t_n, r_n, u_n)^T \quad (i = r, c, s; n = 1, 2, 3, 4). \quad (8b)$$

Here, the floating support of the sun gear is simulated as low-stiffness springs. The system excitations come from the time-varying mesh stiffness and the static transmission errors. The mesh phasing relationships of the s - P_n - r meshes are taken into consideration in this dynamic model. These functions

of meshing stiffness and planet phasing can be obtained from the previous work [7] and [8].

The dynamic mesh forces of $F_{sp}^n(t)$ ($s-P_n$ mesh) and $F_{rp}^n(t)$ ($r-P_n$ mesh) are obtained from Eqs. (1) and (8), as follows:

$$F_{sp}^n(t) = k_{sp}^n(t)DTE_{sp}^n(t) + c_{sp}^n \dot{DTE}_{sp}^n(t), \quad (9a)$$

$$F_{rp}^n(t) = k_{rn}^n(t)DTE_{rn}^n(t) + c_{rp}^n \dot{DTE}_{rn}^n(t). \quad (9b)$$

Then load sharing factor is defined to represent the dynamic load sharing among the planets, and can use the following expressions:

$$L_{s(r)p}^n(t) = 4F_{s(r)p}^n(t) / \sum_{n=1}^4 F_{s(r)p}^n(t). \quad (10)$$

2 EFFECTS OF GEARBOX BODY FLEXIBILITY ON DYNAMIC RESPONSE

The mesh frequency varies from 0 Hz to 3000 Hz to show the dynamic mesh forces responses of the planetary gear system with the excitations due to the mesh stiffness and the transmission error. Figs. 3 and 4 show the dynamic transmission error and dynamic mesh force of the $s-P_n$ gear pair and the $r-P_n$ gear pair with and without the gearbox body, respectively. Here, the input load of the carrier is taken as $9.33 \times 10^5 \text{ Nm}$.

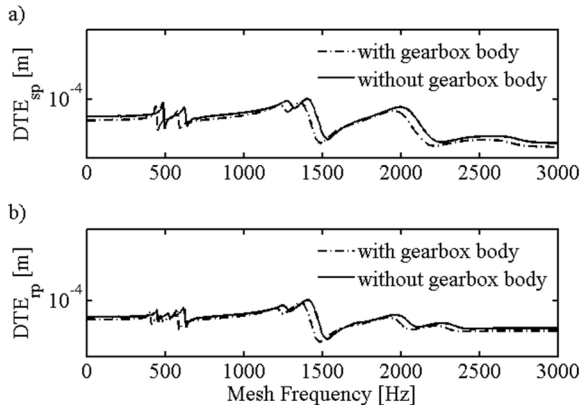


Fig. 3. Dynamic transmission error with or without gearbox body flexibility; a) s-P mesh; b) r-P mesh

It can be seen in Figs. 3 and 4 that when the gearbox body is included in the dynamic model, the peaks of a dynamic transmission error and dynamic mesh force decrease both in the S-P gear mesh and the R-P gear mesh. The frequencies of response peaks clearly move to lower mesh frequencies. At peak 1284 Hz, 1411 Hz and 2096 Hz, the variations are remarkable. Therefore, from the point of view of

improving system vibration, a lower gearbox body supporting stiffness can decrease the peak of dynamic mesh force of s-P mesh and r-P mesh, which will alleviate the vibration conditions of the system.

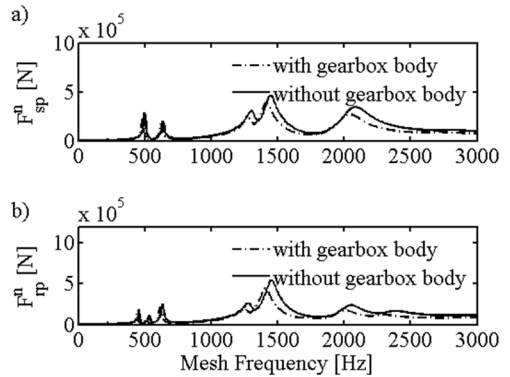


Fig. 4. Dynamic mesh force for the with or without gearbox body flexibility; a) s-P mesh; b) r-P mesh

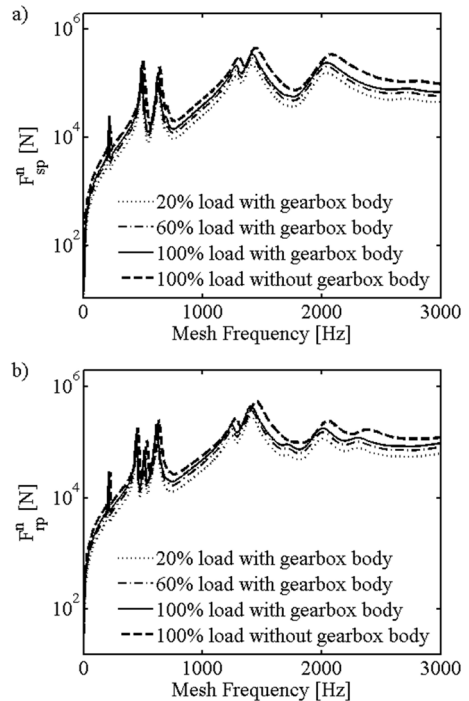


Fig. 5. Dynamic mesh force for the different input load; a) s-P mesh; b) r-P mesh

Due to the planetary gears system's existing multi-flexible components, the dynamic responses of planetary gears system with gearbox body flexibility are very different when an external load is changed. To observe these effects, 20 %, 60 %, and 100 % of the rated input load are applied to the coupling model with or without gearbox body flexibility, respectively. Then dynamic responses of s-P and r-P mesh can be

obtained in these cases, as shown in Fig. 5. It can be seen that, when gearbox body flexibility is included, the peak values of dynamic mesh force for the s-P gear pair and the r-P gear pair increase with the increase of input. It means that the heavier load can cause the higher system vibration, but the peak frequencies' position remain unchanged.

To observe the effects of gearbox body flexibility on the floating displacement of the sun gear, the maximum floating displacements of sun gear can be obtained by Eq. (8) with the same parameters, as shown in Fig. 6.

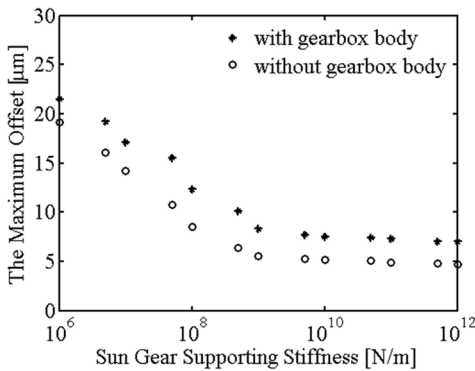


Fig. 6. The effects of sun gear supporting stiffness on floating displacements

From the Fig. 6, it can be seen that floating displacements of sun gear increase when gearbox body flexibility is coupled. Meanwhile, the floating displacement of the sun gear also decreases with the increase of the sun gear supporting stiffness. When the support stiffness of the sun gear is greater than 10¹⁰ N/m, there is almost no effect of the supporting stiffness of sun gear on the floating displacement amount.

3 EFFECTS OF GEARBOX BODY FLEXIBILITY ON LOAD SHARING

To observe the effects of gearbox body flexibility on load sharing among planet gears, assume planetary gear P1 has tangential position error $e_1 = 500 \mu\text{m}$. The dynamic load factor that represents good or bad load sharing is defined as the actual dynamic load to the mean input load of every planet gear, as shown in Fig. 7.

From the Figs. 7a and b, it can be seen that the dynamic loads are very close between planet gears P1 and P3 in the opposite phase, P2 and P4 are also similar characteristics. When gearbox body flexibility is included, the maximum load of P1 can drop from

30.1 % to 27.8 %. This means that gearbox body flexibility reduces the supporting stiffness of the gear-bearing system, which can play an important role in improving the load sharing of the planetary gear system.

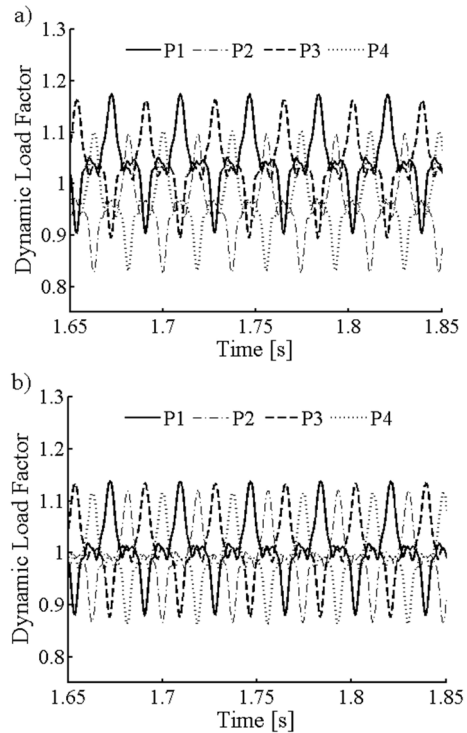


Fig. 7. Dynamic load factor with or without gearbox body flexibility; a) without gearbox body; b) with gearbox body

To verify load sharing results from the theoretical model, the experiments are conducted on a 3.7-megawatt power recirculation type back-to-back layout wind turbine gearbox test rig. The test system consists of 350 Ω strain gauge, dynamic strain indicator, and computer. Strain gauges are symmetrically arranged into four groups $u=1,2,3,4$ in the circumferential direction of the ring gear. Eight strains of each group $v = a, b, c, d, e, f, g, h$ are uniformly arranged on the two adjacent teeth, as shown in Fig. 8.

ϵ_{uv} represents each measuring point microstrain value, and load sharing coefficient of each measuring point can be read as Eq. (11).

$$L_{factor} = \frac{\epsilon_{uv}}{\frac{1}{4} \sum_{j=1}^4 \epsilon_{jv}} \tag{11}$$

Here, tangential error e_l of planetary gear P1 is still taken as 500 μm while input load is still taken as $9.25 \times 10^3 \text{ Nm}$. After the continuous running 300 hours,

mesh marking of the ring gear and microstrain curve in the same tooth root of ring gear can be observed in Figs. 9a and b.

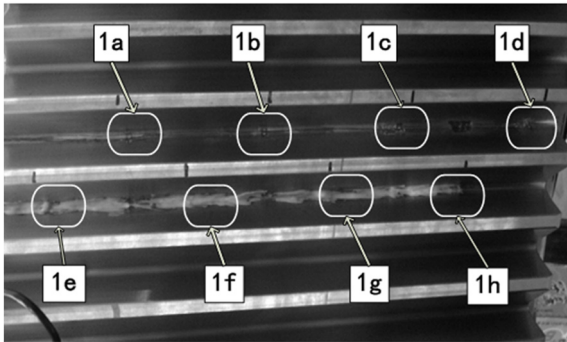


Fig. 8. Strain gauges' configuration along the tooth width

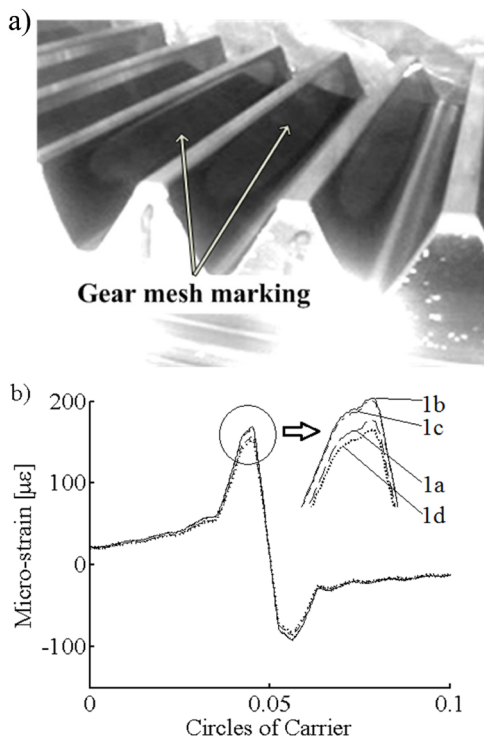


Fig. 9. Mesh marking microstrain of ring, a) Mesh marking; b) Microstrain curve at the same root

It can be seen from Fig. 9a that the distribution of mesh gear marking is drum shaped. It means that load sharing is good, and planet gear pins have no tilt. Fig. 9b shows that the four stress values of each ring teeth root are very close, which agrees well with the mesh gear marking.

Fig. 10 shows the continuous microstrain curve when four planet gears are sequential through the same root position. Moreover, the load-sharing

coefficient L_{factor} is 1.13, which means the maximum load of planet gear is 28.3 % of total input load. This result is in good agreement with the theoretical results in Fig. 7.

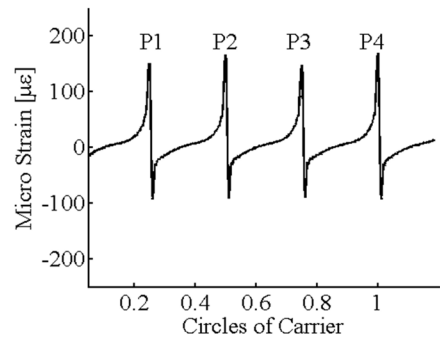


Fig. 10. Time-varying microstrain curve of the same position

4 CONCLUSIONS

In this work, a new coupled dynamic model between internal planetary gear transmission subsystem and external gearbox body flexibility is presented to study the dynamic response and load sharing. The flexible supporting stiffness of the gearbox body is incorporated in the dynamic model, and the effects of gearbox body flexibility on dynamic response and load sharing are simulated. The calculated results show that gearbox body supporting stiffness can significantly reduce the peak values of a dynamic transmission error and dynamic mesh force, and drop the peak frequencies of dynamic mesh force. The peak values of dynamic response increase with the increase of external load, but the frequencies positions of peaks are not changed. The sun gear floating displacements can be increased when gearbox body flexibility is taken into account. In addition, the planetary gear system has better load sharing after gearbox body flexibility is included. Load-sharing experiments are also conducted which verified the theoretical results.

5 ACKNOWLEDGEMENTS

The authors would like to thank Project Nos. 51405048 and 51405047 supported by the National Natural Science Foundation of China, Project Nos. 2016M590861 supported by the China Postdoctoral Science Foundation, Project Nos. Xm2015011 supported by the Special Program of Chongqing Postdoctoral Science Foundation, Project Nos. cstc2015jcyjA70012 and Nos.cstc2014jcyjA70009 supported by the Chongqing Research Program of

Frontier and Application Foundation, Project Nos. KJ1500516 supported by the Scientific Research Fund of Chongqing Municipal Education Commission, Project Nos. 310825161104 supported by the National Engineering Laboratory for Highway Maintenance Equipment, and Program of Study Abroad for Young Scholar sponsored by CQJTU for their support of this research.

6 REFERENCES

- [1] August, R. Kasuba, J.L. Frater, Pintz, A. (1984). *Dynamics of Planetary Gear Trains*. NASA Contractor Report 3793, Nasa, Washington.
- [2] Kahraman, A. (1994). Planetary Gear Train Dynamics. *ASME Journal of Mechanical Design*, vol. 116, no. 3, p. 713-720, DOI:10.1115/1.2919441.
- [3] Parker, R.G., Agashe, V., Vijayakar, S.M. (2000). Dynamic Response of a Planetary Gear System Using a Finite Element/Contact Mechanics Model. *ASME Journal of Mechanical Design*, vol. 122, no. 3, p. 304-310, DOI:10.1115/1.1286189.
- [4] Peeters, J.L.M., Vandepitte, D., Sas, P. (2006). Analysis of internal drive train dynamics in a wind turbine. *Wind Energy*, vol. 9, no. 1-2, p. 141-161, DOI:10.1002/we.173.
- [5] Peeters, J., Goris, S., Vanhollebeke, F., Marrant, B., Meeusen, W. (2008). A need for advanced and validated multibody models as a basis for more accurate dynamic load prediction in multi-megawatt wind turbine gearboxes. *International Conference on Noise and Vibration Engineering*, p. 2097-2112.
- [6] Montestruc, A.N. (2011). Influence of planet pin stiffness on load sharing in planetary gear drives. *ASME Journal of Mechanical Design*, vol. 133, no. 1, DOI:10.1115/1.4002971.
- [7] Gu, X., P. Velez, P. (2012). A dynamic model to study the influence of planet position errors in planetary gears. *Journal of Sound and Vibration*, vol. 331, no. 20, p. 4554-4574, DOI:10.1016/j.jsv.2012.05.007.
- [8] Gu, X., Velez, P. (2013). On the dynamic simulation of eccentricity errors in planetary gears. *Mechanism and Machine Theory*, vol. 61, p. 14-29, DOI:10.1016/j.mechmachtheory.2012.10.003.
- [9] Wang, J., Qin, D., Ding, Y. (2009). Dynamic behavior of wind turbine by a mixed flexible-rigid multi-body model. *Journal of System Design and Dynamics*, vol. 3, no. 3, p. 403-419, DOI:10.1299/jsdd.3.403.
- [10] Zhu, C.C., Xu, X.Y., Lim, T.C., Du, X.S., Mingyong Liu, M.Y. (2013). Effect of flexible pin on the dynamic behaviors of wind turbine planetary gear drives. *Proceedings of the Institution of Mechanical Engineers, Part C: Journal of Mechanical Engineering Science*, vol. 227, no. 1, p. 74-86, DOI:10.1177/0954406212447029.
- [11] Zhu, C.C., Xu, X.Y., Liu, H.J., Luo, T.H., Zhai, H.F. (2014). Research on dynamic characteristics of wind turbine gearboxes with flexible pins. *Renewable Energy*, vol. 68, p. 724-732, DOI:10.1016/j.renene.2014.02.047.
- [12] Feng, Z.P., Liang, M., Zhang, Y. Hou, S.M. (2012). Fault diagnosis for wind turbine planetary gearboxes via demodulation analysis based on ensemble empirical mode decomposition and energy separation. *Renewable Energy*, vol. 47, p. 112-126, DOI:10.1016/j.renene.2012.04.019.
- [13] Teng, W., Wang, F., Zhang, K.L., Liu, Y.B., Ding, X. (2014). Pitting fault detection of a wind turbine gearbox using empirical mode decomposition. *Strojniški vestnik - Journal of Mechanical Engineering*, vol. 60, no. 1, p. 12-20, DOI:10.5545/sv-jme.2013.1295.
- [14] Ambarisha, V.K., Parker, R.G. (2007). Nonlinear dynamics of planetary gears using analytical and finite element models. *Journal of Sound and Vibration*, vol. 302, no. 3, p. 577-595, DOI:10.1016/j.jsv.2006.11.028.
- [15] Guo, Y. (2011). *Analytical Study On Compound Planetary Gear Dynamics*. PhD. thesis, The Ohio State University, Ohio.
- [16] Chen, Z.G., Shao, Y.M., Daizhong Su, D.Z. (2013). Dynamic simulation of planetary gear set with flexible spur ring gear. *Journal of Sound and Vibration*, vol. 332, no. 26, p. 7191-7204, DOI:10.1016/j.jsv.2013.07.026.

Comprehensive Energy Resource Management for Essential Reduction of the Total Cost

Liljana Ferbar Tratar*

University of Ljubljana, Faculty of Economics, Slovenia

Comprehensive energy resource management presents a kind of global optimisation, which is much more cost-effective than separate treatment of energy-demand forecasting and energy-inventory data. In this paper, a two-stage supply chain is presented where the distributor of derivate energy products (e.g., hot water, steam, electricity) shares information with its supplier of primary energy sources (e.g., coal, crude oil, gas). Different methods of energy-demand forecasting can be used, although exponential smoothing methods are most often used in practice because they are simple, fast and inexpensive. In this study we analysed a modified Holt-Winters (HW) method and we describe a method for simultaneous optimisation of a forecasting method and a stock control policy. We compared the proposed joint optimisation of total cost with the optimisation, based solely on forecasting data. The total cost presents the joint cost of the distributor and supplier. The data consisted of 756 quarterly real series from M3-Competition and 300 simulated demand patterns. We have shown that the total cost can be reduced dramatically if we use joint optimisation instead of a separate treatment of a forecasting method and an inventory model. We obtained the best result with the modified HW method; the essential reduction of total cost was reached in the case of simulated data as well as in the case of real data.

Keywords: energy resource management, supply chain, forecasting, inventory, M3-competition, total cost

Highlights

- Comprehensive energy resource management is presented.
- Two-stage centralised supply chain of distributor and supplier is observed.
- The joint optimisation comprises energy-demand forecasting methods and energy-inventory data.
- The result shows an essential reduction of the total cost as an objective function.

0 INTRODUCTION

Sustainable energy supply, reducing dependence on energy resources, efficient energy production, climate-friendly and less energy-consuming production are some of the most important challenges facing the European Union in present times [1]. The European commission encourages energy companies to follow suggested climate action, which comprises cost-efficient and less environmental damaging power generation [2] and [3]. Companies have to look constantly for new strategies and tools to improve processes, decrease cost and increase productivity and efficiency [4] and [5]. The appropriate demand forecasting methods, inventory data and sharing of information constitute comprehensive energy resource management, which may lead to essential reduction of the total cost, better planning performance with energy resources and much more efficient production.

Customer demand is probably one of the most important factors to be predicted through a forecasting system that is especially problematic when we are faced with a noisy demand. Selecting a forecasting method from the many available is a very complex task (see, for example, [6] and [7]). The main approach towards the selection and optimisation of

alternative methods relates to the minimisation of forecast error measures. Most of the stock control studies consider demand data as an input to the model without explicitly considering that they are the results of a demand forecasting system. Even though this weakness has been highlighted in the academic literature, little empirical work has been conducted to develop an understanding of the interaction between forecasting and stock control, except in [8] and [9], where the problem of the local optimisation of forecasting methods was elucidated. In general, separate evaluation of the forecasting method and the stock control policy may easily lead to poorer overall performances [10].

We present an example of a centralized supply chain with an order-up-to inventory policy and evaluate different forecasting methods together with the inventory model. In this joint model we optimise total inventory costs where holding and stock-out costs (for different penalties) are included. We demonstrate that smoothing and initial parameters of forecasting methods can be determined to minimise the total costs. The joint model can be implemented easily, even by using an Excel spreadsheet, and the proposed solution is easy-to-use for managers.

*Corr. Author's Address: University of Ljubljana, Faculty of Economics, Kardeljeva ploščad 17, 1000 Ljubljana, Slovenia, liljana.ferbar.tratar@ef.uni-lj.si

Exponential smoothing methods are a class of methods that produce forecasts with simple formulae, taking into account the trend and seasonal effects of the data [11]. Distinguished by their simplicity, their forecasts are comparable to those of more complex statistical time series models [12]. The main advantages of HW methods, a special subset of exponential methods, are low expenses, fast calculations and simplicity.

The aim of this paper is to present a modified HW method, which is computationally stable and can handle both additive and multiplicative seasonality, even when a time series contains a nonlinear trend and a large noise component. We also expose the problem of the local optimisation of forecasting methods. We show that in the case of a centralised supply chain the calculated forecasts of demand, determined by minimising the mean square error (MSE), are not optimal. We therefore propose a method for the simultaneous optimisation of demand forecasting and a stock control policy, and demonstrate that initial and smoothing parameters in the forecasting methods can be determined to minimise the total costs of the supply chain.

The idea of the joint optimization could be used for different objective functions such as the total energy efficiency and environmental impact concerns [13].

The remainder of the paper is organised as follows. In Section 1, the methodology and data are described. In Section 2 we present forecasting methods; the additive, multiplicative and modified HW method. In Section 3 we describe our model of the supply chain and calculate average costs for all different forecasts considered as an input to the model. In Section 4, we describe the proposed joint optimisation of total costs and present the results, which allows us to compare different forecasting methods and replenishment policy combinations. Finally, after the conclusions of our paper some further steps of research are suggested.

1 DATA AND METHODOLOGY

We used real seasonal time series from the M3-Competition and conducted a simulation study to evaluate the performance of the modified HW method. The analyses were carried out in the program R [14]. The function `sbplx` from the nonlinear optimization package “`nloptr`” [15] was used to estimate the smoothing parameters. The starting values in the minimization step were set to $\alpha_0 = \beta_0 = \gamma_0 = 0.5$ and the maximum number of iterations was set to 25,000.

1.1 Real Time Series from the M3-Competition

The Makridakis Competitions, known in the literature as the M-Competitions, are empirical studies that have compared the performance of large number of major time series methods using recognized experts who provide forecasts for their method of expertise [12]. The first M-Competition (1982) used 1001 time series and 15 forecasting methods. The second M2-Competition (1993) used only 29 time series. The third M3-Competition (2000) was intended to both replicate and extend the features of the first two competitions. A total of 3003 time series were used. The data sets used refer mainly to business and economic time series, although the conclusions can be relevant to other disciplines as well. The original time series data can be found in the R package `Mcomp` [16].

In our study, we have analyzed quarterly series. They refer to five different disciplines, as shown in Table 1.

First we used the “`ets`” function from the R package `forecast` [17] and [18] to classify the series by the form of their trend, seasonality and noise. Table 1 also shows this classification, where ‘A’ stands for ‘additive’, ‘M’ for ‘multiplicative’, and ‘N’ for ‘none’.

We applied different forecasting methods to each of the series independently of its discipline and `ets` classification.

Table 1. Classification of quarterly time series from the M3-Competition

Discipline		Noise	Trend	Season	
Micro	204	A	N	N	67
Industry	83	A	N	A	40
Macro	336	A	A	N	113
Finance	76	A	A	A	64
Demographic	57	M	N	N	90
Total	756	M	N	A	31
		M	N	M	37
		M	A	N	87
		M	A	A	49
		M	A	M	42
M	M	N	76		
M	M	M	60		
Total					756

1.2 Simulated Time Series

We have simulated 300 time series corresponding to six different demand patterns using the following formula (based on [19]):

$$D_t = base + slope \times t^2 \times A + season \times s_{ind_{t-12}} \times t \times B + noise \times snormal() \times t \times C, \quad (1)$$

where D_t is the demand in time t , *base* is the average demand, *slope* captures trend in data (series with no trend are obtained by setting $slope = 0$), *season* is a seasonal factor, *noise* is the coefficient of demand variation, and *snormal()* is a standard normal random number generator. s_{ind_t} are seasonal indices, which are obtained for $t=1, 2, \dots, 12$ with *snormal()*. By varying the quantities A , B and C we obtain time series differing in the form of their trend, seasonality and noise. The possible demand patterns are the following. If we make A equal to 1, the equation provides a nonlinear (quadratic) trend; otherwise, if we make A equal to $1/t$, we get a pattern with a linear trend. If we make B equal to $1/t$, we get a demand pattern with additive seasonality; otherwise, if B is equal to 1, we get a pattern with multiplicative seasonality. The expression in the last term of the equation provides additive or multiplicative noise if we make C equal to $1/t$ or 1, respectively. Using the different combinations of parameters (*base*, *slope*, *season*, *noise*) we can generate the demand patterns.

Table 2. Descriptions and marks for different demand patterns

Description	Mark	noise (step)	slope	season
add. noise,	AAM_5_50	200-650 (50)	5	50
nonlinear trend,	AAM_5_100	200-650 (50)	5	100
mult. seasonality	AAM_8_100	200-650 (50)	8	100
mult. noise,	MAM_5_50	10-55 (5)	5	50
nonlinear trend,	MAM_5_100	10-55 (5)	5	100
mult. seasonality	MAM_20_50	10-55 (5)	20	50

In this study we analysed in detail only demand patterns with additive and multiplicative noise, additive nonlinear trend and multiplicative seasonality. *Base* was selected to ensure that the average demand was approximately 2000 units; the parameters for six demand patterns are shown in Table 2. We used notation *noise (step)* to point out that for each selected parameter *slope* and *season* we chose 10 different noises (e. g., for the AAM_5_50, $noise=200, 250, \dots, 650$). The AAM produced a demand with additive noise, additive nonlinear trend and multiplicative seasonality (quantity C is equal to $1/t$, A and B are equal to 1); the MAM produced a demand with multiplicative noise, nonlinear trend and multiplicative seasonality (quantities A , B and C are equal to 1). Each combination of the simulation study was replicated five times (for different *snormal()*). Thus, the total number of simulation runs for the

experiment is equal to 6 (patterns) \times 10 (different noises) \times 5 (simulations) = 300.

1.3 Symmetric Relative Efficiency Measure

The efficiency of the modified HW (MoHW) method was measured in terms of the MSE of the in-sample one-step-ahead forecasts and compared to that of additive (AHW) and multiplicative (MHW) methods. Because the first two complete seasons were used to initialize the methods, these observations were excluded from the reported MSE:

$$MSE = \frac{1}{T - 2s} \sum_{t=2s}^{T-1} (F_{t+1} - Y_{t+1})^2, \quad (2)$$

where Y_t is the actual value at the time point t , F_t is the forecasted value at the time point t , s is the length of seasonality and T is the length of the observed time series. To compare the MoHW method with the other method, we first find their mean square errors, MSE_{MoHW} and MSE_{method} as defined above. We define the symmetric relative efficiency measure as

$$SREM_{\frac{MoHW}{method}} = \begin{cases} 1 - \frac{MSE_{MoHW}}{MSE_{method}}; & MSE_{MoHW} < MSE_{method} \\ \frac{MSE_{method}}{MSE_{MoHW}} - 1; & MSE_{MoHW} \geq MSE_{method} \end{cases} \quad (3)$$

We prefer the SREM to the standard relative efficiency measure the REM (percentage increase or decrease of the MSE),

$$REM_{\frac{MoHW}{method}} = \frac{MSE_{MoHW} - MSE_{method}}{MSE_{method}}, \quad (4)$$

because it treats the methods symmetrically: e.g., when $MSE_{MoHW}=10$ and $MSE_{AHW}=20$, the REM is -50% , while when the $MSE_{MoHW}=20$ and the $MSE_{AHW}=10$, it is 100% . On the other hand the SREM is 50% in the first case and -50% in the second case, indicating that ‘on average’, none of the methods is preferable. The value of the SREM is bounded by the interval $[-1, 1]$, which mitigates the possibility of an individual time series to substantially outweigh other series in the group. The interpretation does not depend on the number of series in the group, so the SREM can easily be applied to the M3-Competition data where different disciplines (or types) have different numbers of time series.

Also, we use the definition of the SREM to compare the MoHW method with other methods

regarding average costs AC (in these cases, the SREMI measures the percentage increase or decrease of the average costs):

$$SREMI_{\frac{MoHW}{method}} = \begin{cases} 1 - \frac{AC_{MoHW}}{AC_{method}}; & AC_{MoHW} < AC_{method} \\ \frac{AC_{method}}{AC_{MoHW}} - 1; & AC_{MoHW} \geq AC_{method} \end{cases} \quad (5)$$

2 FORECASTING METHODS

The Holt-Winters method estimates three smoothing parameters associated with level, trend and seasonal factors. The seasonal variation can be of either an additive or multiplicative form. The multiplicative version is used more widely and on average works better than the additive one ([20]; of course, if a data series contains some values equal to zero, the multiplicative HW method cannot be used).

In the multiplicative seasonal form of the HW method (MHW) fundamental equations for level L_t , trend b_t , seasonal factors S_t and forecast F_t are:

$$L_t = \alpha(Y_t / S_{t-s}) + (1 - \alpha)(L_{t-1} + b_{t-1}), \quad (6)$$

$$b_t = \beta(L_t - L_{t-1}) + (1 - \beta)b_{t-1}, \quad (7)$$

$$S_t = \gamma(Y_t / L_t) + (1 - \gamma)S_{t-s}, \quad (8)$$

$$F_{t+m} = (L_t + b_t m) S_{t-s+m}, \quad (9)$$

where α, β, γ are smoothing parameters (which must lie in the interval $[0, 1]$), m is the number of the forecast ahead, s is the length of seasonality (e.g., the number of months or quarters in a year) and Y_t is the observed data at the time point t . We have given values for s, m and $Y_t, t = 1, 2, \dots, T$. To initialize the level, we set $L_s = (Y_1 + Y_2 + \dots + Y_s) / s$; to initialize the trend, we use $b_s = (Y_{s+1} - Y_1 + Y_{s+2} - Y_2 + \dots + Y_{2s} - Y_s) / s^2$; and for the initial seasonal indices we calculate $S_p = Y_p / L_s, p = 1, 2, \dots, s$.

The additive seasonal form of the HW method (AHW) works with the following equations:

$$L_t = \alpha(Y_t - S_{t-s}) + (1 - \alpha)(L_{t-1} + b_{t-1}), \quad (10)$$

$$b_t = \beta(L_t - L_{t-1}) + (1 - \beta)b_{t-1}, \quad (11)$$

$$S_t = \gamma(Y_t - L_t) + (1 - \gamma)S_{t-s}, \quad (12)$$

$$F_{t+m} = L_t + b_t m + S_{t-s+m}. \quad (13)$$

Eq. (11) is identical to (7). The only differences in the other equations are that the seasonal indices

are now added and subtracted instead of relying on products and ratios. The initial values for level and trend are identical to those for the multiplicative method. To initialize the seasonal indices we calculate $S_p = Y_p - L_s, p = 1, 2, \dots, s$.

The only difference between the AHW and the MoHW method is in the equation for seasonal factors:

$$S_t = \gamma(Y_t - L_t) + (1 - \alpha\gamma)S_{t-s}, \quad (14)$$

and forecast:

$$F_{t+m} = L_t + b_t m + \alpha S_{t-s+m}. \quad (15)$$

The other equations for MoHW conform to the AHW format. Thus, when we minimize the MSE with respect to the smoothing parameters, the new effect is to smooth the seasonal factors by changing them less. The initial values for the level, trend and seasonal components are the same as in the case of the AHW method.

For each of the series we also used the ‘ets’ function [17] and [18] to obtain the MSE, where we set opt.crit='mse', ic='aic', bounds='usual', so that the MSE was minimized to estimate the parameters of each model; the aic was used to select the best model, and the standard parameter restrictions were applied. We use the notation ETS method. It is a state space model that includes some transition equations that describe how the unobserved components or states (level, trend, seasonal) change over time. The classical decomposition method splits a time series into a trend and a seasonal component and projects them into the forecast horizon [21].

3 THE SUPPLY CHAIN COST MODEL

Consider a simple two-stage supply chain consisting of one distributor of derivate energy products (e.g., hot water, steam, electricity) and one supplier of primary energy sources (e.g., coal, crude oil, gas). The distributor holds an inventory in order to meet an external demand and places inventory replenishment orders to the supplier. At the time t , the last known value of the external demand is D_{t-1} . The distributor places an order Q_t to the supplier. We assume that the order placed one period ago is received (delivery lead time is one period). After the order placement, the external demand D_t is observed and filled. At the end of each period, the inventory costs are evaluated. The unsatisfied demand is backlogged and causes penalty costs for the distributor. The supplier is able to supply any requested quantity.

We assume that the distributor follows an order-up inventory policy. An order Q_t placed by the distributor to the supplier can be expressed as $Q_t = F_{t+1} - FS_t$, where F_{t+1} is the forecasted demand for a time point $t+1$ and FS_t is the final stock for the time point t (if $FS_t > 0$ the distributor has on-hand inventory, if $FS_t < 0$ the unsatisfied demand occurs). When it is $Q_t < 0$, an order is not placed. The final stock is calculated as $FS_t = IS_t - D_t$, where the initial stock is obtained as $IS_t = Q_{t-1} - FS_{t-1}$.

As the supplier has information about the external demand (the centralized supply chain), it places the order, which is equal to the forecasted demand (less FS_t , if $FS_t > 0$). The missing amount of products supplied from the marketplace (assuming that a perfect substitute for the product exists) causes penalty costs for the supplier.

The costs of the supply chain are the sum of the holding costs and the penalty costs for all links in the supply chain. We assume the penalty costs to be higher than the holding costs, which is expressed by introducing a weight, *penalty*, that is greater than 1. In our analysis, for all calculations of total costs (average costs and minimised average costs) we assume that the penalty is equal to 3 or 5.

In other words, using the common notation $X^+ = \max(X, 0)$, the supply chain costs C_t at the time

point t are expressed as (l is an individual link in the supply chain [in our case, $l = 1, 2$], n is the total number of links in the supply chain [$n = 2$]):

$$C_t = \sum_{l=1}^n C_t^l = \sum_{l=1}^n \left((IS_t^l - D_t^l)^+ + \text{penalty} \cdot (D_t^l - IS_t^l)^+ \right). \quad (16)$$

Because the first two seasons were used to initialize the methods, the average costs (AC) are calculated as:

$$AC = \frac{1}{T - 2s} \sum_{t=2s+1}^T C_t. \quad (17)$$

3.1 Real Time Series from the M3-Competitor

For each observed method and series, the symmetric relative efficiency measures (the SREM and the SREM1) of the MoHW with respect to the AHW, MHW or ETS were computed. Also, the portion of time series for which the MoHW method outperforms each other method was recorded.

Table 3 shows averages of the SREM for quarterly time series. We can observe that with the MoHW method the MSE can be reduced on average by more

Table 3. Averages of the SREM and the SREM1 for time series from the M3-Competition; the series are grouped by disciplines or types

MSE → COST	SREM (MSE) [%]			SREM1 (AC) [%]						
	MOHW/ AHW	MOHW/ MHW	MOHW/ ETS	penalty = 3			penalty = 5			
				MOHW/ AHW	MOHW/ MHW	MOHW/ ETS	MOHW/ AHW	MOHW/ MHW	MOHW/ ETS	
Discipline	MICRO	7.30	3.73	13.29	2.76	1.33	9.11	2.64	1.30	9.69
	MACRO	3.56	3.57	10.43	1.72	1.80	8.47	1.77	1.88	8.81
	INDUSTRY	1.94	-2.92	6.82	0.93	-0.34	3.99	1.07	-0.22	3.84
	FINANCE	0.42	0.24	10.38	0.57	0.74	3.74	0.74	0.89	2.91
	DEMOGRAPHIC	-3.74	-3.24	1.07	-4.09	-3.37	-0.19	-4.55	-3.86	-0.72
Type	ANN	0.21	1.27	14.65	-0.02	-0.33	10.54	-0.27	-0.54	10.99
	ANA	1.55	5.33	9.30	0.45	2.87	11.83	0.40	2.85	13.18
	AAN	-1.96	-0.27	6.67	-2.07	-1.05	5.77	-2.39	-1.32	6.23
	AAA	10.63	14.39	20.63	3.82	4.86	11.47	3.99	4.96	11.19
	MNN	1.33	-0.52	16.11	0.97	0.21	9.31	0.91	0.20	9.27
	MNA	-0.56	-0.14	16.89	-0.36	0.23	6.91	-0.31	0.26	5.73
	MNM	3.68	-4.83	8.84	0.63	-1.21	11.17	0.58	-1.07	12.18
	MAN	-2.00	-2.27	4.18	-2.56	-2.04	1.57	-2.79	-2.31	1.17
	MAA	3.56	7.83	4.62	0.10	4.84	3.86	-0.34	4.59	3.90
	MAM	14.07	1.60	5.84	7.32	0.99	3.80	7.52	1.31	3.72
	MMN	-1.17	-2.91	4.49	0.02	-0.18	3.51	0.38	0.19	3.74
	MMM	23.22	9.33	12.10	13.52	5.95	8.74	14.27	6.66	9.24
	Average	3.53	2.05	10.09	1.36	0.94	7.02	1.36	0.96	7.19
	Portion [%]	67.59	50.26	78.44	55.56	50.53	72.22	54.76	50.79	70.63

than 3% (2%) in comparison with the AHW (MHW) method. Also, the MoHW method outperforms the ETS, on average by more than 10%.

For all included disciplines the MoHW method performs better than the ETS method, indicating the universality of the MoHW method regarding the ETS which tries to select the most appropriate method for forecasting.

The MoHW method does not outperform the classical AHW and MHW methods for the classes with no seasonal component (xxN), except for the ANN type, but the MoHW substantially outperforms them for classes with additive/multiplicative trend and additive/multiplicative seasonality, irrespective of the noise. Surprisingly, the fit of the MoHW method is better even in the AA and AM classes, where the AHW and MHW methods are the theoretically correct methods.

Since demand data is usually considered as input to the model in stock control studies, the average costs (for the period $t=T-s$) for forecasts obtained with different forecasting methods were calculated. Table 3 also shows the averages of the SREM1 (the percentage of improvement of the average costs) of the MoHW with respect to the AHW, MHW and ETS.

Almost the same as we observe for the SREM holds for the SREM1. If the MoHW outperforms classical methods regarding the MSE, the MoHW outperforms them regarding the average costs as well as in this case the costs are calculated for forecasts considered as an input to the stock control model.

3.2 Simulated Time Series

We analyzed 300 simulated time series in the same way that we analyzed the real time series from the

M3-Competition. For each method and series, the symmetric relative efficiency measures (the SREM and the SREM1) of the MoHW with respect to the AHW, MHW or ETS were computed. From Table 4 we can observe that for the AAM patterns the MoHW method reduces the MSE on average by more than 71% (55%, 95%) in comparison with the the AHW (the MHW, the ETS) method. For the MAM patterns the MoHW reduces the MSE on average by more than 35% (9%, 84%) in comparison with the AHW (the MHW, the ETS) method.

From Table 4 we can also observe that for the AAM patterns at penalty = 3 the averages of the SREM1 are more than 53%, 40% and 80% with respect to the AHW, MHW and ETS, respectively, and that for penalty = 5 the values of the SREM1 slightly increase. This holds also for the MAM patterns (averages of the SREM1 are now more than 27%, 9% and 61% for penalty = 3). The MoHW method outperforms the AHW and ETS in all 150 cases of the MAM patterns and the MHW in 70% of cases.

Applying all smoothing methods under consideration to the simulated data confirms the good performance of the MoHW method and yields another important insight. For the AAM patterns we can observe that the improvement of the MoHW with respect to other methods increases as seasonality increases and decreases as the slope increases. For the MAM patterns the improvement of the MoHW with respect to the AHW and ETS increases and with respect to the MHW decreases as seasonality increases and increases with respect to all methods as the slope increases.

Table 4. Averages of the SREM and the SREM1 for the simulated time series

MSE → COST	SREM (MSE) [%]			SREM1 (AC) [%]					
	MOHW/ AHW	MOHW/ MHW	MOHW/ ETS	penalty = 3			penalty = 5		
				MOHW/ AHW	MOHW/ MHW	MOHW/ ETS	MOHW/ AHW	MOHW/ MHW	MOHW/ ETS
AAM_5_50	62.17	37.58	93.09	47.15	30.40	74.94	49.28	32.73	74.96
AAM_5_100	81.29	66.70	97.83	59.21	48.47	84.67	60.48	49.54	84.42
AAM_8_100	70.20	62.79	95.42	55.50	43.86	81.56	62.83	50.24	84.51
Average	71.22	55.69	95.45	53.95	40.91	80.39	57.53	44.17	81.30
Portion [%]	100.00	100.00	100.00	100.00	100.00	100.00	100.00	95.56	100.00
MAM_5_50	25.76	9.32	74.98	22.64	12.96	50.82	24.58	14.98	51.62
MAM_5_100	29.15	1.49	88.54	22.66	-1.63	65.96	25.29	-3.04	66.30
MAM_20_50	51.58	17.91	88.95	37.93	18.56	66.53	39.76	20.11	66.68
Average	35.50	9.58	84.16	27.74	9.96	61.10	29.87	10.68	61.53
Portion [%]	94.44	61.11	100.00	100.00	70.00	100.00	100.00	70.00	100.00

Table 5. Averages of the SREM1 obtained with joint optimisation for quarterly time series from the M3-Competition

JOINT		SREM1 (AC) [%]					
		penalty = 3			penalty = 5		
		JMOHW / JAHW	JMOHW / JMHW	JMOHW / ETS	JMOHW / JAHW	JMOHW / JMHW	JMOHW / ETS
Discipline	MICRO	6.25	4.43	33.28	9.49	6.31	46.89
	MACRO	9.76	9.42	30.51	14.50	14.23	44.13
	INDUSTRY	4.83	2.71	26.95	7.22	4.79	41.85
	FINANCE	2.44	2.55	26.38	3.42	3.29	38.56
	DEMOGRAPHIC	2.57	3.42	18.70	6.59	7.85	30.39
Type	ANN	0.88	2.96	32.01	3.52	4.26	45.15
	ANA	2.99	4.66	35.09	3.36	3.59	49.26
	AAN	5.10	4.85	25.11	9.51	8.07	36.75
	AAA	12.24	15.83	36.42	15.26	19.72	49.52
	MNN	3.64	1.42	33.73	3.93	3.92	47.56
	MNA	1.70	0.97	30.15	0.80	2.31	44.37
	MNM	5.63	1.30	37.39	9.21	4.66	51.21
	MAN	6.15	5.41	24.03	12.53	11.53	38.43
	MAA	5.98	10.21	27.93	10.53	13.23	42.17
	MAM	12.60	3.93	26.61	15.86	6.93	42.30
	MMN	7.86	8.23	23.09	13.12	12.51	34.30
	MMM	21.84	13.85	32.44	27.22	17.81	47.85
	Average	6.99	6.20	29.56	10.64	9.47	43.03
	Portion [%]	68.65	63.36	98.02	70.90	64.15	98.68

4 JOINT OPTIMIZATION

In this section we illustrate the advantage of joint optimisation over the optimisation based solely on forecasting data. Namely, the smoothing and initial parameters calculated by optimisation of the forecasting method (the minimisation of the MSE) are not optimal values for minimising the supply chain costs. Therefore, joint optimisation was used (notation *J method*) and the initial and smoothing parameters were optimised to minimise the average total costs of the supply chain (Eq. (17)).

4.1 Real Time Series from the M3-Competition

From the joint optimisation of supply chain (costs) model for the time series from the M3-Competition (see Table 5), we observe the following: joint optimization with the MoHW method (JMoHW) outperforms all other methods for all disciplines and it is particularly good for micro and macroeconomic time series. Also, the JMoHW method outperforms all other methods for all types and it is particularly good for the AAA and MMM patterns.

At the bottom of Table 5, we can see that the SREM1 and a portion of series with an improved SREM1 increase as the penalty increases.

Table 6. Averages of the SREM1 for the time series from the M3-Competition (a comparison between the joint model and the model where the forecasting/inventory problem is treated separately)

JOINT/not_joint		SREM1 (AC) [%]			
		penalty = 3		penalty = 5	
		JMOHW/ AHW	JMOHW/ MHW	JMOHW/ AHW	JMOHW/ MHW
Discipline	MICRO	28.38	27.15	42.60	41.61
	MACRO	25.27	25.44	39.70	39.86
	INDUSTRY	25.36	24.01	41.11	39.91
	FINANCE	24.27	24.55	37.84	38.11
	DEMOGRAPHIC	15.31	15.46	27.39	27.27
Type	ANN	23.76	23.31	38.01	37.49
	ANA	39.28	41.19	42.07	43.52
	AAN	43.62	45.00	30.35	31.22
	AAA	58.30	59.83	45.96	46.70
	MNN	41.08	41.51	43.33	42.73
	MNA	42.84	44.35	41.41	40.64
	MNM	47.13	44.78	44.46	43.23
	MAN	41.94	44.19	35.66	36.04
	MAA	41.54	43.51	39.61	42.81
	MAM	42.97	41.84	45.61	40.85
	MMN	44.28	45.12	32.12	32.06
	MMM	36.14	30.54	50.86	46.41
	Average	25.27	24.90	39.52	39.21

Table 7. Averages of the SREM1 obtained with joint optimisation for the simulated time series

JOINT	SREM1 (AC) [%]					
	penalty = 3			penalty = 5		
	JMOHW / JAHW	JMOHW / JMHW	JMOHW / ETS	JMOHW / JAHW	JMOHW / JMHW	JMOHW / ETS
AAM_5_50	52.98	36.71	80.46	65.61	58.67	85.74
AAM_5_100	61.23	44.29	86.80	67.56	44.93	88.69
AAM_8_100	58.13	53.95	85.14	71.77	53.10	89.80
Average	57.45	44.98	84.13	68.31	52.23	88.08
Portion [%]	100.00	94.44	100.00	100.00	91.11	100.00
MAM_5_50	29.80	37.00	65.41	45.03	39.08	75.36
MAM_5_100	16.85	9.23	75.66	14.44	8.52	79.43
MAM_20_50	53.15	19.56	76.45	65.00	26.93	81.52
Average	33.27	21.93	72.50	41.49	24.85	78.77
Portion [%]	96.67	95.56	100.00	98.89	91.11	100.00

Finally, if we use the JMoHW instead of the models where forecasts are calculated with the AHW or MHW method regarding minimising the MSE, we can observe the following (see Table 6): for penalty=5 (penalty=3) the JMoHW (on average) can reduce the average costs by at least 37.84% (24.27%) for all disciplines, except for a demographic series, where the JMoHW can reduce costs “only” by 27.27% (15.31%) in comparison with the AHW (the MHW) method.

For different types of series we can observe that for penalty=3 the JMoHW can reduce the average costs for the ANN and MMM patterns “only” by 23% to 36% and for all other types by 39% to 60%. For penalty=5, the JMoHW can reduce the costs for patterns with no season “only” by 30% to 43% and for other types by 40% to 51%.

4.2 Simulated Time Series

For the AAM patterns we can observe (see Table 7) that the improvement of the JMoHW with respect to all others methods increases as seasonality increases, except for the JMHW for penalty=5. Also, for penalty=5 the improvement of the JMoHW with respect to all others methods increases as the slope increases, and this also holds for the JMHW at penalty=3.

For the MAM patterns the improvement of the JMoHW with respect to the ETS increases and with respect to the JAHW and the JMHW decreases as seasonality increases. Also, the improvement of the JMoHW with respect to the JAHW and the ETS increases and with respect to the JMHW decreases as the slope increases.

Finally, if we use JMoHW instead of the models where forecasts are calculated with the AHW or MHW method regarding minimising the MSE, we can observe (see Table 8) that the JMoHW can essentially reduce the average costs on average by more than 60% (48%) in comparison with the AHW (MHW) method. The improvement of the JMoHW with respect to the AHW and the MHW at the AAM patterns is greater than at the MAM patterns and increases as the penalty increases for both types of patterns.

Table 8. Averages of the SREM1 for a simulated time series (a comparison between the joint model and the model where the forecasting/inventory problem is treated separately)

JOINT/ not_joint	SREM1 (AC) [%]			
	penalty = 3		penalty = 5	
	JMOHW/ AHW	JMOHW/ MHW	JMOHW/ AHW	JMOHW/ MHW
AAM_5_50	58.91	45.60	71.20	61.66
AAM_5_100	64.93	54.93	71.46	63.27
AAM_8_100	63.99	53.85	75.54	66.88
Average	62.61	51.46	72.73	63.94
MAM_5_50	44.78	36.45	61.70	54.89
MAM_5_100	44.50	23.94	55.24	34.51
MAM_20_50	55.50	40.61	66.30	54.10
Average	48.26	33.66	61.08	47.83

5 CONCLUSION AND FURTHER RESEARCH

The biggest challenges facing the European energy policy are sustainable energy supply, reducing dependence on energy resources and energy efficiency. Appropriate energy-demand forecasting methods offer many opportunities regarding process optimisation and appropriate strategic decisions.

This paper exposes two problems: the problem of forecasting energy demand with large noise and the problem of the local optimisation of forecasting methods. We propose the modified HW method for a simultaneous optimisation of demand forecasting and total costs.

From our study of 756 quarterly real series from the M3-Competition and 300 simulated demand patterns we can conclude that the average costs can always be reduced if we use joint optimisation with the MoHW method. For real data they can be reduced on average by more than 24% for penalty=3 and by more than 39% for penalty=5 in comparison with the models where forecasts are calculated with the AHW or MHW methods regarding minimising the MSE and are treated separately from the cost model. When joint optimisation with the modified HW method for simulated data was used, the average costs were reduced on average by more than 55% (42%) for penalty=3 and by more than 66% (55%) for penalty=5 in comparison with the AHW (MHW).

Joint optimization ensures better planning performance with energy resources, better utility of power plant assets and much more efficient production of derivate energy products from primary energy sources. Finally, the result shows that sharing information and comprehensive energy resource management lead to essential reduction of the total cost.

Further research will include a detailed study of the impact of the modified HW method on the bullwhip effect if the proposed joint optimisation is used. Also, relaxation of the limitation for the lead time assumed to be only one period will be analysed for better evaluation of the joint model over longer horizons. It would be also interesting to investigate how the proposed joint optimization with the modified HW method would effect the systems described in [22].

6 REFERENCES

- [1] European Commission. 2050 Energy strategy, from <http://ec.europa.eu/energy/en/topics/energy-strategy/2050-energy-strategy>, accessed on 2016-08-18.
- [2] European Commission. Global Europe 2050, from https://ec.europa.eu/research/social-sciences/pdf/policy_reviews/global-europe-2050-report_en.pdf, accessed on 2016-08-18.
- [3] European Commission. Energy roadmap 2050, from https://ec.europa.eu/energy/sites/ener/files/documents/2012_energy_roadmap_2050_en_0.pdf, accessed on 2016-08-18.
- [4] Gracanin, D., Lalic, B., Beker, I., Lalic, D., Buchmeister, B. (2013). Cost-time profile simulation for job shop scheduling decisions. *International Journal of Simulation Modelling*, vol. 12, no. 4, p. 213-224, DOI:10.2507/IJSIMM12(4)1.237.
- [5] Kremljak, Z., Palcic, I., Kafol, C. (2014). Project evaluation using cost-time investment simulation. *International Journal of Simulation Modelling*, vol. 13(4), p. 447-457, DOI:10.2507/IJSIMM13(4)5.279.
- [6] Ferbar Tratar, L., Strmčnik, E. (2016). The comparison of Holt-Winters method and Multiple regression method:a case study. *Energy*, vol. 109, p. 266-276, DOI:10.1016/j.energy.2016.04.115.
- [7] Potočnik, P., Strmčnik, E., Govekar, E. (2015). Linear and neural network-based models for short-term heat load forecasting. *Strojniški vestnik - Journal of Mechanical Engineering*, vol. 61, no. 9, p. 543-550, DOI:10.5545/sv-jme.2015.2548.
- [8] Strijbosch, L.W.G., Syntetos, A.A., Boylan, J.E., Janssen, E. (2011). On the interaction between forecasting and stock control: The case of non-stationary demand. *International Journal of Production Economics*, vol. 133, no. 1, p. 470-480, DOI:10.1016/j.ijpe.2009.10.032.
- [9] Ferbar Tratar, L. (2010). Joint optimisation of demand forecasting and stock control parameters. *International Journal of Production Economics*, vol. 127, no. 1, p. 173-179, DOI:10.1016/j.ijpe.2010.05.009.
- [10] Ma, Y., Wang, N., Che, A., Huang, Y., Xu, J. (2013). The bullwhip effect on product orders and inventory: a perspective of demand forecasting techniques. *International Journal of Production Research*, vol. 51, no. 1, p. 281-302, DOI:10.1080/00207543.2012.676682.
- [11] Gardner, Jr. E.S. (1985). Exponential smoothing: The state of the art. *Journal of Forecasting*, vol. 4, no. 1, p. 1-28, DOI:10.1002/for.3980040103.
- [12] Makridakis, S., Hibon, M. (2000). The M3-Competition: results, conclusions and implications. *International Journal of Forecasting*, vol. 16, no. 4, p. 451-476, DOI:10.1016/S0169-2070(00)00057-1.
- [13] Glavan, I., Prelec, Z., Pavkovic, B. (2015). Modelling, simulation and optimization of small-scale CCHP energy systems. *International Journal of Simulation Modelling*, vol. 14, no. 4, p. 683-696, DOI:10.1016/S0169-2070(00)00057-1.
- [14] R Core Team (2014). *R: A language and environment for statistical computing*. Version 3.1.0. R Foundation for Statistical Computing, Vienna.
- [15] Ypma, J., Borchers, H.W. (2014). nloptr: R interface to NLOpt. <https://CRAN.R-project.org/web/package=nloptr>, accessed on 2016-10-03.
- [16] Hyndman, R.J., Akram, M., Bergmeir, C. (2013). *Mcomp: Data from the M-competitions*. R package version 2.05.
- [17] Hyndman, R.J., Athanasopoulos, G., Razbash, S., Schmidt, D., Zhou, Z., Khan, Y., Bergmeir, C., Wang, E. (2014). *Forecast: Forecasting functions for time series and linear models*. R package version 2.05.
- [18] Hyndman, R.J., Khandakar, Y. (2008). Automatic time series forecasting: The forecast package for R. *Journal of Statistical Software*, vol. 27, no. 3, DOI:10.18637/jss.v027.i03.
- [19] Zhao, X., Lee, T.S. (1993). Freezing the master production schedule in multilevel material requirements planning systems under demand uncertainty. *Journal of Operations*

Management, vol. 11, no. 2, p. 185-205, DOI:10.1016/0272-6963(93)90022-H.

- [20] Bermúdez, J.D., Segura, J.V., Vercher, E. (2006). A decision support system methodology for forecasting of time series based on soft computing. *Computational Statistics & Data Analysis*, vol. 51, no. 1, p. 177 - 191, DOI:10.1016/j.csda.2006.02.010.
- [21] Escuin, D., Polo, L., Cipres, D. (2017). On the comparison of inventory replenishment policies with time-varying stochastic

demand for the paper industry. *Journal of Computational and Applied Mathematics*, vol. 309, p. 424-434, DOI:10.1016/j.cam.2016.03.027.

- [22] Šljivac, D., Nakomčić-Smaragdakis, B., Vukobratović, M., Topić, D., Čepić, Z. (2014). Cost-benefit comparison of on-grid photovoltaic systems in pannonian parts of Croatia and Serbia. *Tehnički vjesnik - Technical Gazette*, vol. 21, no. 5, p. 1149-1157.

Vsebina

Strojniški vestnik - Journal of Mechanical Engineering

letnik 62, (2016), številka 11
Ljubljana, november 2016
ISSN 0039-2480

Izhaja mesečno

Razširjeni povzetki (extended abstracts)

- Mehdi Jafari Vardanjani, Alireza Araee, Jacek Senkara, Majid Sohrabian, Roozbeh Zarandooz:
Vpliv vzporednih tokov na metalurške in mehanske lastnosti uporovnih točkovnih zvarov
zlitine AA2219 SI 111
- Tahsin Tecelli Öpöz, Xun Chen: Analiza mehanizmov oblikovanja odrezkov s simulacijo po metodi
končnih elementov SI 112
- Liqiang Zhang, Kai Zhang, Yecui Yan: Algoritem za lokalno glajenje petosne linearne poti orodja v
ogliščih z dvema kubičnima krivuljama NURBS SI 113
- Piotr Zgórnjak, Wojciech Stachurski, Dariusz Ostrowski: Uporaba termografskih meritev za
določanje vpliva izbranih rezalnih parametrov na temperaturo obdelovanca med postopkom
rezkanja SI 114
- Yongsheng Zhao, Cheng Yang, Ligang Cai, Weimin Shi, Yi Hong: Model togosti in dušenja vijačne
zveze s porazdelitvijo kontaktnega pritiska po neenakomerni površini SI 115
- Xiangyang Xu, Youchuan Tao, Changrong Liao, Shaojiang Dong, Renxiang Chen: Dinamična
simulacija planetnega gonila vetrne turbine z upogljivim ohišjem SI 116
- Liljana Ferbar Tratar: Celovito upravljanje z energijskimi viri za bistveno zmanjšanje celotnih
stroškov SI 117
- Osebnosti** SI 118

Vpliv vzporednih tokov na metalurške in mehanske lastnosti uporovnih točkovnih zvarov zlitine AA2219

Mehdi Jafari Vardanjani^{1,*} – Alireza Araee¹ – Jacek Senkara² – Majid Sohrabian³ – Roozbeh Zarandooz⁴

¹ Univerza v Teheranu, Fakulteta za strojništvo, Iran

² Tehniška univerza v Varšavi, Oddelek za varilno tehniko, Poljska

³ Znanstveno-tehniška univerza, Fakulteta za strojništvo, Iran

⁴ Tehniška univerza v Araku, Fakulteta za strojništvo, Iran

Uporovno točkovno varjenje (RSW) je eden najbolj razširjenih postopkov pri izdelavi karoserij vozil. S tem postopkom je mogoče izdelati enega samega ali več točkovnih zvarov v vrsti, v slednjem primeru pa se pojavijo vzporedni tokovi. Vzporedni tokovi pri uporovnem točkovnem varjenju nastanejo, ko si električni tok poišče pot skozi predhodne točkovne zveze v vrsti. Velikost teh tokov je odvisna predvsem od dejavnikov kot so oddaljenost, število in velikost predhodnih točkovnih zvarov. V prizadeti zvarni leči se pojavijo dimenzijske in metalurške spremembe kot posledica sprememb v porazdelitvi električnega toka in toplote. Pojav je bolj izražen pri zlitinah z veliko električno prevodnostjo, kot so aluminijeve zlitine, vse pomembnejši pa bo tudi v industrijah z mnogimi vmesnimi točkovnimi zvari (npr. v letalski in vesoljski industriji).

V predstavljeni raziskavi je bil eksperimentalno analiziran vpliv vzporednih tokov na metalurške in mehanske lastnosti uporovnih točkovnih zvarov pri zlitini AA2219.

Preučene so bile mehanske in metalurške lastnosti, z numeričnimi rezultati analize po metodi končnih elementov (MKE) pa so bili preverjeni tudi toplotni vidiki tega pojava in njihov vpliv na rezultate eksperimentov. Za glavno spremenljivko je bila izbrana razdalja med dvema zaporednima zvaroma v vrsti. Napovedi temperaturne porazdelitve in hitrosti hlajenja iz analize MKE so bile preverjene s kontrolo dimenzij leč in toplotno vplivanega področja (HAZ), preiskavo razpok z vrstičnim elektronskim mikroskopom in natezno-strižnim preizkusom. Zasnovan je bil trifaktorski eksperiment za ugotovitev signifikantnosti dejavnikov in njihovih medsebojnih vplivov na dimenzije leče.

Glavni eksperimenti so bili opravljeni z novimi ravnmi faktorjev, enak postopek pa je bil nato uporabljen tudi pri natezno-strižnih preizkusih točkovnih zvarov. Numerični model upošteva medsebojne toplotne in električne vplive, vključno s temperaturno odvisnostjo materialnih lastnosti in kontaktnimi prevodnostmi. Eksperimentalni rezultati se ujemajo z napovedmi. V analizi MKE so bili napovedani razvoj HAZ, prisotnost razpok, vrste odpovedi ter mehanska trdnost prizadete leče pri različnih razmikih leč v obliki temperaturnih porazdelitev in hitrosti ohlajanja prizadete leče. Napoved temperaturnih variacij je bila preverjena tudi s primerjavo maksimalne temperature, pridobljene pri analizi MKE, in maksimalne temperature po linearni odvisnosti med vhodno močjo in največjo dosegljivo temperaturo. Ugotovljena je bila rast HAZ z raztezanjem proti predhodni leči, ki je bila intenzivnejša pri manjšem razmiku med zvari. Napovedane hitrosti ohlajanja razkrivajo tudi krhkost strukture prizadete leče in HAZ, ki bi lahko bila povezana s prisotnostjo metastabilne nekoherentne faze med procesom ohlajanja pri manjših razmikih med lečami. Posnetki, narejeni z vrstičnim elektronskim mikroskopom, so razkrili več razpok in manjšo natezno-strižno trdnost, možni vzrok pa bi lahko bila prisotnost delcev, bogatih z bakrom v mikrostrukturi. Preverjanje načina odpovedi prizadetih leč v različnih razmikih je pokazalo prisotnost več razpok v leči, ki so posledica krhkosti in povzročajo lom med ploskvami pri manjših razmikih. Pri večjem razmiku (20 mm) je prišlo do izvleka zvara brez kritičnih razpok v okolici leče. 20-milimetrski razmik med zvarnimi točkami bi torej lahko omogočil doseganje zahtevane kakovosti pri danem materialu in pogojih varjenja, ob upoštevanju omejitev pri razporedu točkovnih zvarov in zahtev učinkovitega izkoriščenja prostora.

Predlagani numerični model omogoča nadzor nad vzporednimi tokovi pri uporovnem točkovnem varjenju za zagotavljanje metalurških in mehanskih lastnosti točkovnih zvarov.

Ključne besede: pojav vzporednih tokov, toplotno vplivano področje, natezna in strižna trdnost, način odpovedi, analiza po metodi končnih elementov, eksperimenti

Analiza mehanizmov oblikovanja odrezkov s simulacij po metodi končnih elementov

Tahsin Tecelli Öpöz* – Xun Chen

Univerza Johna Mooresa v Liverpoolu, Tehniški raziskovalni inštitut, Liverpool, Združeno kraljestvo

Napovedovanje oblike odrezkov, ki nastajajo pri obdelavi z odrezavanjem, je pomembno za zagotavljanje zelene površine obdelovancev in preprečevanje poškodb, ki jih med obdelavo povzročajo odrezki. Rezultati predstavljene raziskave in simulacij po metodi končnih elementov podajajo poglobljen pregled nad mehanizmi nastajanja odrezkov pri obdelavi kovin z odrezavanjem ter nad vplivi različnih procesnih parametrov. Analiza po metodi končnih elementov je zelo uporaben numerični pristop k napovedovanju vrste in oblike odrezkov, mehanskih in toplotnih napetosti ter rezalnih sil pri oblikovanju odrezkov. Napovedovanje mehanizmov oblikovanja odrezkov v različnih delovnih pogojih samo na podlagi eksperimentov bi bilo namreč zelo težavno in drago. Rezultati analize po MKE so lahko preventivno sredstvo za preprečevanje neželenih tresljajev in termičnih poškodb med procesom obdelave.

Opravljen je bil vrsta simulacij oblikovanja odrezkov s programsko opremo Abaqus/Explicit. Simulirane so bile tri vrste odrezkov – neprekinjeni, nazobčani in prekinjeni –, ki se oblikujejo pri različnih vrednostih parametrov kot sta cepilni kot in globina reza. V modelu oblikovanje odrezkov po MKE sta bila uporabljena Johnson-Cookov model napetosti pri preoblikovanju in Johnson-Cookov progresivni model poškodb. Začetek razpoke in vedenje materiala po nastanku razpoke sta bila opredeljena z razvojem poškodbe na podlagi Hillerborgovega parametra lomne energije. Za ohranitev kakovosti mreže v simulaciji in zmanjšanje stopnje popačenja elementov pri ekstremnih deformacijah je bila uporabljena arbitrarna Lagrangeova-Eulerjeva tehnika (ALE) prilagojenega mreženja.

Rezultati so dokazali vpliv lomne energije, globine reza in cepilnega kota na oblikovanje odrezkov. Opravljen je bil vrsta simulacij s postopnim večanjem lomne energije ($G_f = 250$ N/m, 2500 N/m, 10.000 N/m in 20.000 N/m) za dve različni globini reza ($h = 20$ μm in 50 μm) in štiri različne cepilne kote ($\gamma = 22^\circ, 0^\circ, -30^\circ, -45^\circ$). Pri večjih lomnih energijah se oblikujejo neprekinjeni odrezki, pri manjših lomnih energijah pa so odrezki prekinjeni. Poleg tega so odrezki pri večjih lomnih energijah bolj ravni. Vpliv globine reza je bil preizkušen pri lomni energiji 2500 N/m: pri globini reza 20 μm so odrezki neprekinjeni, pri 50 μm pa nazobčani. Simulacije so pokazale, da ima tudi cepilni kot pomembno vlogo pri oblikovanju odrezkov. Pri cepilnih kotih $22^\circ, 0^\circ$ in -30° so bili ugotovljeni neprekinjeni, nazobčani (segmentirani) in prekinjeni odrezki. Ko se cepilni kot spreminja od pozitivnih proti negativnim vrednostim, se pojavi tendenca po prehajanju od neprekinjenih k prekinjenim odrezkom. Čeprav predhodne raziskave ne poročajo o večjem vplivu cepilnega kota na stopnjo segmentacije odrezkov, je bilo ugotovljeno, da ima cepilni kot signifikanten vpliv predvsem pri manjših globinah reza. Simulacije so pokazale, da so odrezki z naraščanjem globine reza vse bolj segmentirani, dokler se končno ne oblikujejo nazobčani odrezki. Te ugotovitve so pomembne za brušenje, kjer je globina reza manjša in so cepilni koti bistveno bolj negativni.

V predhodnih raziskavah je bila vrednost Hillerborgove lomne energije ocenjena z vrednostmi K_{IC} . Le-te pa so odvisne od velikosti testnega vzorca, kot je opisano v članku. Poudarjeno je, da je lahko računanje zahtevane lomne energije iz vrednosti K_{IC} težavno, vedenje materiala pri oblikovanju odrezkov pa je v določenih pogojih simulacije mogoče napovedati že z ocenjeno vrednostjo lomne energije. Izkazalo se je tudi, da so računalniške simulacije majhnih globin reza do mikronske ravni težavne zaradi velikosti mreže in potrebne računske moči. Problem občutljivosti mreže pri analizah po metodi končnih elementov je znan in rezultati so odvisni od velikosti mreže. Za omejitev odvisnosti od mreže je bila v tej raziskavi uporabljena tehnika razvoja poškodb z linearnim mehčanjem na podlagi Hillerborgovega modela lomne energije. V prihodnjih raziskavah bi lahko uporabili različne velikosti mreže ter preučili občutljivost mreže pri simulaciji oblikovanja odrezkov po MKE.

Ključne besede: oblikovanje odrezkov, metoda končnih elementov, lomna energija, odrezavanje kovin, razvoj poškodb

Algoritem za lokalno glajenje petosne linearne poti orodja v ogliščih z dvema kubičnima krivuljama NURBS

Liqliang Zhang^{1,*} – Kai Zhang¹ – Yecui Yan²

¹ Tehniška univerza v Šanghaju, Kolidž za strojništvo, Kitajska

² Tehniška univerza v Šanghaju, Kolidž za avtomobilsko tehniko, Kitajska

Petosne poti orodij so pogosto sestavljene iz linearnih segmentov s tangentnimi nezveznostmi v ogliščih, zaradi česar se tangencialna hitrost v ogliščih med sosednjima segmentoma sunkovito spreminja ali je enaka nič. Pri petosnih NC-sistemih se zato še vedno pojavlja izziv usklajevanja točnosti obdelave in gladke trajektorije orodja.

V članku je uporabljen pristop s parom kubičnih krivulj NURBS, ki imata vnaprej določeno točnost prilaganja, za glajenje poti v ogliščih med sosednjima linearnima segmentoma in ustvarjanje gladke poti orodja z zveznostjo G^2 v delovnem koordinatnem sistemu.

Osnova za glajenje petosne poti orodja v ogliščih je glajenje pri triosnih linearnih segmentih. Prva kubična krivulja NURBS je namenjena glajenju translacijske poti, druga pa rotacijske poti v oglišču. Z vključitvijo dveh kubičnih krivulj NURBS za glajenje translacijske in rotacijske komponente je mogoče uspešno zgladiti petosno linearno pot orodja v oglišču. Za translacijske trajektorije točk na konici orodja je konstruiran model gladkega prehoda v ogliščih s krivuljami NURBS, ki izpolnjuje omejitve glede napak in zagotavlja zveznost razreda G^2 .

Z vstavitvijo dveh kubičnih krivulj NURBS v sosednja segmenta je mogoče ustvariti gladko petosno pot orodja z zveznostjo razreda G^2 . Pri interpolaciji petosne poti orodja morata translacija konice orodja in rotacija orodne osi potekati zvezno in gladko, zato je ključna sinhronizacija translacijske trajektorije točk na konici orodja in rotacijske trajektorije točk na osi orodja.

Za preverjanje uporabnosti in natančnosti predlaganega algoritma so bile z izračunom odstopanja obdelane površine opredeljene napake pri rezkanju lopatice. Rezultati primerjave kažejo, da je predlagani algoritem za glajenje poti v ogliščih visokonatančen in lahko pomembno izboljša kakovost obdelane površine.

Predlagani algoritem ima tri prednosti: (1) Par kubičnih krivulj NURBS je omejen s petimi kontrolnimi točkami in lahko zgladi translacijsko trajektorijo točk na konici orodja in rotacijsko trajektorijo točk na osi orodja z zveznostjo G^2 . Zaradi zveznosti tangent in ukrivljenosti je možno povečanje hitrosti in pospeškov. (2) Napaka aproksimacije je v analitičnem razmerju z dolžino prehoda zglajene krivulje in analitično konstruiranje dvojnih krivulj NURBS, ki dosegajo vnaprej določeno mejo napake, je zato preprosto. (3) Sinhronizacijska metoda jamči za zvezno variabilnost orientacije orodja.

Ključne besede: petosna obdelava, prehod v ogliščih, dvojne krivulje NURBS, pot orodja

Uporaba termografskih meritev za določanje vpliva izbranih rezalnih parametrov na temperaturo obdelovanca med postopkom rezkanja

Piotr Zgórnjak* – Wojciech Stachurski – Dariusz Ostrowski
Tehniška univerza v Lodzu, Inštitut za obdelovalne stroje in proizvodni inženiring, Poljska

Glavni cilj raziskave je razdelava metodologije za vrednotenje vpliva rezalnih parametrov na temperaturo obdelovancev med postopkom rezkanja, ki bi jo bilo mogoče uporabljati tudi v proizvodnih obratih.

Vse večja pričakovanja glede produktivnosti in učinkovitosti so privedla do tega, da nastaja v rezalnih procesih tudi vse več toplote. Če naj bodo končni izdelki v zahtevanih dimenzijah, je zaradi intenzivnega segrevanja nujno hlajenje in mazanje. Ustvarjena toplota ne vpliva le na trajnost rezalnih orodij, temveč tudi na lastnosti površinskega sloja obdelovanca. Našteti razlogi opravičujejo razvoj infrardeče merilne tehnologije.

Članek obravnava vrednotenje vpliva izbranih rezalnih parametrov na temperaturo v obdelovancu. Opravljene so bile raziskave z rezkanjem jeklene litine 41Cr4 z diskastim rezkarjem s ploščicami iz sintrane karbidne trdine F40M, opremljenimi s protiobrabno prevleko. Uporabljen je bil postopek suhega rezkanja, tri rezalne in tri podajalne hitrosti, globina reza pa je bila konstantna. Temperatura v območju obdelave je bila posneta z infrardečo kamero Flir SC6000HS. Za vse posnetke v vrsti je bila izračunana srednja temperatura in v naslednji fazi so bila preučena samo tista območja, ki ustrezajo mestu obdelovancev.

Rezultat infrardečih meritev je srednja temperatura v opredeljenem merilnem območju, na osnovi tega pa je podan predlog postopka za določanje maksimalne temperature v obdelovancu. Rezultati so pokazali, da povečanje rezalne hitrosti privede do povečanja maksimalne temperature obdelovanca, povečanje podajalne hitrosti pa do zmanjšanja te temperature. Celo pri razmeroma majhni razliki med temperaturo okolice in temperaturo obdelovanca je možna optimizacija rezalnih parametrov.

Na rezultate infrardečih meritev vplivajo mnogi dejavniki, npr. omejitve strojne in programske opreme, od temperature odvisen koeficient emisivnosti, prisotnost različnih virov toplote itd. Zaradi hitrih relativnih gibanj med rezalnim orodjem in obdelovancem je analiza temperaturnih polj zelo težavna, avtorji pa so se zato odločili za primerjalne preizkuse v čim bolj podobnih razmerah. Kljub temu, da imajo termopari številne slabosti (npr. težavno natančno pozicioniranje v obdelovancu, motnje toplotnega polja, enotočkovne meritve), bi bili lahko primerni za validacijo in umerjanje termografskih meritev. To bo predmet prihodnjih raziskav.

Temperatura, ki se tvori pri postopkih obdelave z odrezavanjem, je pomemben dejavnik pri oblikovanju lastnosti površinskega sloja ter mora biti vključena v metodologijo izbire rezalnih parametrov za zadovoljivo produktivnost in ohranitev omenjenih lastnosti. Predlagane infrardeče meritve so obetavno sredstvo za optimizacijo obdelovalnih procesov, ki je primerno tudi za tovarne.

Ključne besede: obdelava, IR-meritve, temperatura obdelovanca, termografske meritve, rezkanje, infrardeče meritve, toplotno slikanje

Model togosti in dušenja vijačne zveze s porazdelitvijo kontaktnega pritiska po neenakomerni površini

Yongsheng Zhao^{1,*} – Cheng Yang¹ – Ligang Cai¹ – Weimin Shi² – Yi Hong¹

¹ Institut za tehnologijo v Pekingu, Državni laboratorij za napredne proizvodne tehnologije, Kitajska

² Tehniška univerza v Pekingu, Kolidž za računalništvo, Kitajska

Vijačne zveze se množično uporabljajo pri konstrukcijskih komponentah, kjer so pogosto eden najšibkejših členov in lahko pomembno vplivajo na dinamične lastnosti obdelovalnega stroja. V tej raziskavi je bil ustvarjen model togosti in blaženja s porazdelitvijo kontaktnega pritiska po neenakomerni površini, ki točno napoveduje dinamične lastnosti sestava.

Normalno togost, tangencialno togost in dušenje kontaktne površine je mogoče izpeljati na podlagi teorije fraktalnega kontakta, ki je običajno enak za vse elemente togosti in dušenja po celotni kontaktni površini. Ta hipoteza pa ni primerna za vijačne zveze zaradi vpliva koncentracije sil pri sestavih z več vijaki. Zaradi neenakomerne porazdelitve pritiska se togost in dušenje spreminjata po kontaktni površini vijačne zveze.

Za opredelitev togosti in dušenja vijačne zveze je uveden pritisk kontaktne površine. Privzeta je bila domneva ravne kontaktne površine na makro nivoju in v tem primeru je porazdelitev pritiska po kontaktni površini mogoče ugotavljati po metodi končnih elementov (MKE). Najprej se izberejo vozlišča kontaktne površine in nato je mogoče določiti kontaktne napetosti v splošnem modulu Postproc programskega paketa ANSYS. Na podlagi vozliščnih napetosti kontaktne površine je mogoče opredeliti nelinearno odvisnost za togost in blaženje vijačne zveze ter za pritisk po kontaktni površini. Vrednosti togosti in dušenja so dodeljene elementu Matrix 27, ki povezuje vozlišča dveh kontaktnih površin.

Za validacijo predlaganega modela je bil zasnovan eksperiment s preizkušancem v obliki škatle. Ko je sila prednapetosti enaka, je lastna frekvenca v primeru neenakomernega pritiska bistveno bližja rezultatom eksperimenta kot v primeru enakomernega pritiska. Neenakomerna porazdelitev pritiska po kontaktni površini lahko resno vpliva na točnost analize vijačne zveze. Upogibni moment vpliva na porazdelitev kontaktnega pritiska in povzroči poslabšanje kontaktne togosti vijačne zveze. Glavni razlog je v tem, da upogibni moment še ojači neenakomernost porazdelitve kontaktnega pritiska. Ugotovljeno je bilo tudi, da je s povečanjem sile prednapetosti mogoče povečati prvo lastno frekvenco. Ta se počasi povečuje, ko je sila prednapetosti večja od 24 kN. Glavni razlog je v rasti kontaktnega pritiska blizu vijakov, ko se povečuje sila prednapetosti. Kontaktni pritisk na večji oddaljenosti od vijakov pri tem ostaja praktično nespremenjen.

Za merjenje površinske hrapavosti je potreben profilometer, izmerjena površina pa mora ustrezati preizkušancu v obliki škatle. Tedaj je hrapavost površine mogoče opisati s fraktalno teorijo in predlagani model je uporaben za točno napovedovanje dinamičnih lastnosti vijačne zveze.

Predstavljeni model je uporaben za učinkovito modeliranje vijačnih zvez, ki so ali niso pod vplivom zunanjih obremenitev, in lahko točno napoveduje vedenje vijačnih zvez na obdelovalnem stroju.

Ključne besede: vijačna zveza, kontaktna togost in dušenje, teorija fraktalnega kontakta, neenakomerna porazdelitev pritiska, obdelovalni stroj

Dinamična simulacija planetnega gonila vetrne turbine z upogljivim ohišjem

Xiangyang Xu^{1,2*} – Youchuan Tao³ – Changrong Liao² – Shaojiang Dong¹ – Renxiang Chen¹

¹ Univerza Chongqing Jiaotong, Šola za mehatroniko in avtomobilsko tehniko, Kitajska

² Univerza v Chongqing, Kolidž za optoelektroniko, Kitajska

³ CSIC (Chongqing) Haizhuang Windpower Equipment Co., Ltd., Kitajska

Planetna gonila imajo mnoge prednosti, ki jih s pridom izkoriščamo pri vetrnih turbinah; med njimi so veliko prestavno razmerje, kompaktna konstrukcija in dobra sposobnost porazdeljevanja moči. Večina predhodnih študij planetnih prenosnikov privzema, da je ohišje gonila togo telo in ta domneva je upravičena pri planetnih gonilih za majhne moči, kjer so deformacije ohišja gonila zanemarljive. Pri večjih obremenitvah, kot se pojavljajo pri vetrnih turbinah, pa lahko ta upogljivost ohišja povzroči velika odstopanja v rezultatih izračunov. Določitev odvisnosti med upogljivostjo ohišja gonila in dinamičnimi značilnostmi je zato velikega praktičnega pomena.

Dinamične lastnosti planetnih gonil vetrnih turbin so preučevali mnogi raziskovalci. Obstoječe študije zagotavljajo pomembne smernice za konstruiranje optimalnih prenosnikov za vetrne turbine, ne upoštevajo pa upogljivosti ohišja gonila. Zaradi zahtevnosti konstrukcije ohišja gonila in plavajočih komponent je tudi težko popisati dinamične lastnosti planetnega prenosnika, če model vključuje upogljivost ohišja.

Upogljivost ohišja ima velik vpliv na dinamični odziv in na porazdelitve obremenitev med planetnimi zobniki. Članek podrobno preučuje robne pogoje povezav med podsistemom planetnega prenosnika in podsistemom ohišja gonila. V dinamični model je vključena upogljivost ohišja in simulirani so njeni vplivi na dinamični odziv ter na porazdelitev obremenitev. Upogljivost ohišja gonila, ki je bila določena po metodi končnih elementov, je nato vključena v dinamični model z združenimi parametri za simulacijo njenega vpliva na dinamične lastnosti in na porazdelitev obremenitev.

Numerični rezultati kažejo, da lahko togost ohišja gonila občutno zmanjša vršne vrednosti dinamične napake prenosa in dinamične sile ubiranja, zmanjšajo pa se tudi vršne frekvence dinamične sile ubiranja. Vršne vrednosti dinamičnega odziva se povečujejo z rastjo zunanjih obremenitev, medtem ko frekvenčni vrhovi ostajajo na istem mestu. Plavajoči odmiki sončnega zobnika so lahko večji ob upoštevanju fleksibilnosti ohišja gonila, izboljša pa se tudi porazdelitev obremenitev. Eksperimenti so pokazali, da se le-ta dobro ujema s teoretičnimi vrednostmi.

Ključne besede: gonilo vetrne turbine, planetno gonilo, upogljivost ohišja gonila, sklopljen dinamični model, dinamične lastnosti, porazdelitev obremenitev

Celovito upravljanje z energijskimi viri za bistveno zmanjšanje celotnih stroškov

Liljana Ferbar Tratar*

Univerza v Ljubljani, Ekonomska fakulteta, Slovenija

Celovito upravljanje z energijskimi viri predstavlja enega od možnih načinov globalne optimizacije, ki je stroškovno veliko bolj učinkovito kot ločena obravnava modela napovedovanja povpraševanja po energentih in modela upravljanja z zalogami energentov. V članku predstavimo dvo-nivojsko (centralizirano) dobavno verigo, kjer distributer derivatov energije (npr. tople vode, pare, električne energije) deli informacije o povpraševanju letih z dobaviteljem primarnih virov energije (npr. premoga, nafte, plina).

Za napovedovanje povpraševanja (na kratki ali dolgi rok) lahko uporabimo različne metode. V praksi se najpogosteje uporabljajo metode eksponentnega glajenja, saj so preproste, hitre in ne zahtevajo dodatne programske opreme. Metode eksponentnega glajenja vsebujejo nekaj enostavnih rekurzivnih enačb, ki jih lahko implementiramo v Microsoft Excel-u, optimizacijo pa izvedemo z orodjem Reševalec. V članku analiziramo modificirano, aditivno in multiplikativno Holt-Winters-ovo metodo (ki spadajo med metode eksponentnega glajenja) in opišemo model ‚združene‘ optimizacije parametrov metode napovedovanja in modela upravljanja zalog. Predlagano združeno optimizacijo celotnih stroškov dobavne verige primerjamo z optimizacijo, ki bazira le na napovedovanju povpraševanja po energentih. V kriterijsko funkcijo celotnih stroškov vključimo tako stroške držanja zalog kot tudi stroške primanjkljaja (upoštevaje različne penale) za oba člena dobavne verige, distributerja in dobavitelja.

Za namen raziskave uporabimo 756 realnih četrletnih časovnih vrst iz M3-Competition ter 300 simuliranih časovnih vrst. Rezultati študije pokažejo, da celovito upravljanje z energijskimi viri bistveno zmanjša celotne stroške dobavne verige v primerjavi z lokalno (ločeno) optimizacijo napovedovanja in uravnavanja zalog. Iz primerjave rezultatov je razvidno tudi, da ustrezno izbrana metoda napovedovanja (v našem primeru je to modificirana Holt-Winters-ova metoda) omogoča izboljšanje optimizacije in ustreznih strateških odločitev. Celovito upravljanje tako zagotavlja boljše planiranje energentov in učinkovitejšo proizvodnjo derivatov energije iz primarnih energijskih virov.

V nadaljnje raziskave bomo vključili študijo vpliva modificirane Holt-Winters-ove metode v združeni optimizaciji na učinek biča, kot tudi na sprostitev omejitev števila členov v dobavni verigi in dobavnih odlogov. Pri tem bomo poskušali najti odgovor na to, kakšen je efekt razširjenega modela celovitega upravljanja (združene optimizacije) v večjem okolju (npr. na ravni Evropske unije), se pa zavedamo, da je implementacija sistema v takem okolju veliko bolj kompleksna in zahteva veliko povezanost med podjetji, tako v smislu podpore informacijske tehnologije kot tudi v izmenjavi informacij.

Do danes je bilo na področju razumevanja interakcije med napovedovanjem in upravljanjem zalog narejenih zelo malo empiričnih raziskav, zato naša študija predstavlja doprinos na omenjenem raziskovalnem področju, prav tako pa tudi na področju uporabe in prakse, saj se lahko izsledki raziskave in priporočila uporabijo v realnem gospodarskem sektorju.

Ključne besede: upravljanje z energijskimi viri, dobavna veriga, napovedovanje, zaloge, celotni stroški

DOKTORSKE DISERTACIJE

Na Fakulteti za strojništvo Univerze v Ljubljani so obranili svojo doktorsko disertacijo:

- dne 6. oktobra 2016 **Primož LIPAR** z naslovom: »Identifikacija zvočnega vira z vizualizacijo na osnovi primerjave značilnih zvočnih koeficientov« (mentor: izr. prof. dr. Jurij Prezelj, somentor: prof. dr. Mirko Čudina);

V disertaciji je predstavljen inovativen pristop identifikacije vira zvoka stroja ali naprave. Nov postopek identifikacije temelji na uporabi mikrofonske antene za namen določanja ali preverjanja lokacije vira. Antena v sklopu z metodo oblikovanja snopa omogoča ojačenje signala iz želene smeri in s tem izboljša proces identifikacije v hrupnem okolju. Predlagan sistem vsebuje poleg mikrofonske antene tudi metode za parametrizacijo in klasifikacijo zvočnega signala. Z uporabo parametrizacije koeficientov frekvenčnega cepstra se iz sintetiziranega zvočnega signala izračunajo značilke, ki se uporabijo v postopku klasifikacije. Statistično modeliranje se izvede z uporabo postopka mešanice Gaussovih porazdelitev, kjer se v procesu učenja iz značilk poznanih zvočnih signalov izdelajo statistični modeli in shranijo v bazo. V postopku razpoznavanja oziroma identifikacije pa se meri statistično ujemanje značilk neznanega zvoka z modeli iz baze.

Predlagan sistem omogoča znotraj določenih meja identifikacijo večjega števila virov, ki delujejo istočasno. Z razliko od sistema, ki vsebuje le en mikrofonski sistem z anteno ojači signal obravnavanega zvočnega vira in s tem izboljša proces identifikacije. Z uporabo dodatne informacije o lokaciji pa postane identifikacija vira še toliko bolj zanesljiva;

- dne 19. oktobra 2016 **Matjaž MRŠNIK** z naslovom: »Večosno vibracijsko utrujanje v frekvenčni domeni« (mentor: prof. dr. Miha Boltežar);

V delu je predstavljena in eksperimentalno primerjana skupina spektralnih metod, namenjenih oceni porazdelitve amplitud ciklov naključne enosne napetosti. Metode so primerjane na realnih spektrih, tipičnih za strukturno dinamiko. Eksperimentalno je primerjana tudi skupina večosnih

porušitvenih kriterijev za izračun ekvivalentne naključne enosne napetosti v materialu. Porušitev vzorcev med eksperimentom je pri tem dosežena s širokospektralnim vzbujanjem dinamskega odziva. Predlagan je nov pristop k vrednotenju utrujanja v frekvenčnem prostoru z uporabo modalne dekompozicije;

- dne 28. oktobra 2016 **Alexandra AULOVA** z naslovom: »Uporaba nevronske mreže za modeliranje disipativnih sistemov« (mentor: prof. dr. Igor Emri, somentor: prof. dr. Edvard Govekar);

Polimerni materiali, ki so tipični predstavniki disipativnih sistemov vstopajo v zahtevne inženirske aplikacije. Zato je potreben natančen in zanesljiv nadzor stanja in trajnosti polimernih struktur. Sistem, ki to zagotavlja mora biti sposoben zaznati geometrijske spremembe, tako kot obstoječi sistemi, poleg tega pa mora zaznati spremembe časovno-odvisnih mehanskih lastnosti, ki jih povzročijo zunanje statične in dinamične obremenitve, ter okoljski pogoji.

Doktorsko delo obravnava problem pridobitve segmenta relaksacijske krivulje iz eksperimentalnih podatkov pridobljenih iz enosnih eksperimentov z konstantno hitrostjo obremenitve, kar predstavlja inverzni problem. Inverzni problem je bil rešen z uporabo nevronske mreže 'Multilayer Perceptron' in 'Radial Basis Function'. Poleg tega je bila obravnavana direktna določitev relaksacijskega mehanskega spektra iz enakih eksperimentalnih podatkov. V ta namen je bila uporabljena prestrukturirana nevronska mreža.

Pokazano je bilo, da nevronska mreža 'Radial Basis Function' robustna in izkazuje obetavne generalizacijske sposobnosti v primerjavi s 'klasično' numerično metodo prilagajanja eksponentov. Zato je ta pristop mogoče uporabiti pri razvoju sistemov za nadzor polimernih struktur v realnem času. Po drugi strani, pa so v primeru uporabe pristopa z prestrukturirano nevronske mreže, potrebne še nadaljnje raziskave in izboljšave.

Information for Authors

All manuscripts must be in English. Pages should be numbered sequentially. The manuscript should be composed in accordance with the Article Template given above. The maximum length of contributions is 10 pages. Longer contributions will only be accepted if authors provide justification in a cover letter. For full instructions see the Information for Authors section on the journal's website: <http://en.sv-jme.eu>.

SUBMISSION:

Submission to SV-JME is made with the implicit understanding that neither the manuscript nor the essence of its content has been published previously either in whole or in part and that it is not being considered for publication elsewhere. All the listed authors should have agreed on the content and the corresponding (submitting) author is responsible for having ensured that this agreement has been reached. The acceptance of an article is based entirely on its scientific merit, as judged by peer review. Scientific articles comprising simulations only will not be accepted for publication; simulations must be accompanied by experimental results carried out to confirm or deny the accuracy of the simulation. Every manuscript submitted to the SV-JME undergoes a peer-review process.

The authors are kindly invited to submit the paper through our web site: <http://ojs.sv-jme.eu>. The Author is able to track the submission through the editorial process - as well as participate in the copyediting and proofreading of submissions accepted for publication - by logging in, and using the username and password provided.

SUBMISSION CONTENT:

The typical submission material consists of:

- A **manuscript** (A PDF file, with title, all authors with affiliations, abstract, keywords, highlights, inserted figures and tables and references),
 - Supplementary files:
 - a **manuscript** in a WORD file format
 - a **cover letter** (please see instructions for composing the cover letter)
 - a ZIP file containing **figures** in high resolution in one of the graphical formats (please see instructions for preparing the figure files)
 - possible **appendices** (optional), cover materials, video materials, etc.
- Incomplete or improperly prepared submissions will be rejected with explanatory comments provided. In this case we will kindly ask the authors to carefully read the Information for Authors and to resubmit their manuscripts taking into consideration our comments.

COVER LETTER INSTRUCTIONS:

Please add a **cover letter** stating the following information about the submitted paper:

1. **Paper title**, list of **authors** and their **affiliations**.
2. **Type of paper**: original scientific paper (1.01), review scientific paper (1.02) or short scientific paper (1.03).
3. A **declaration** that neither the manuscript nor the essence of its content has been published in whole or in part previously and that it is not being considered for publication elsewhere.
4. State the **value of the paper** or its practical, theoretical and scientific implications. What is new in the paper with respect to the state-of-the-art in the published papers? Do not repeat the content of your abstract for this purpose.
5. We kindly ask you to suggest at least two **reviewers** for your paper and give us their names, their full affiliation and contact information, and their scientific research interest. The suggested reviewers should have at least two relevant references (with an impact factor) to the scientific field concerned; they should not be from the same country as the authors and should have no close connection with the authors.

FORMAT OF THE MANUSCRIPT:

The manuscript should be composed in accordance with the Article Template. The manuscript should be written in the following format:

- A **Title** that adequately describes the content of the manuscript.
- A list of **Authors** and their **affiliations**.
- An **Abstract** that should not exceed 250 words. The Abstract should state the principal objectives and the scope of the investigation, as well as the methodology employed. It should summarize the results and state the principal conclusions.
- 4 to 6 significant **key words** should follow the abstract to aid indexing.
- 4 to 6 **highlights**; a short collection of bullet points that convey the core findings and provide readers with a quick textual overview of the article. These four to six bullet points should describe the essence of the research (e.g. results or conclusions) and highlight what is distinctive about it.
- An **Introduction** that should provide a review of recent literature and sufficient background information to allow the results of the article to be understood and evaluated.
- A **Methods** section detailing the theoretical or experimental methods used.
- An **Experimental section** that should provide details of the experimental set-up and the methods used to obtain the results.
- A **Results** section that should clearly and concisely present the data, using figures and tables where appropriate.
- A **Discussion** section that should describe the relationships and generalizations shown by the results and discuss the significance of the results, making comparisons with previously published work. (It may be appropriate to combine the Results and Discussion sections into a single section to improve clarity.)
- A **Conclusions** section that should present one or more conclusions drawn from the results and subsequent discussion and should not duplicate the Abstract.
- **Acknowledgement** (optional) of collaboration or preparation assistance may be included. Please note the source of funding for the research.
- **Nomenclature** (optional). Papers with many symbols should have a nomenclature that defines all symbols with units, inserted above the references. If one is used, it must contain all the symbols used in the manuscript and the definitions should not be repeated in the text. In all cases, identify the symbols used if they are not widely recognized in the profession. Define acronyms in the text, not in the nomenclature.
- **References** must be cited consecutively in the text using square brackets [1] and collected together in a reference list at the end of the manuscript.
- **Appendix(-ices)** if any.

SPECIAL NOTES

Units: The SI system of units for nomenclature, symbols and abbreviations should be followed closely. Symbols for physical quantities in the text should be written in italics (e.g. v , T , n , etc.). Symbols for units that consist of letters should be in plain text (e.g. ms^{-1} , K, min, mm, etc.). Please also see: <http://physics.nist.gov/cuu/pdf/sp811.pdf>.

Abbreviations should be spelt out in full on first appearance followed by the abbreviation in parentheses, e.g. variable time geometry (VTG). The meaning of symbols and units belonging to symbols should be explained in each case or cited in a **nomenclature** section at the end of the manuscript before the References.

Figures (figures, graphs, illustrations digital images, photographs) must be cited in consecutive numerical order in the text and referred to in both the text and the captions as Fig. 1, Fig. 2, etc. Figures should be prepared without borders and on white grounding and should be sent separately in their original formats. If a figure is composed of several parts, please mark each part with a), b), c), etc. and provide an explanation for each part in Figure caption. The caption should be self-explanatory. Letters and numbers should be readable (Arial or Times New Roman, min 6 pt with equal sizes and fonts in all figures). Graphics (submitted as supplementary files) may be exported in resolution good enough for printing (min. 300 dpi) in any common format, e.g. TIFF, BMP or JPG, PDF and should be named Fig1.jpg, Fig2.tif, etc. However, graphs and line drawings should be prepared as vector images, e.g. CDR, AI. Multi-curve graphs should have individual curves marked with a symbol or otherwise provide distinguishing differences using, for example, different thicknesses or dashing.

Tables should carry separate titles and must be numbered in consecutive numerical order in the text and referred to in both the text and the captions as Table 1, Table 2, etc. In addition to the physical quantities, such as t (in italics), the units [s] (normal text) should be added in square brackets. Tables should not duplicate data found elsewhere in the manuscript. Tables should be prepared using a table editor and not inserted as a graphic.

REFERENCES:

A reference list must be included using the following information as a guide. Only cited text references are to be included. Each reference is to be referred to in the text by a number enclosed in a square bracket (i.e. [3] or [2] to [4] for more references; do not combine more than 3 references, explain each). No reference to the author is necessary.

References must be numbered and ordered according to where they are first mentioned in the paper, not alphabetically. All references must be complete and accurate. Please add DOI code when available. Examples follow.

Journal Papers:

Surname 1, Initials, Surname 2, Initials (year). Title. Journal, volume, number, pages, DOI code.

- [1] Hackenschmidt, R., Alber-Laukant, B., Rieg, F. (2010). Simulating nonlinear materials under centrifugal forces by using intelligent cross-linked simulations. *Strojniški vestnik - Journal of Mechanical Engineering*, vol. 57, no. 7-8, p. 531-538, DOI:10.5545/sv-jme.2011.013.

Journal titles should not be abbreviated. Note that journal title is set in italics.

Books:

Surname 1, Initials, Surname 2, Initials (year). Title. Publisher, place of publication.

- [2] Groover, M.P. (2007). *Fundamentals of Modern Manufacturing*. John Wiley & Sons, Hoboken.

Note that the title of the book is italicized.

Chapters in Books:

Surname 1, Initials, Surname 2, Initials (year). Chapter title. Editor(s) of book, book title. Publisher, place of publication, pages.

- [3] Carbone, G., Ceccarelli, M. (2005). Legged robotic systems. Kordić, V., Lazinica, A., Merdan, M. (Eds.), *Cutting Edge Robotics*. Pro literatur Verlag, Mammendorf, p. 553-576.

Proceedings Papers:

Surname 1, Initials, Surname 2, Initials (year). Paper title. Proceedings title, pages.

- [4] Štefanič, N., Martinčević-Mikić, S., Tošanović, N. (2009). Applied lean system in process industry. *MOTSP Conference Proceedings*, p. 422-427.

Standards:

Standard-Code (year). Title. Organisation. Place.

- [5] ISO/DIS 16000-6.2:2002. *Indoor Air - Part 6: Determination of Volatile Organic Compounds in Indoor and Chamber Air by Active Sampling on TENAX TA Sorbent, Thermal Desorption and Gas Chromatography using MSD/FID*. International Organization for Standardization. Geneva.

WWW pages:

Surname, Initials or Company name. Title, from <http://address>, date of access.

- [6] Rockwell Automation. Arena, from <http://www.arenasimulation.com>, accessed on 2009-09-07.

EXTENDED ABSTRACT:

When the paper is accepted for publishing, the authors will be requested to send an **extended abstract** (approx. one A4 page or 3500 to 4000 characters). The instruction for composing the extended abstract are published on-line: <http://www.sv-jme.eu/information-for-authors/>.

COPYRIGHT:

Authors submitting a manuscript do so on the understanding that the work has not been published before, is not being considered for publication elsewhere and has been read and approved by all authors. The submission of the manuscript by the authors means that the authors automatically agree to transfer copyright to SV-JME when the manuscript is accepted for publication. All accepted manuscripts must be accompanied by a Copyright Transfer Agreement, which should be sent to the editor. The work should be original work by the authors and not be published elsewhere in any language without the written consent of the publisher. The proof will be sent to the author showing the final layout of the article. Proof correction must be minimal and executed quickly. Thus it is essential that manuscripts are accurate when submitted. Authors can track the status of their accepted articles on <http://en.sv-jme.eu/>.

PUBLICATION FEE:

Authors will be asked to pay a publication fee for each article prior to the article appearing in the journal. However, this fee only needs to be paid after the article has been accepted for publishing. The fee is 240.00 EUR (for articles with maximum of 6 pages), 300.00 EUR (for articles with maximum of 10 pages), plus 30.00 EUR for each additional page. The additional cost for a color page is 90.00 EUR. These fees do not include tax.

Strojniški vestnik - Journal of Mechanical Engineering
Askerčeva 6, 1000 Ljubljana, Slovenia,
e-mail: info@sv-jme.eu



<http://www.sv-jme.eu>

Contents

Papers

- 625 Mehdi Jafari Vardanjani, Alireza Araee, Jacek Senkara, Majid Sohrabian, Roozbeh Zarandooz
Influence of Shunting Current on the Metallurgical and Mechanical Behaviour of Resistance Spot-welded Joints in AA2219 Joints
- 636 Tahsin Tecelli Öpöz, Xun Chen:
Chip Formation Mechanism Using Finite Element Simulation
- 647 Liqiang Zhang, Kai Zhang, Yecui Yan:
Local Corner Smoothing Transition Algorithm Based on Double Cubic NURBS for Five-axis Linear Tool Path
- 657 Piotr Zgórnjak, Wojciech Stachurski, Dariusz Ostrowski:
Application of Thermographic Measurements for the Determination of the Impact of Selected Cutting Parameters on the Temperature in the Workpiece during Milling Process
- 665 Yongsheng Zhao, Cheng Yang, Ligang Cai, Weimin Shi, Yi Hong:
Stiffness and Damping Model of Bolted Joints with Uneven Surface Contact Pressure Distribution
- 678 Xiangyang Xu, Youchuan Tao, Changrong Liao, Shaojiang Dong, Renxiang Chen:
Dynamic Simulation of Wind Turbine Planetary Gear Systems with Gearbox Body Flexibility
- 685 Liljana Ferbar Tratar:
Comprehensive Energy Resource Management for Essential Reduction of the Total Cost